TU Delft

Delft University of Technology

Imaging DNA nanostructures with advanced TEM techniques

Kabiri, Yoones

DOI
10.4233/uuid:16e8c6f0-d2c4-47bd-b4e1-1564105c0a94

Publication date
2019

Citation (APA)
Kabiri, Y. (2019). *Imaging DNA nanostructures with advanced TEM techniques*. [Dissertation (TU Delft), Delft University of Technology]. https://doi.org/10.4233/uuid:16e8c6f0-d2c4-47bd-b4e1-1564105c0a94

Important note
To cite this publication, please use the final published version (if applicable).
Please check the document version above.

Copyright
Other than for strictly personal use, it is not permitted to download, forward or distribute the text or part of it, without the consent of the author(s) and/or copyright holder(s), unless the work is under an open content license such as Creative Commons.

Takedown policy
Please contact us and provide details if you believe this document breaches copyrights.
We will remove access to the work immediately and investigate your claim.

This work is downloaded from Delft University of Technology.
For technical reasons the number of authors shown on this cover page is limited to a maximum of 10.

Imaging DNA nanostructures with advanced TEM techniques

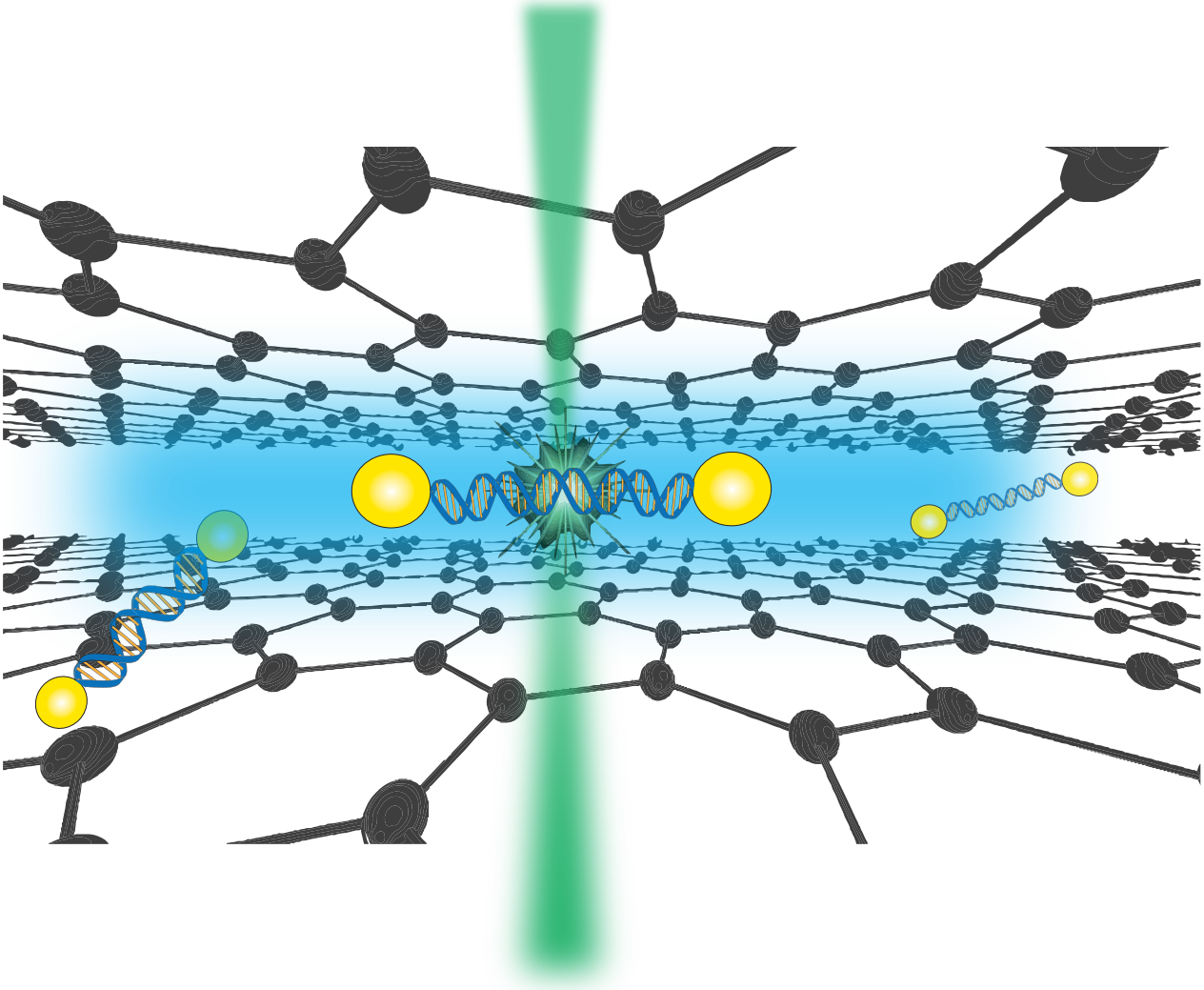

Yoones Kabiri

Imaging DNA nanostructures with advanced TEM techniques

YOONES KABIRI

Imaging DNA nanostructures with advanced TEM techniques

Dissertation

for the purpose of obtaining the degree of doctor
at Delft University of Technology,
by the authority of the Rector Magnificus prof.dr. ir. T.H.J.J. van der Hagen,
Chair of the Board for Doctorates,
to be defended publicly on
Tuesday 25 June 2019 at 12:30 o'clock

by

YOONES KABIRI

Master of Science in Advanced Materials and Processes,
University of Erlangen-Nuremberg, Germany
born in Esfahan, Iran.

this dissertation has been approved by

promotor: Prof. dr. C. Dekker
promotor: Prof. dr. H. W. Zandbergen

Composition of the doctoral committee:

Rector Magnificus,	chairperson
Prof. dr. C. Dekker	TU Delft, promotor
Prof. dr. H. W. Zandbergen	TU Delft, promotor

Independent members:

Prof. dr. ir. A. J. Koster	Leiden University
Prof. dr. ir. P. Kruit	TU Delft
Dr. A. Jakobi	TU Delft
Prof. dr. M. Dogterom	TU Delft

Other member:

Prof. dr. P. J. Peters	University of Maastricht



Keywords: transmission electron microscopy, graphene, DNA nanostructures

Cover Image: Yoones Kabiri

Printed by: IPSKAMP printing

Copyright © 2019 by Y. Kabiri
Casimir PhD series: 2019-25
ISBN: 978-90-8593-4080

An electronic version of this dissertation is available at `http://repository.tudelft.nl/`.

To my beloved parents and siblings,

who could not be present at my defence
due to visa restrictions

Contents

1 Introduction **1**

1.1 Introduction . . . 2
1.2 Seeing "plenty of room at the bottom" of biology with TEM . . . 2
1.3 DNA nanotechnology as an innovative microscopy toolkit . . . 5
1.4 Graphene as the thinnest TEM support in the nature . . . 5
1.5 Nanofluidics in TEM . . . 8
1.6 My thesis in a nutshell . . . 11
References . . . 13

2 Distortion of DNA origami on graphene imaged with advanced TEM techniques **19**

2.1 Introduction . . . 20
2.2 Results and Discussions . . . 21
2.3 Conclusion . . . 28
2.4 Experimental Section . . . 30
2.5 Supporting Information . . . 32
References . . . 45

3 Intercalating electron dyes for TEM visualization of DNA at the single-molecule level **49**

3.1 Introduction . . . 50
3.2 Results . . . 51
3.3 Discussion . . . 62
3.4 Conclusions . . . 64
3.5 Experimental Section . . . 64
3.6 Supporting Information . . . 67
References . . . 76

4 Visualization of unstained DNA nanostructures with advanced in-focus phase contrast TEM techniques **81**

4.1 Introduction . . . 82
4.2 Results . . . 84
4.3 Discussion . . . 90
4.4 Methods . . . 92
4.5 Supporting Information . . . 95
References . . . 101

5 Probing DNA nanostructures in graphene/SiN nanocapillaries with liquid-phase STEM **103**
5.1 Introduction . . . 104
5.2 Results and Discussion . . . 105
5.3 Conclusion . . . 112
5.4 Supporting Information . . . 114
References . . . 124

Summary **127**

Samenvatting **129**

Acknowledgements **133**

Curriculum Vitæ **137**

List of Publications **139**

1

Introduction

Somewhere, something incredible is waiting to be known.

Carl Sagan

In this introductory chapter, I present the main concepts underlying my thesis, which focus on transmission electron microscopy (TEM) imaging of DNA nanostructures.

1

1.1. Introduction

In this introductory chapter, I will guide the reader to understanding the main pillars of this thesis. TEM is an indispensable asset in science, without which much of our understanding about structure-function relations in materials would have not been elucidated. It is fair to say that much of our current progress in science would have not been possible if we couldn't see the building blocks of mother nature and tailor them to create unnatural materials. The birth of electron microscopy revolutionized our understanding of the materials world and later turned out to be an important characterization tool across various fields in science. However, electron beam-specimen interaction can limit the use of electron microscopy. For example, a recurrent question is why we nowadays can routinely resolve carbon atoms in a sp2 bonded graphene layer [1–4], which requires a resolution of better than 1 Angstrom, but we face a huge challenge to image a 2 nm DNA helix, which needs almost an order of magnitude less resolving power than the case of graphene lattice imaging.

The importance of imaging and characterization of DNA and DNA-based nanostructures is paramount. Being able to image DNA with TEM opens up ample opportunities across the life sciences for various applications. Although this seems trivial, the many issues addressed in this thesis show the unaddressed challenges for TEM imaging of DNA. In the following, I will introduce how I put different pieces of the puzzle together, i.e., I will give a glimpse of TEM, DNA nanotechnology, graphene, and the use of nanofluidics in TEM, all with the aim to probe DNA both in dry and aqueous states.

1.2. Seeing "plenty of room at the bottom" of biology with TEM

In 1959, Feynman mentioned in his famous visionary speech: "... The electron microscope is not quite good enough, with the greatest care and effort, it can only resolve about 10 angstroms. I would like to try and impress upon you while I am talking about all of these things on a small scale, the importance of improving the electron microscope by a hundred times. It is not impossible; it is not against the laws of diffraction of the electron. The wave length of the electron in such a microscope is only 1/20 of an angstrom. So, it should be possible to see the individual atoms ...". Later in his speech, he also addresses the importance of imaging DNA and other biological molecules with TEM to unravel the mysteries of life. Feynman was well aware of the drawbacks in electron optics at that time, most importantly the low numerical aperture and other theoretical limitations imposed by the electron lenses. Nowadays, we can see individual atoms with the resolution record of about 0.5 Angstrom [5], roughly 20 times better than the state of the art that Feynman mentioned in his speech in 1959. Yet, this does not mean that imaging biological macromolecules has become trivial since then. Biomolecules are very susceptible to electron radiation, a major limiting factor that changes their structure while being imaged with TEM [6–8]. Another major and common misunderstanding is the resolution versus contrast predicament. It is not the resolution, but rather the contrast which is the paramount issue for biological samples since they are mainly made of carbon, nitrogen, and hydrogen in a non-crystalline lattice. These elements have very low electron scattering strength and hence when the electron beam passes through them,

only a negligible change occurs to its amplitude or phase, which consequently hinders the image formation [9–11].

After discovery of the DNA double helical structure through X-Ray diffraction and understanding its major role in biology, tremendous efforts were made to visualize it with TEM. Importantly, the early works of Jacques Dubochet were dedicated to DNA and protein imaging with TEM, and later these efforts actually paved the way for the emergence of the Cryo-EM field [12, 13]. Imaging DNA in its native unlabeled form was achieved by flash-freezing it in solution [12]. However, if DNA is supported on commercial carbon supports, which is the common practice in sample preparation, the phase contrast imaging of the carbon film acts as a major source of noise and obscures the DNA information [14]. Therefore, TEM imaging of DNA could only be achieved if it was freely suspended, i.e., without any support membrane and spanned over pillars or edges that can hold stretched DNA by the ends [14–16].

A viable solution to increase the DNA contrast on commercial TEM supports was to stain it, either positively or negatively, with uranyl acetate and its derivatives as the most commonly applied contrast agents [17]. In the light of confusing interpretations of positive and negative staining, we define positive staining when the staining compounds interact with DNA to enhance its electron scattering strength. Alternatively, the term negative staining is used when the heavy compounds form a uniform layer on the support membrane, and hence form a shadow image of DNA in the stain background. Figure 1.1 schematically illustrates the positive and negative staining concepts for DNA imaging, together with their expected contrast in TEM and scanning TEM (STEM) micrographs. Most reports offer negative staining as the only visualization method and despite the importance of developing new DNA-binding electron dyes for positive staining (for example for imaging DNA in liquid), the field suffers from a prolonged stagnation. For instance, the synthesis and utilizing of an intercalating contrast agent for single-molecule visualization of DNA was never pursued, but we will address it in the current thesis.

Surprisingly, compared to the amount of studies dealing with obstacles in the sample-preparation part of the problem (i.e., staining issues, different support membranes, etc.), very little has been done to improve the DNA contrast via modification in the electron optics. This is partly due to complexity of the TEM instruments on the one hand (Figure 1.2) and to some theoretical limitations on the other hand. With the present HR-TEM machines and with a phase plate, one can image biological samples with about 1 Å resolution. One should get well acquainted with the science behind image formation in the electron optical system in order to be able to address this issue. For this thesis, going through the TEM electron ray diagrams in detail, or explaining the many modes of operation such as bright-field, dark-field, STEM, etc., does fit within the limited space here, and hence, the interested reader is recommended to read the literature for a full understanding of the image formation in TEM [18, 19]. For example, why STEM is the preferred imaging mode for liquid cell studies while cryo-EM is the fit technique for structure determination of biomolecules, needs a thorough discussion and understanding of the image formation mechanisms in TEM. In the following chapters, we will present a few different schematics of TEM ray diagrams, which help to understand the physics behind image formation under different operational mode of TEM, and their relevance in terms of imaging weak phase objects such as DNA nanostructures. Specifically, the

1

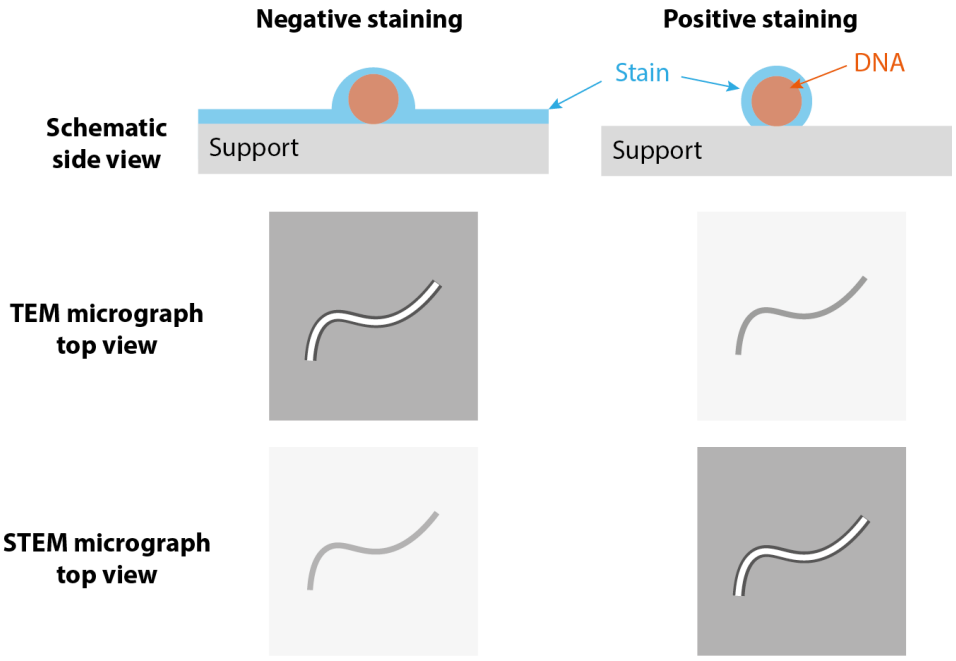

Figure 1.1: Schematics of DNA staining and its corresponding contrast in TEM and STEM mode of the microscope.

use of phase plates, low-voltage electron microscopy, special dark-field microscopy, and STEM is discussed.

1.3. DNA nanotechnology as an innovative microscopy toolkit

As Roald Hoffmann wrote in the American Scientist in 1994, "the nucleic-acid 'system' that operates in terrestrial life is optimized (through evolution) chemistry incarnate. Why not use it ... to allow human beings to sculpt something new, perhaps beautiful, perhaps useful, certainly unnatural."

When speaking about DNA, we naturally recall the very important molecule that is packed inside our cells and helps render our identities. However, DNA can also be created synthetically in the lab, through robust but relatively simple techniques in molecular biology, for example the polymerase chain reaction (PCR). This method was a primer to the DNA nanotechnology field that we are seeing today, after Nadrian Seeman's revolutionary idea to construct nanoobjects based on the Watson-Crick hybridization rules in DNA [20, 21]. What Seeman envisioned was further developed by Paul Rothemund [22], who could construct larger DNA constructs by folding a single-stranded (ss)DNA into custom-design constructs (Figure 1.3A). Computer-generated sequences of small oligonucleotides fold the long ssDNA scaffold (from a viral genome) into a 2D or 3D DNA shape, very similar to the Japanese ancient art of paper origami but made out of DNA instead, and hence called DNA origami. The DNA origami field has developed exponentially, with demonstrated robustness in synthesis of well-defined and functional molecular structures [23, 24].

The primary reason for utilizing DNA origami in this thesis was not to assemble a complex shape or functional nanoscale object. Rather, we utilized the origami concept to facilitate TEM imaging of DNA since the defined shape of its structure would "guide the eyes" and allows reliable DNA detection and contrast evaluation. Indeed, TEM images of single dsDNA strands supported on carbon could be difficult and misleading because the phase contrast images of carbon support produce significant noise, which smears the image of DNA. Therefore, utilization of a larger DNA object with a known shape such as DNA origami is a straightforward and facile approach to circumvent that problem.

DNA origami is not the only example that shows how DNA nanotechnology has evolved and bridged different scientific disciples. Another milestone was reached when researchers could tether DNA (soft matter) to gold nanoparticles (hard matter) [25, 26]. This has led to emerging set of applications in biology and physics [27–31]. Here, we are interested in this technology since gold nanoparticles are excellent electron scattering agents. This allows, for example, probing the dynamics of DNA and proteins in liquids or inside organisms [32–35]. Using this approach, we will also probe the dynamics of DNA inside miniscule liquid pockets.

1.4. Graphene as the thinnest TEM support in the nature

People have searched for the thinnest membrane in the nature, having minimal electron scattering strength, so that the sample of interest can be imaged with minimal noise coming from the background. This notion was realized as early as 1960s [36], way be-

1



Figure 1.2: Titan TEM microscope installed at the Kavli Nanolab at Delft. The majority of the experiments in this thesis were performed using this microscope.

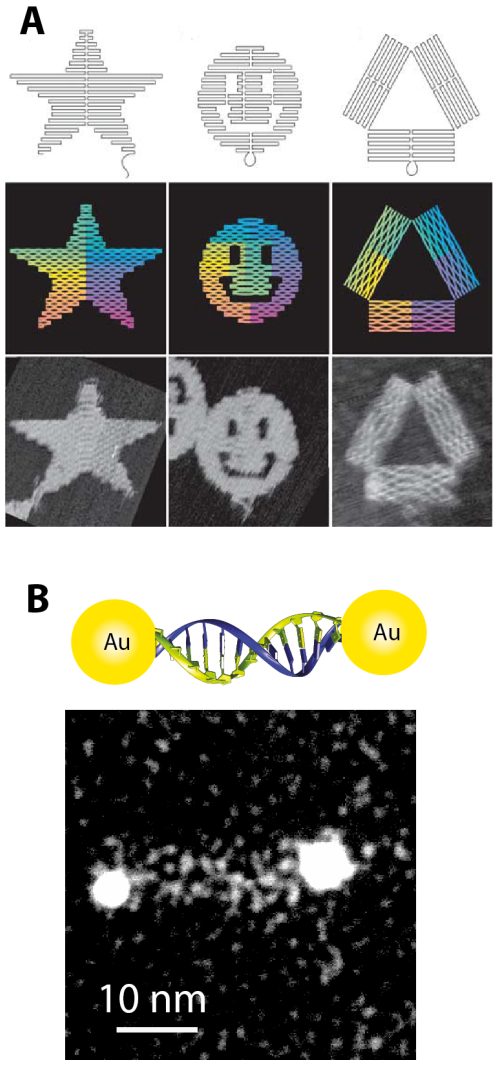

Figure 1.3: DNA nanotechnology allowing bottom-up synthesis of functional nanomaterials (A) DNA origami and (B) DNA-Au nanoconjugates. Panel (A) is reproduced from Ref [22].

fore the discovery of graphene in 2004 as a superb material for optoelectronic applications [37]. Figure 1.4 depicts flakes of monolayer graphene membranes spanning over a perforated TEM carbon grid. We observe a very small intensity difference between the hole that is covered by graphene (indicate by an arrow) compared to the empty hole. The small intensity suggests an ideal condition for electron microscopy applications. In addition to the high transparency for the electron beams, graphene also has excellent electrical and mechanical properties, which helps to support the samples on such a thin membrane as well as to dissipate the electron charge build-up during imaging. Finding a material having all these characteristics altogether was definitely a holy grail for TEM community. Already some samples in biology and materials science were investigated when supported on graphene [38–42]. However, little is known whether graphene has advantages for DNA imaging over the widely employed amorphous carbon membranes. We answer this question in this thesis, where we explore the suitability of graphene for DNA imaging both in dry and wet media.

1.5. Nanofluidics in TEM

Samples in TEM are situated in a high vacuum chamber (~10^{-5} Pa) because electron scattering with the gas molecules should not occur prior and after interaction with the sample. This high vacuum level causes any residual water in the sample to evaporate immediately after insertion into TEM, and thus probing wet materials in their native state is not possible. Frances Ross tackled this issue by introducing a liquid cell design based on SiN technology [44]. Due to encapsulation of water between two hermetically sealed SiN enclosures, samples can be maintained at near atmospheric pressures and hence retain their aqueous state. This was a remarkable step towards studying liquid-phase physiochemical phenomena with high spatial-temporal resolution. Researchers from different disciples, from materials science to biology, exploited this technique to shed light on the hitherto unknown processes at the nanometer scale. For example, nanoparticle nucleation and growth mechanisms followed by their Brownian motion, or their self-assembly are extensively studied [45, 46], protein structures are imaged in their native state [47], whole cells of eukaryotic and prokaryotic organisms are inspected [35, 48], and many other examples abound in the field of battery, energy, corrosion etc.

There are several drawbacks associated with the SiN liquid cells though. Most importantly, the SiN membranes are relatively thick (~20-50 nm for each of the two layers), and they bulge upon insertion into TEM, a phenomenon responsible for increasing the thickness of the liquid layer to several microns, causing major resolution loss. Also, SiN membranes are not conductive and hence they charge up during electron irradiation, which consequently increases radiolysis side reactions that alter the chemistry of the medium. To overcome these drawbacks, researchers at UC Berkeley introduced a new type of liquid cell in 2012 for in situ liquid TEM applications, namely graphene liquid cells (GLC) [49]. Entrapment of very thin water layer between two single-layer graphene dramatically increased the contrast of weak-phase objects while protecting them against harsh radiation damage [50, 51]. The disruptive GLC approach, and its later derivatives, enabled probing interesting biomolecules or organic/inorganic materials in liquid with TEM, that was previously not possible due to constraints in terms of resolution, contrast,

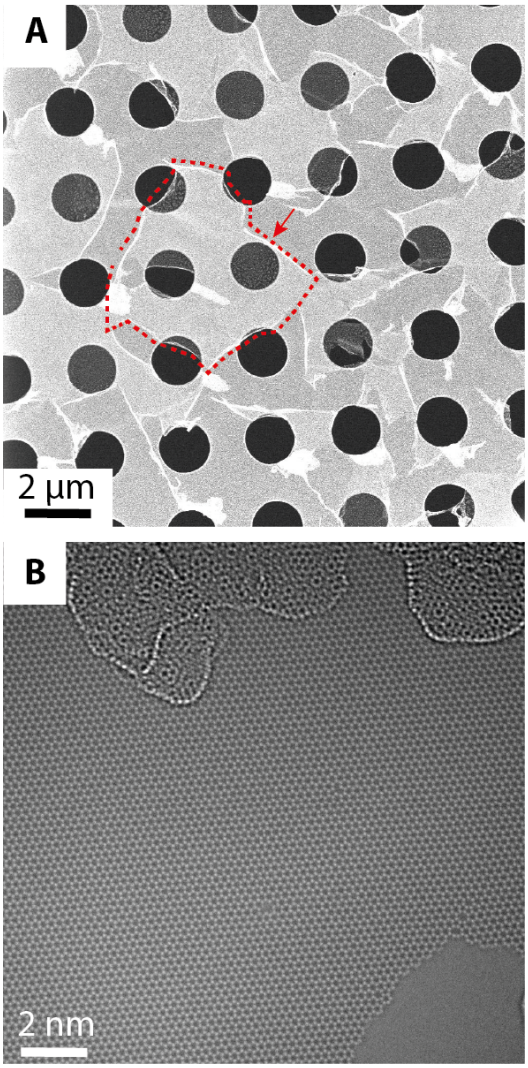

Figure 1.4: (A) Graphene flakes spanning on perforated carbon support imaged with low-magnification STEM. One exemple flake is identified using the red dotted line. (B) Cc+Cs corrected high-resolution TEM (HRTEM) image of graphene an 80 kV, reproduced with permission from Ref [43].

1

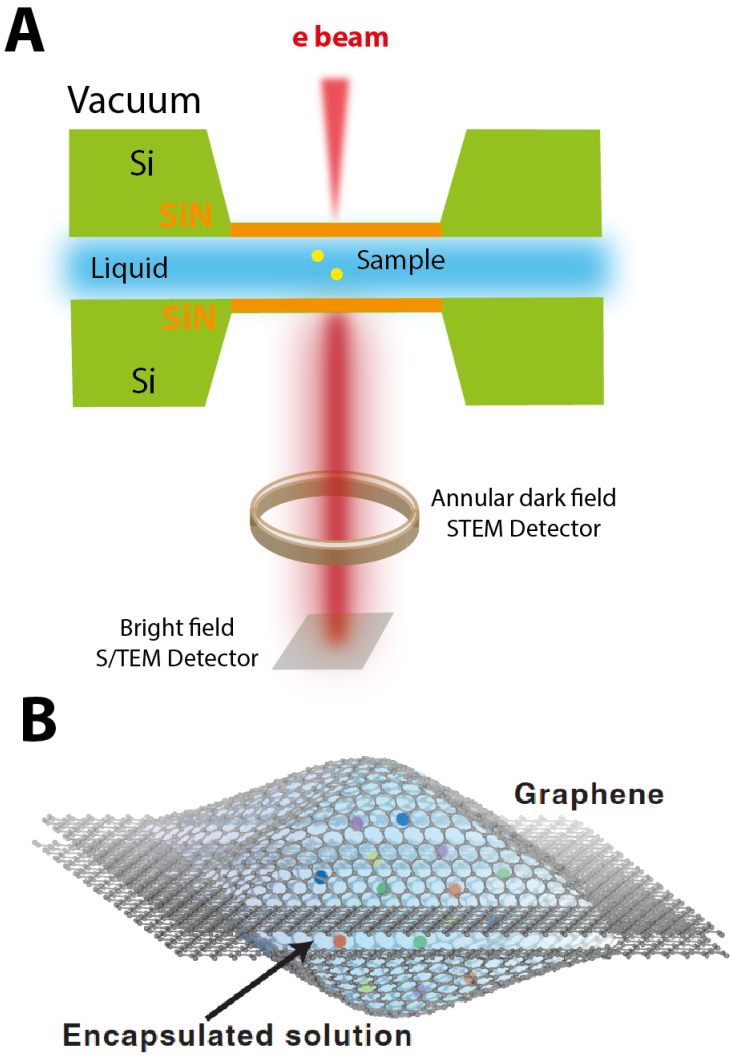

Figure 1.5: Two main strategies for liquid-phase TEM. (A) SiN and (B) graphene liquid cells. Panel B has been reproduced from Ref [49].

and beam damage. Interesting examples include imaging DNA-Au nanoconjugates, proteins, 2D water, nanoparticles, cellular organisms, DNA-Au superlattices, etc. [32, 52–60].

Maybe the most notable study was indeed the one carried out by the Alivisatos group [32]. They showed the movement dynamics of DNA-Au nanoconjugates inside the GLCs, and characterized the Brownian motion of such nanostructure. It was thus demonstrated that single DNA molecules inside these graphene nanochambers can withstand surprising amounts of adverse radiation damage in TEM [58, 61]. However, many open questions still remain unanswered. For example, what is the exact mechanism of damage mitigation? What is the role of the TEM operation mode, e.g. STEM vs TEM? What property in graphene is facilitating the TEM imaging? In **chapter 5**, we will touch upon some of these questions.

1.6. My thesis in a nutshell

The major aim of this thesis is to explore the visualization of DNA nanostructures using TEM through various means. We employ techniques from a wide range of disciplines, from molecular biology and chemistry, to electron optics and structural biology. Not only do we utilize previous well-established techniques, but we also develop new imaging capabilities for nucleic acids which were not pursued before. Excitingly, the past decade has seen spectacular advances in the TEM instrumentation. For example, the scintillator layer in CCD cameras has been removed in the new direct electron detectors [62]. These new detectors are much faster and more sensitive than CCD cameras, which assist high-contrast high-resolution TEM imaging. Next to new detectors, commercial phase plates are now available [63], which increase the contrast of materials containing light elements such as carbon, oxygen, and nitrogen that are abundant in most biological macromolecules. This has been one of the most important obstacles in obtaining detectable DNA contrast in TEM since the 1960s. New aberration-correctors (spherical (Cs), and chromatic (Cc)) are also facilitating high-resolution imaging [43, 64]. Concerning the substrate issue, graphene has proven to be an ideal sample support for electron microcopy applications. Taken together, the above-mentioned revolutions are sweeping through life and materials sciences, and have spurred a clear motivation to revive the historical endeavor of attempting DNA imaging with TEM.

In **chapter 2**, we design, fold, and characterize a special DNA origami nanostructure for TEM imaging. Our 2D DNA origami serves as a facile and straightforward route to image DNA with different spatial features, i.e., at single helix (2 nm wide), bundles (4 nm wide), etc. We set out to answer the question whether single-atom thick graphene poses a great advantage over amorphous carbon substrates (that are commercially available with thicknesses above 4 nm, e.g. more than an order of magnitude thicker than a graphene layer) in terms of improving the DNA contrast. We find that the origami nanoplates unfortunately undergo severe structural distortion when they are deposited on graphene. We could not obtain reliable dsDNA contrast on graphene. These rather discouraging results laid down the foundation for the remaining course of action for this thesis.

Chapter 3 deals with tackling the DNA contrast issue from a biochemistry point of view, i.e., through synthesis of a new DNA binding metallo-intercalator molecule,

namely bis-acridine uranyl (BAU). This can interact with the bases of DNA instead of covalent attachment to the DNA phosphate backbone (as in the conventional uranyl acetate stain [17]). Electron scattering strength of positively stained DNA on carbon membranes is thus expected to be greatly improved, and subsequently its contrast in TEM. We confirm the structure of the BAU molecule via NMR and MS spectroscopy, and show that BAU indeed strongly interacts with DNA through an intercalation binding mode. In STEM experiments, single DNA molecules were rendered visible using this new electron dye, where BAU depicts contrast enhancement comparable to that of uranyl acetate.

In **chapter 4**, we introduce advanced in-focus phase contrast TEM techniques for imaging challenging weak phase objects such as DNA origami nanostructures on commercial carbon membranes. These techniques differ substantially from the prevailing defocus-based conventional TEM (CTEM) technique. Whereas CTEM, even at its best capabilities, is unable of DNA visualization, we find that our newly introduced methods are indeed able to render unstained DNA visible. Single particle analysis (SPA), the de facto method in Cryo-EM structure determination of protein structures, is applied to micrographs taken by the state-of-the-art phase plate technology, namely volta-potential phase plate (VPP), as well as to micrographs taken by sub-Ångstrom low-voltage electron (SALVE) microscopy. We provide interesting insights on imaging DNA using these relatively new imaging capabilities. In addition, we probe the origami samples using a special dark-field (DF) technique and we observe good contrast enhancement.

Finally, the structural stability and movement dynamics of DNA-Au nanoconjugates is probed in **chapter 5**. We study these nanoconjugates in different nanofluidic architectures, i.e., graphene and SiN liquid cells. A central question was whether we can visualize the tethered DNA between the Au NPs with STEM in GLCs, and if this is possible, to understand the dynamic movements and structural stability of the DNA under the STEM imaging mode. We find that GLC facilitates the imaging of the nanoconjugates with good stability under scanning illumination. In contrast, SiN liquid cells pose great challenges in terms of contrast and radiation damage, due to higher thickness as well as the low conductivity of SiN membranes compared to graphene.

References

[1] J. C. Meyer, A. K. Geim, M. I. Katsnelson, K. S. Novoselov, T. J. Booth, and S. Roth, *The structure of suspended graphene sheets,* Nature **446**, 60 (2007).

[2] J. Meyer, *Transmission electron microscopy (tem) of graphene,* in *Graphene* (Elsevier, 2014) pp. 101–123.

[3] J. Meyer, A. Geim, M. Katsnelson, K. Novoselov, D. Obergfell, S. Roth, C. Girit, and A. Zettl, *On the roughness of single-and bi-layer graphene membranes,* Solid State Communications **143**, 101 (2007).

[4] J. C. Meyer, C. Kisielowski, R. Erni, M. D. Rossell, M. Crommie, and A. Zettl, *Direct imaging of lattice atoms and topological defects in graphene membranes,* Nano letters **8**, 3582 (2008).

[5] Y. Jiang, Z. Chen, Y. Han, P. Deb, H. Gao, S. Xie, P. Purohit, M. W. Tate, J. Park, S. M. Gruner, *et al.*, *Electron ptychography of 2d materials to deep sub-ångström resolution,* Nature **559**, 343 (2018).

[6] R. M. Glaeser, *Limitations to significant information in biological electron microscopy as a result of radiation damage,* Journal of ultrastructure research **36**, 466 (1971).

[7] E. Binshtein and M. D. Ohi, *Cryo-electron microscopy and the amazing race to atomic resolution,* Biochemistry **54**, 3133 (2015).

[8] R. Egerton, P. Li, and M. Malac, *Radiation damage in the tem and sem,* Micron **35**, 399 (2004).

[9] K. Nagayama and R. Danev, *Phase contrast electron microscopy: development of thin-film phase plates and biological applications,* Philosophical Transactions of the Royal Society B: Biological Sciences **363**, 2153 (2008).

[10] R. M. Glaeser, *Invited review article: Methods for imaging weak-phase objects in electron microscopy,* Review of Scientific Instruments **84**, 312 (2013).

[11] R. M. Glaeser, *How good can cryo-em become?* Nature methods **13**, 28 (2015).

[12] M. Adrian, B. ten Heggeler-Bordier, W. Wahli, A. Z. Stasiak, A. Stasiak, and J. Dubochet, *Direct visualization of supercoiled dna molecules in solution.* The EMBO journal **9**, 4551 (1990).

[13] J. Dubochet, *Cryo-em—the first thirty years,* Journal of microscopy **245**, 221 (2012).

[14] Y. Fujiyoshi and N. Uyeda, *Direct imaging of a double-strand dna molecule,* Ultramicroscopy **7**, 189 (1981).

[15] M. Marini, A. Falqui, M. Moretti, T. Limongi, M. Allione, A. Genovese, S. Lopatin, L. Tirinato, G. Das, B. Torre, *et al.*, *The structure of dna by direct imaging,* Science advances **1**, e1500734 (2015).

[16] F. Gentile, M. Moretti, T. Limongi, A. Falqui, G. Bertoni, A. Scarpellini, S. Santoriello, L. Maragliano, R. Proietti Zaccaria, and E. di Fabrizio, *Direct imaging of dna fibers: the visage of double helix,* Nano Letters **12**, 6453 (2012).

[17] C. R. Zobel and M. Beer, *Electron stains: I. chemical studies on the interaction of dna with uranyl salts,* The Journal of Cell Biology **10**, 335 (1961).

[18] C. B. Carter and D. B. Williams, *Transmission electron microscopy: Diffraction, imaging, and spectrometry* (Springer, 2016).

[19] R. Erni, *Aberration-corrected imaging in transmission electron microscopy: an introduction* (World Scientific Publishing Company, 2010).

[20] N. C. Seeman, *Dna in a material world,* Nature **421**, 427 (2003).

[21] N. C. Seeman, *Nucleic acid junctions and lattices,* Journal of theoretical biology **99**, 237 (1982).

[22] P. W. Rothemund, *Folding dna to create nanoscale shapes and patterns,* Nature **440**, 297 (2006).

[23] E. Stahl, T. G. Martin, F. Praetorius, and H. Dietz, *Facile and scalable preparation of pure and dense dna origami solutions,* Angewandte Chemie International Edition **53**, 12735 (2014).

[24] B. Saccà and C. M. Niemeyer, *Dna origami: the art of folding dna,* Angewandte Chemie International Edition **51**, 58 (2012).

[25] A. P. Alivisatos, K. P. Johnsson, X. Peng, T. E. Wilson, C. J. Loweth, M. P. Bruchez Jr, and P. G. Schultz, *Organization of 'nanocrystal molecules' using dna,* Nature **382**, 609 (1996).

[26] C. A. Mirkin, R. L. Letsinger, R. C. Mucic, and J. J. Storhoff, *A dna-based method for rationally assembling nanoparticles into macroscopic materials,* Nature **382**, 607 (1996).

[27] M. R. Jones, R. J. Macfarlane, B. Lee, J. Zhang, K. L. Young, A. J. Senesi, and C. A. Mirkin, *Dna-nanoparticle superlattices formed from anisotropic building blocks,* Nature materials **9**, 913 (2010).

[28] M. N. O'Brien, M. R. Jones, B. Lee, and C. A. Mirkin, *Anisotropic nanoparticle complementarity in dna-mediated co-crystallization,* Nature materials **14**, 833 (2015).

[29] M. R. Jones, N. C. Seeman, and C. A. Mirkin, *Programmable materials and the nature of the dna bond,* Science **347**, 1260901 (2015).

[30] B. Nickel and T. Liedl, *Dna-linked superlattices get into shape,* Nature materials **14**, 746 (2015).

[31] Y. Tian, Y. Zhang, T. Wang, H. L. Xin, H. Li, and O. Gang, *Lattice engineering through nanoparticle–dna frameworks,* Nature materials **15**, 654 (2016).

[32] Q. Chen, J. M. Smith, J. Park, K. Kim, D. Ho, H. I. Rasool, A. Zettl, and A. P. Alivisatos, *3d motion of dna-au nanoconjugates in graphene liquid cell electron microscopy,* Nano letters **13**, 4556 (2013).

[33] D. B. Peckys, G. M. Veith, D. C. Joy, and N. De Jonge, *Nanoscale imaging of whole cells using a liquid enclosure and a scanning transmission electron microscope,* PloS one **4**, e8214 (2009).

[34] D. B. Peckys and N. de Jonge, *Visualizing gold nanoparticle uptake in live cells with liquid scanning transmission electron microscopy,* Nano letters **11**, 1733 (2011).

[35] N. De Jonge, D. B. Peckys, G. Kremers, and D. Piston, *Electron microscopy of whole cells in liquid with nanometer resolution,* Proceedings of the National Academy of Sciences **106**, 2159 (2009).

[36] W. H. Dobelle and M. Beer, *Chemically cleaved graphite support films for electron microscopy,* The Journal of cell biology **39**, 733 (1968).

[37] K. S. Novoselov, A. K. Geim, S. V. Morozov, D. Jiang, Y. Zhang, S. V. Dubonos, I. V. Grigorieva, and A. A. Firsov, *Electric field effect in atomically thin carbon films,* science **306**, 666 (2004).

[38] R. S. Pantelic, J. W. Suk, Y. Hao, R. S. Ruoff, and H. Stahlberg, *Oxidative doping renders graphene hydrophilic, facilitating its use as a support in biological tem,* Nano letters **11**, 4319 (2011).

[39] R. S. Pantelic, J. W. Suk, C. W. Magnuson, J. C. Meyer, P. Wachsmuth, U. Kaiser, R. S. Ruoff, and H. Stahlberg, *Graphene: Substrate preparation and introduction,* Journal of structural biology **174**, 234 (2011).

[40] J. C. Meyer, Girit, M. Crommie, and A. Zettl, *Imaging and dynamics of light atoms and molecules on graphene,* Nature **454**, 319 (2008).

[41] J. Jeon, M. S. Lodge, B. D. Dawson, M. Ishigami, F. Shewmaker, and B. Chen, *Superb resolution and contrast of transmission electron microscopy images of unstained biological samples on graphene-coated grids,* Biochimica et Biophysica Acta (BBA)-General Subjects **1830**, 3807 (2013).

[42] R. S. Pantelic, J. C. Meyer, U. Kaiser, and H. Stahlberg, *The application of graphene as a sample support in transmission electron microscopy,* Solid State Communications **152**, 1375 (2012).

[43] F. Börrnert and U. Kaiser, *Chromatic-and geometric-aberration-corrected tem imaging at 80 kv and 20 kv,* Physical Review A **98**, 023861 (2018).

[44] M. Williamson, R. Tromp, P. Vereecken, R. Hull, and F. Ross, *Dynamic microscopy of nanoscale cluster growth at the solid–liquid interface,* Nature materials **2**, 532 (2003).

[45] N. De Jonge and F. M. Ross, *Electron microscopy of specimens in liquid,* Nature nanotechnology **6**, 695 (2011).

[46] F. M. Ross, *Opportunities and challenges in liquid cell electron microscopy,* Science **350**, aaa9886 (2015).

[47] U. M. Mirsaidov, H. Zheng, Y. Casana, and P. Matsudaira, *Imaging protein structure in water at 2.7 nm resolution by transmission electron microscopy,* Biophysical journal **102**, L15 (2012).

[48] T. J. Woehl, S. Kashyap, E. Firlar, T. Perez-Gonzalez, D. Faivre, D. Trubitsyn, D. A. Bazylinski, and T. Prozorov, *Correlative electron and fluorescence microscopy of magnetotactic bacteria in liquid: toward in vivo imaging,* Scientific reports **4**, 6854 (2014).

[49] J. M. Yuk, J. Park, P. Ercius, K. Kim, D. J. Hellebusch, M. F. Crommie, J. Y. Lee, A. Zettl, and A. P. Alivisatos, *High-resolution em of colloidal nanocrystal growth using graphene liquid cells,* Science **336**, 61 (2012).

[50] G. Algara-Siller, S. Kurasch, M. Sedighi, O. Lehtinen, and U. Kaiser, *The pristine atomic structure of mos2 monolayer protected from electron radiation damage by graphene,* Applied Physics Letters **103**, 203107 (2013).

[51] R. Zan, Q. M. Ramasse, R. Jalil, T. Georgiou, U. Bangert, and K. S. Novoselov, *Control of radiation damage in mos2 by graphene encapsulation,* ACS nano **7**, 10167 (2013).

[52] C. Wang, Q. Qiao, T. Shokuhfar, and R. F. Klie, *High-resolution electron microscopy and spectroscopy of ferritin in biocompatible graphene liquid cells and graphene sandwiches,* Advanced Materials **26**, 3410 (2014).

[53] G. Algara-Siller, O. Lehtinen, F. Wang, R. Nair, U. Kaiser, H. Wu, A. Geim, and I. Grigorieva, *Square ice in graphene nanocapillaries,* Nature **519**, 443 (2015).

[54] J. Park, H. Elmlund, P. Ercius, J. M. Yuk, D. T. Limmer, Q. Chen, K. Kim, S. H. Han, D. A. Weitz, A. Zettl, *et al.*, *3d structure of individual nanocrystals in solution by electron microscopy,* Science **349**, 290 (2015).

[55] M. Wojcik, M. Hauser, W. Li, S. Moon, and K. Xu, *Graphene-enabled electron microscopy and correlated super-resolution microscopy of wet cells,* Nature communications **6**, 7384 (2015).

[56] N. Mohanty, M. Fahrenholtz, A. Nagaraja, D. Boyle, and V. Berry, *Impermeable graphenic encasement of bacteria,* Nano letters **11**, 1270 (2011).

[57] J. M. Yuk, K. Kim, B. Alemán, W. Regan, J. H. Ryu, J. Park, P. Ercius, H. M. Lee, A. P. Alivisatos, M. F. Crommie, *et al.*, *Graphene veils and sandwiches,* Nano letters **11**, 3290 (2011).

[58] H. Cho, M. R. Jones, S. C. Nguyen, M. R. Hauwiller, A. Zettl, and A. P. Alivisatos, *The use of graphene and its derivatives for liquid-phase transmission electron microscopy of radiation-sensitive specimens,* Nano letters **17**, 414 (2016).

[59] C. Wadell, S. Inagaki, T. Nakamura, J. Shi, Y. Nakamura, and T. Sannomiya, *Nanocuvette: A functional ultrathin liquid container for transmission electron microscopy,* ACS nano **11**, 1264 (2017).

[60] U. Mirsaidov, V. Mokkapati, D. Bhattacharya, H. Andersen, M. Bosman, B. Özyilmaz, and P. Matsudaira, *Scrolling graphene into nanofluidic channels,* Lab on a Chip **13**, 2874 (2013).

[61] N. M. Schneider, M. M. Norton, B. J. Mendel, J. M. Grogan, F. M. Ross, and H. H. Bau, *Electron–water interactions and implications for liquid cell electron microscopy,* The Journal of Physical Chemistry C **118**, 22373 (2014).

[62] L. Jin, A.-C. Milazzo, S. Kleinfelder, S. Li, P. Leblanc, F. Duttweiler, J. C. Bouwer, S. T. Peltier, M. H. Ellisman, and N.-H. Xuong, *Applications of direct detection device in transmission electron microscopy,* Journal of structural biology **161**, 352 (2008).

[63] R. Danev, B. Buijsse, M. Khoshouei, J. M. Plitzko, and W. Baumeister, *Volta potential phase plate for in-focus phase contrast transmission electron microscopy,* Proceedings of the National Academy of Sciences **111**, 15635 (2014).

[64] M. Linck, P. Hartel, S. Uhlemann, F. Kahl, H. Müller, J. Zach, M. Haider, M. Niestadt, M. Bischoff, J. Biskupek, *et al.*, *Chromatic aberration correction for atomic resolution tem imaging from 20 to 80 kv,* Physical review letters **117**, 076101 (2016).

2

Distortion of DNA origami on graphene imaged with advanced TEM techniques

Either you repeat the same conventional doctrines everybody is saying; or else you say something true, and it will sound like it's from Neptune.

Noam Chomsky

While graphene may appear to be the ultimate support membrane for transmission electron microscopy (TEM) imaging of DNA nanostructures, very little is known if it poses an advantage over conventional carbon supports in terms of resolution and contrast. We carry out microscopic investigations on DNA origami nanoplates that are supported onto free-standing graphene, using advanced TEM techniques, including a new dark-field technique that was recently developed in our lab. TEM images of stained and unstained DNA origami are presented with high contrast on both graphene and amorphous carbon membranes. On graphene, the images of the origami plates show severe unwanted distortions, where the rectangular shape of the nanoplates is significantly distorted. From a number of comparative control experiments, we demonstrate that neither staining agents, nor screening ions, nor the level of electron-beam irradiation cause this distortion. Instead, we suggest that origami nanoplates are distorted due to hydrophobic interaction of the DNA bases with graphene upon adsorption of the DNA origami nanoplates.

This chapter has been published as: Yoones Kabiri, Adithya N. Ananth, Jaco van der Torre, Allard Katan, Jin-Yong Hong, Sairam Malladi, Jing Kong, Henny Zandbergen, and Cees Dekker, Distortion of DNA Origami on Graphene Imaged with Advanced TEM Techniques, Small, 1700876, 2017.

2.1. Introduction

Graphene features tantalizing properties suitable for a wide range of applications, from next-generation nanoelectronics and biosensing to TEM imaging of biomolecules [1–3]. Graphene gained an interest in the TEM community as a support substrate because it can be as thin as one carbon atom, which provides the lowest cross-section for elastic and inelastic scattering [4]. Moreover, graphene mitigates electron-beam-associated damage [4, 5]. As a result, high-resolution high-contrast images can be obtained for weak-phase objects that are supported onto or sandwiched between graphene layers [4, 6].

Can graphene also facilitate the imaging of (unstained) nucleic acids with TEM? Here, we address this question by utilizing DNA origami test structures. Such DNA origami, DNA that is folded into well-defined shapes, is an emerging workhorse for synthetic biology and programmable materials due to its accessible and compelling self-assembly principle [7–10]. Two-dimensional (2D) DNA origami is an excellent microscopy test object as it features the same scattering properties as double stranded DNA while it comes with a bigger and defined size, which helps the observation and investigation.

To the best of our knowledge, no high-resolution TEM (HRTEM) imaging of origami have been reported without staining or class averaging since various challenges arise for HRTEM imaging of biological specimens in general and DNA macromolecular assemblies in particular, such as sample preparation, beam damage, inherently low contrast of nucleic acids, and substrate signal contributions [11]. Some attempts of direct imaging of unstained DNA have been already reported [12–14]. However, even when deposited onto an atomically-thin layer of graphene, unstained DNA structures are barely distinguishable in normal TEM mode due to their low scattering elements [4, 15]. This necessitates further developments in electron optics for their visualization. The common practice in life-science TEM is to enhance the contrast at the expense of losing resolution by strongly defocusing the objective lens (by 1-10µm), i.e., transforming part of the phase information into amplitude. Such a methodology, however, is not suitable for high-resolution imaging due to information delocalization [16].

In order to boost the in-focus contrast for nucleic acids, we employ two complementary TEM techniques, viz., scanning transmission electron microscopy (STEM) and a special type of dark-field (DF) microscopy. STEM and DF allowed us to shed light on the conformational polymorphism of DNA origami on graphene without the need for any staining compound and class averaging. So far, only stained or class-averaged images of origami on carbon membranes were reported in literature. Since our imaging techniques provide good contrast as well as sufficient resolution for visualization, we could notice an unexpected behavior of the origami plates onto graphene, namely, that crumpled and deformed rectangles were obtained instead of fully flat and rectangular structures which are normally observed onto amorphous carbon supports. A range of complementary characterization techniques, provided in this manuscript, examines various parameters on the imaging of the origami plates, such as staining or screening ions, the level of electron-beam irradiation, and surface interaction of the origami plates with graphene.

2.2. Results and Discussions

We first characterized the DNA origami plates using liquid-cell atomic force microscopy (AFM). Figure 2.1b depicts a typical AFM image of the origami on a mica surface in liquid. It is seen that nanoplates are well dispersed on the mica surface with a suitable density for imaging. AFM was the fastest way to control the folding and purification success and was the basic control that we did prior to TEM sample preparations. Liquid-cell AFM was essential, as we found problems in AFM imaging in dry condition, such as curvature at the bottom of the plates, side arms sticking to one another, and concealment of the smaller cavity (observed for more than 95% of the plates tested for various Mg2+ ionic strength, see supporting information (SI), Figure S2.1). In liquid, on the other hand, the AFM images (Figure 2.1b) conform to the computer design. A slight distortion in aspect ratio is noticed, similar to earlier reports by Rothemund in his original paper [9], where he observed origami rectangles changing into a slightly hourglass-shaped structure due to imaging artifacts. The dsDNA loop at the bottom of the plate was quite floppy in liquid and we added 1mM NiCl2 in the buffer to immobilize the loop onto the surface.

After characterization of the origami structures with AFM, we turned to TEM for imaging them on free-standing graphene, which is the main focus of this paper. We started by imaging uranyl-stained origami on graphene by STEM, which provides the best contrast. We mostly found white "blobs", which were hardly distinguishable as DNA origami plate. Extensive imaging was carried out to make sure that our observation was indeed valid for all TEM samples. Figure 2.1c shows the best image that we could acquire in our dataset. The most striking observation is that the majority of the investigated nanoplates seem to show very crumpled conformations. To our surprise, DNA origami plates thus appear to be severely distorted upon adsorption onto graphene. Several attempts were made to improve the images such as graphene cleaning, changing Mg2+ concentration in a range of 15-60 mM, and removing EDTA from the buffer (SI, Figure S2.2). All these efforts failed to tackle the distortion problem. In the remaining part of the manuscript, we will examine what underlies this distortion.

We found out that distortion occurs regardless of the staining. DNA nanostructures are weak-phase objects for TEM, and staining agents that contain high-scattering elements such as heavy metals, are commonly utilized to increase the contrast. As a consequence of the binding of staining agents, artifacts can occur, e.g., double helix unwinding, DNA lengthening, kink formation, and intrastrand crosslinking [17]. In view of the distortion shown in Figure 2.1c, we wondered whether the staining could be the reason. To examine this, we acquired images of unstained origami on graphene. It should be noted that this is not possible with conventional TEM, even on graphene [4]. A better approach is using STEM, where a high-angle annular dark-field (HAADF) detector is utilized to collect the Rutherford-scattered electrons. The STEM contrast scales with Z^2 (or more precisely, the exponent of Z is reported to be between 1.6-1.8 instead of the classical value of 2) [18], which theoretically makes possible to distinguish DNA (rich in phosphorous with Z=15) on graphene (Z=6). One example of a STEM image of unstained origami on graphene is presented in Figure 2.1d. Incidentally, we mention that it is noteworthy to present such an image since TEM images of single-layer unstained DNA origami are rare. Similar to our observations for the stained origami, we present the best image for the unstained one. It can be seen that the majority of the nanoplates depict the

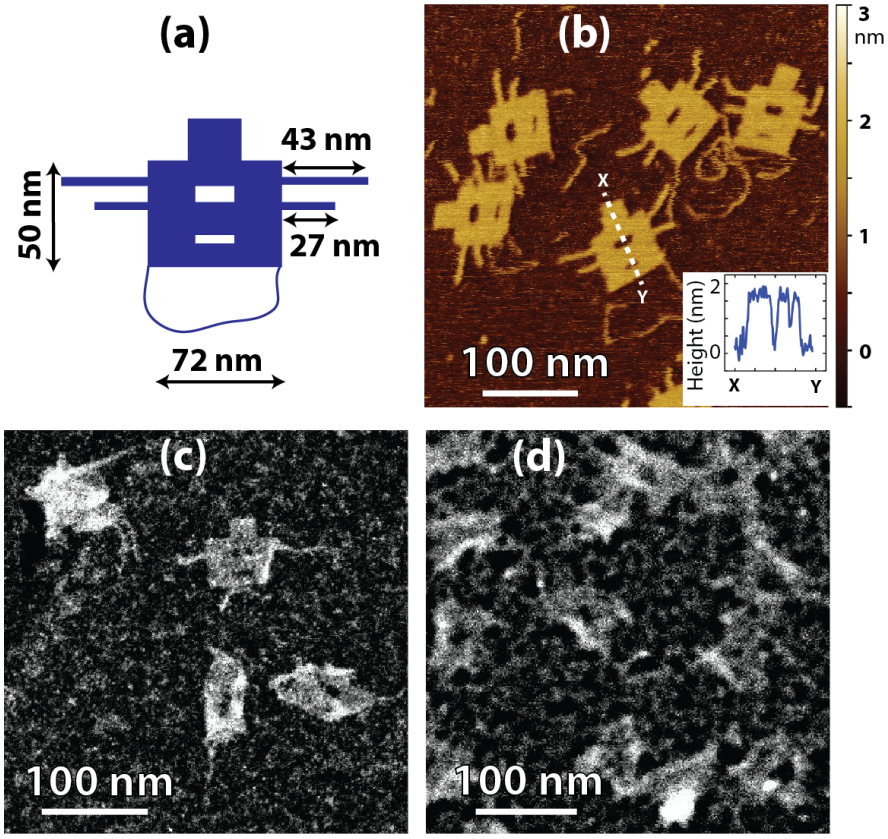

Figure 2.1: (a) Design schematic of the symmetric DNA origami nanoplate. (b) Liquid-cell AFM image of DNA origami on mica. (C) Uranyl acetate-stained DNA origami plates on suspended graphene imaged with STEM. (d) Same, but without any staining.

same severe structural deformation despite the absence of uranyl acetate stain. Again, various attempts such as changing Mg2+ concentration, removing EDTA from the buffer, or testing on different batch of graphene did not improve the images in terms of seeing DNA origami structures with all the design components. The comparison of Figure 2.1c and 2.1d thus shows that uranyl staining does not cause the origami distortion. Later in the manuscript, we show that our TEM techniques are indeed able to visualize even a single DNA helix. However, the severe distortion of DNA on graphene greatly smears the contrast that can be obtained.

The distortion of the DNA origami is also not caused by the electron beam, as could be conceived for a highly focused STEM probe. The good contrast in Figure 2.1c-d is due to high signal-to-noise (SNR) of the focused STEM beam, but the strongly focused beam can cause severe structural damage [19–21]. In general, the applicability of STEM to image polymeric materials, including nucleic acid macromolecules, should be cautiously examined. We thus speculated whether the distortion might be due to STEM-induced damage, leading to crumpling of nanoplates. Therefore we also probed the nanoplates with a broad parallel beam, where we circumvented the low SNR problem in wide-field TEM using our newly developed DF technique (see the experimental section for more details on the DF technique in detail) [22]. For a fair comparison, we acquired images on the exact same area, first exposing the region of interest with wide-field (DF image in Figure 2.2) and subsequently with a focused beam (STEM image in Figure 2.2). No difference was seen between sequential images in panel (c) and (b), not only for this particular region but also for the entire area of the TEM grids. Thus, these experiments exclude STEM-associated damage as the origin of the observed nanoplate crumpling.

Before we move on, we address several points in Figure 2.2 that are worthy of consideration: (1) In contrast to TEM imaging on amorphous carbon substrates, electron-induced contamination [23] is not observed on the graphene substrates such as in Figure 2.2a, even after several exposures on the boxed area. This hints on the damage-mitigation property of graphene reported earlier by Algara-Siller et al [24], which was attributed to the high thermal and electrical conductivity of graphene. The properties of graphene are also advantageous in terms of sample drift and charging, allowing improved HRTEM imaging. (2) By comparing Figure 2.2b and 2.2c, it is seen that the contrast enhancement obtained in the DF is comparable to that of STEM. Considering that most TEM labs around the world lack access to deflecting-coil STEM, using a "Mercedes star" in the objective aperture cassette suggests a cheap and easy alternative for contrast enhancement. Since the central beam is absent, the intensity reaching the camera is too low in DF technique, where the noise becomes an important factor (the central beam contributes to more than 99% of the intensity in a normal bright-field image [22]). Therefore, contrast can be further improved by removing the noise in the CCD cameras. Obviously, using the recent direct electron detection technology is advantageous in this regard [25]. (3) We also examined whether the distortion was an effect of sample orientation relative to the electron beam, i.e., if the electrons first hit the sample and then the graphene, or vice versa (note the two arrow directions in Figure 2.2d). Several studies reported such an orientation-dependent damage response in beam-sensitive materials, especially for materials containing light elements [5, 19, 24]. For our origami sample, sputtering of light atoms from the DNA structure might be a reason behind the crum-

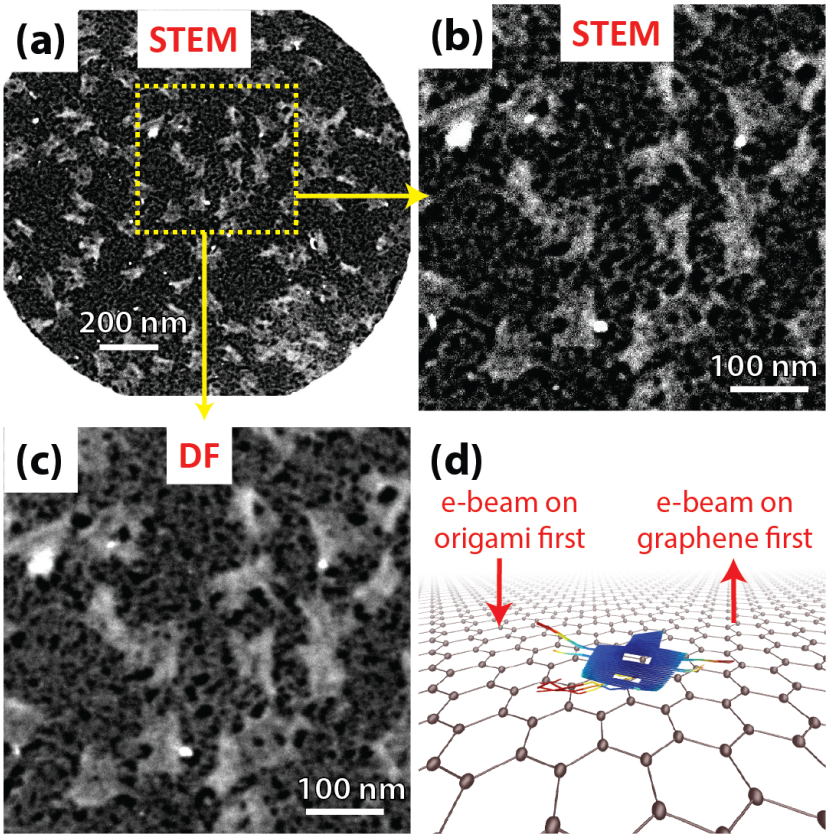

Figure 2.2: Comparison of STEM and DF to examine the effect of beam exposure on DNA origami distortion. (a) STEM overview image of the investigated area of unstained DNA origami on graphene. (b) Close-up of the boxed area in (a) imaged with STEM (c) Same for DF. Note that the sequence of events during imaging was from (c) to (a) in order to expose the area first with DF and only then with STEM. The DNA origami appears to be the same in panel (c) and (b), which shows that the intense STEM beam does not cause the distortion. Focus setting of the microscope was carried out in the neighboring area to avoid beam damage on the region of interest. The electron dose for the DF image in (c) corresponds to 25 e/Å2. Similar distorted DNA plates were seen when imaged with lower electron doses. (d) Artistic impression of origami on graphene (not to scale). Two different orientations were investigated: one where the electron beam first hits the origami and then graphene (left arrow), or the other way around (right arrow). We did not observe any difference in terms of damage response

pling of nanoplates. However, we did not observe any dependence on sample orientation relative to the electron beam, as in both cases, distorted plates were seen. (4) The background of the DNA origami images on graphene indicates the presence of contaminants. Likely, these are origami buffer constituents [4], hydrocarbon contamination [4, 26], or contaminants that result from graphene transfer.

Finally, we show that the distortion is dependent on which substrate the origami plates are deposited on. So far, we ruled out staining and imaging artifacts as the origin of origami damage on graphene. One other parameter to consider is the interaction of origami with graphene. It has been suggested that this interaction is mediated through π-π stacking of the aromatic purine and pyrimidine DNA bases with the delocalized π bonds of graphene [27]. To test this, we examined origami behavior on amorphous carbon film as an alternative substrate, where such π-π interactions will be absent. Figure 2.3 shows that the origami is well flattened on the amorphous carbon, depicting all the details encoded in the computer design (cf. Figure 2.1a). Note that remarkably we obtain good contrast of a 2 nm thin uranyl-stained DNA on a 15 nm thick carbon support (thickness of carbon measured by electron energy loss spectroscopy (EELS)). The nice images in Figure 2.3 incidentally prove that origami is stable under vacuum condition of the microscope (10^{-7} mbar) as well as during image acquisitions (both with STEM and DF at 300kV at room temperature).

We find that DNA origami is also distorted when deposited onto highly oriented pyrolytic graphite (HOPG) graphite, which has a surface very similar to that of graphene. Although this may seem trivial, there is no consensus on whether and how DNA origami interacts with the HOPG surface [27–31]. The different reported results may be due to different experimental conditions including buffer, pH, salt concentrations, or biased sampling of the imaging area. Lacking a proper comprehensive study, we carried out our own AFM experiments. Figure 2.4a shows the DNA origami structures on HOPG that are so heavily disconfigured that they are barely identifiable as rectangles. Control experiments (SI, Figure S2.3) proved that the observed structures on HOPG are indeed DNA and not hydrophobic contaminants.

The interaction of the origami plates and graphene can be prevented by surface functionalization. We passivated HOPG and graphene surfaces with polylysine (PLL) and with 1-pyrenecarboxylic acid (1PCA) [32] respectively, and performed AFM and TEM analysis. Figure 2.4b shows a typical AFM image of the origami plates onto a PLL-coated HOPG surface. By comparing the images of the DNA origami onto bare HOPG and PLL-coated HOPG surfaces (panel a and b in Figure 2.4), it is clear that PLL coating on HOPG prevents adverse interactions between the HOPG and the origami. Although the origami plates in Figure 2.4b are a bit distorted compared to Figure 2.1b (onto mica), the integrity of the structure is well maintained. We see a similar trend in TEM images of origami plates deposited onto bare and 1PCA-functionalized graphene. Figure 2.4c illustrates a typical STEM image that we acquired onto 1PCA-fuctionalized graphene. Whereas the images of the origami plates on bare graphene show very distorted conformation (cf. Figures 2.1 and 2.2), we see much less distortion in Figure 2.4c, where for example, the cavities inside the plates become visible. From both AFM and TEM experiments on functionalized HOPG and graphene surfaces, we thus can conclude that the interactions between the origami plates and graphene plays a crucial role in the observed distortion.

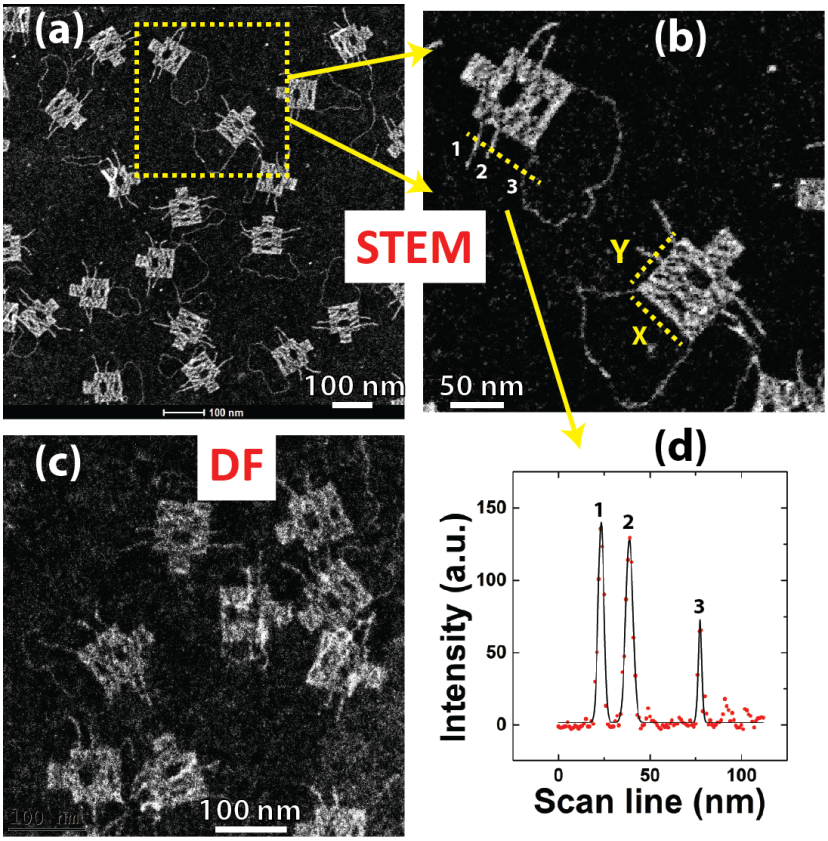

Figure 2.3: Distortion of the DNA origami is found to be substrate dependent. On amorphous carbon, origami is well spread and all details of the nanoplates become visible. (a) STEM image of uranyl-stained origami on 15 nm amorphous carbon (thickness measured by EELS). (b) Close-up of dashed area in (a). All structural features in the nanoplate design (cf. Figure 2.1a) are resolved. X and Y correspond to 71 and 65 nm respectively. (c) DF image on the same carbon membrane but from a different area. DF can also visualize the structures, however, with a lower SNR. (d) Line profile of the detector signal passing through the DNA bundles and single dsDNA loop indicated by the dashed line in panel (b). The peaks depict an excellent contrast with high SNR. We find full widths at half maxima of 3.4, 4.3 and 2.1 nm corresponding to peaks 1 to 3 respectively. These values conform to the widths of 2-helix DNA bundles (4 nm wide) and single dsDNA (2 nm wide) (cf. Figure 2.1a).

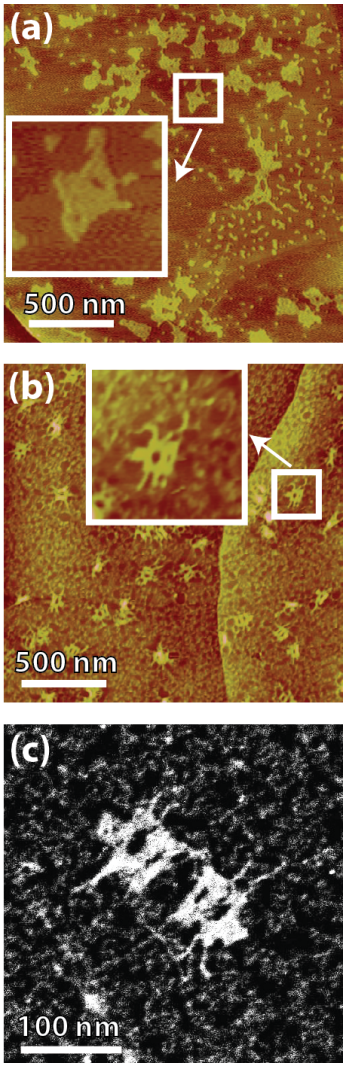

Figure 2.4: Graphene functionalization prevents π-π stacking with the hydrophobic DNA bases. (a) AFM image of origami on a HOPG surface. (b) Origami on a PLL-coated HOPG. Insets are enlargements of the plates marked inside the boxes in (a) and (b). (c) STEM image of a stained origami on 1PCA-functionalized graphene, showing less distorted plates compared to bare graphene.

To quantify the distortion, we define a parameter D as the surface area of the observed origami image divided by its theoretical surface area. For example, a value of D=0.5 represents a distorted nanoplate that has a surface area equal to only half the expected size. For calculation of the theoretical size according to the design sketch in Figure 2.1a, we need to consider a subtle point, namely that the origami structures are extended along the y-axis. Multiple works have previously demonstrated that 2D origami plates can not strictly be modeled as a series of closely-packed parallel double helices [9, 33]. In typical buffer conditions, electrostatic forces between the negatively charged strands cause inter-helical gaps (see Figure 2.5a). Hence, we calculate the size of the origami plate as follows. With n as the number of base pairs along the x-axis, the width X of the origami plate can be estimated as X= n*0.34 nm. However, the height Y of the origami does not simply follow a 2*h equation (with h as the number of double-stranded helices along the y-axis, and 2 nm as the width for B-form DNA; note that h=25 in our design). Instead, a modified expression Y= 2h + g(h-1) should be used, where g is the size of the inter-helical gap caused by the electrostatic repulsion between the strands [33]. The gap size g may vary depending on ionic strength or the design parameters. Since there is no computational method available for size estimation, liquid-cell AFM remains the easiest experimental way to measure the true dimensions of the origami. Figure 2.5b summarizes our liquid-cell AFM measurements of the origami size. In accord with the TEM data as well as with theoretical calculations, we find a consistent value for the nanoplate width of X = 72.8 ± 2.2 nm (mean ± standard deviation), whereas the height of the structure is Y = 67.2 ± 4.4 nm. From these values, we extracted the surface area of the nanoplate. Based on the obtained true size from the AFM experiments, we now return to the TEM image analysis. We processed the distortion of about 50 randomly selected origami plates in the TEM images taken from each substrate (graphene, 1PCA-functionalized graphene, and amorphous carbon), and report the result in Figure 2.5c. In accord with the shown TEM data (Figures 2.1-2.3), the statistical analysis in Figure 2.5c shows that most nanoplates are indeed severely crumpled to almost one third of their size, D=0.37 ± 0.08 (mean ± standard deviation), whereas they are much less distorted on carbon substrate, D=0.85 ± 0.10. For the 1PCA-functionalized graphene, D equals 0.58 ± 0.14, which falls in between the values for the graphene and carbon substrates. The statistical analysis thus shows that the substrates made from the same carbon element but with different hydrophobic surface properties result in significantly different D values.

2.3. Conclusion

With high-resolution STEM and DF techniques, we were able to image for the first time both stained and unstained DNA origami nanoplates on graphene and amorphous carbon membranes with good contrast. We observed that origami nanoplates exhibited a structural distortion when deposited onto graphene. Through a range of complementary control experiments, we conclude that the distortion can be attributed to the interaction of DNA with graphene, likely through π-π bonds. After quantification of the distortion onto different substrates, we found significant different mean values of the relative area of the origami plates, which quantitatively supports our observation in the presented TEM images. We conclude that while graphene provides the ultimate thin and

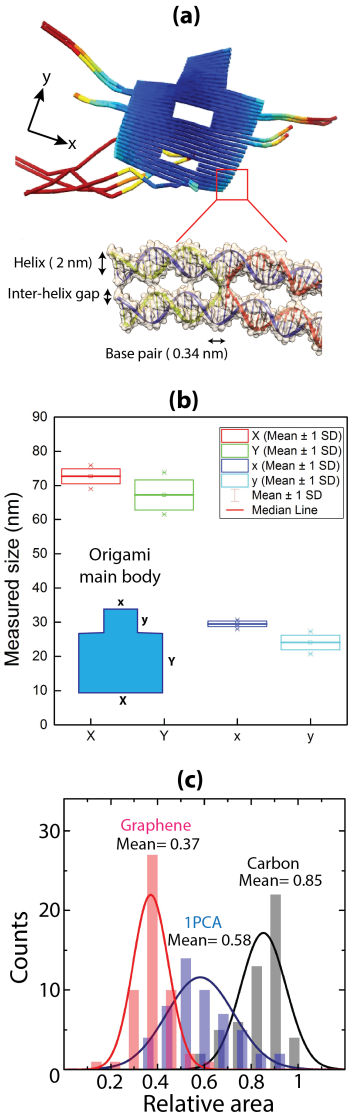

Figure 2.5: Quantification of the distortion of DNA origami on graphene-like substrates. (a) Inter-helical gaps along the y-axis of the nanoplate caused by electrostatic repulsions between the strands (the origami snapshot is exported from the caDNAano package) (b) Liquid-cell AFM measurements of the nanoplate dimensions (c) Statistical analysis of the relative area of origami plates extracted from TEM images onto different substrates (graphene, 1PCA-functionalizes graphene, and amorphous carbon). We find significant different mean values for the relative area on different substrates.

strong sample support for materials science or some biological samples [3], its applicability to DNA nanostructures is hindered by π-π interactions.

2.4. Experimental Section

Graphene growth, transfer, and quality characterization: Single-layer CVD-grown graphene was used to have large available areas for TEM investigations. Details of CVD growth and Raman spectroscopy for the growth characterization are given in the supplementary information (SI), Figure S2.4. In order to avoid polymer residues, graphene was transferred to TEM grids (Quantifoil, gold coated, 200 mesh) using a dry-transfer method (SI, Figure S2.5) [34]. Grids were examined by a number of TEM techniques to ensure layer thickness and cleanliness (SI, Figure S2.6). Note that no hydrophilic treatment such as glow discharging was performed on the grids, as graphene is very susceptible to even gentle plasma treatment.

Origami design, assembly, and purification: As a test object for TEM imaging, we designed a 2D DNA origami structure (Figure 2.1a) using caDNAno package [10]. We aimed to create a symmetric structure that can be well recognized in imaging. A 50x72 nm rectangular plate was designed with a number of different elements such as cavities in the middle (4 and 8 nm wide, 19 nm long), DNA bundles on the side arms (4 nm wide, 27 and 43 nm long), and a floppy dsDNA loop at the bottom (2 nm wide). For a detailed scheme of the design see SI, Figure S2.7. Note that the structure is a 2D design, which means that it is only one dsDNA thick (2 nm), which is desired as we aim for TEM visualization of single dsDNA structures. The structure is a suitable microscopy test object in order to check if different TEM techniques (STEM, DF) can provide enough resolution to visualize DNA at various length scales in the design.

To fold the origami plate, a 7560 base-long scaffold (M13mp18 phage-derived genomic DNA), and staple oligonucleotide strands were purchased from Tilibit®, Munich, Germany. Folding reactions consisted of folding buffer (5 mM Tris-base, 1 mM EDTA, 5 mM NaCl and 12.5 mM MgCl2 at pH8), 20 nM scaffold strand supplied with 10x excess oligo staples (200 nM). A thermocycler was used to fold the structure by heating first to 65 °C and then ramping the temperature from 60 to 40 °C at a cooling rate of 1 °C/h and subsequently keeping the nanostructures at 12 °C. After folding, origami plates were purified from excess staple oligonucleotides using Amicon cutoff filters (100 kDa MWCO, Milipore). Prior to centrifugation, the filter membranes were preconditioned with the working buffer (10 mM Tris-base, 1 mM EDTA, pH8, 15 mM MgCl2, 5 mM NaCl at pH8). Four cycles of purification (2200 rcf, 4 °C) removed most oligos (SI, Figure S2.8). The remaining solution in the dead volume of the filter was collected and diluted to a final origami concentration of 5 nM for TEM sample preparation. Oligomer sequences, finite-element simulations, and gel electrophoresis results (for both purified and unpurified plates) are given in SI.

TEM sample preparations: 5 µL of origami nanoplates (oligo purified, 5 nM) was drop casted onto graphene-coated TEM grids and incubated for 2 minutes. Subsequently, the samples were washed with Milli-Q (MQ) water to remove unadhered origamis, and excess MQ from the washing step was blotted away. For the stained samples, immediately after washing away the excess origamis, staining agent was applied (2% uranyl acetate in MQ, filtered through a 0.2 µm PTFE membrane), incubated for 1 minute, and washed

with MQ. We also prepared origami samples onto amorphous carbon grids (nominal 4 nm carbon onto 6 nm formvar-coated TEM grids, Electron Microscopy Science, USA), followed by the same protocol as mentioned for origami on graphene, but after rendering the carbon hydrophilic with nitrogen plasma.

TEM imaging: All STEM/DF images were taken with a FEI Titan microscope equipped with post-specimen aberration corrector under 300 kV operating voltage. The third-order spherical-aberration coefficient (Cs) was tuned to zero in the image corrector for all S/TEM alignments to minimize the delocalization. Utilization of a HAADF detector at a camera length of 28.3 cm resulted in mass-thickness dominated contrast. No class averaging was done and all images are single acquisitions at near zero focus. In the conventional dark-field technique, certain spatial frequencies in the back-focal plane are collected by the objective aperture to form the image. In our DF method, in contrast, all scattered frequencies are let through, except the noise-bearing central beam [22]. To realize this, we fabricated a "Mercedes star"-shaped aperture on a 5 µm-thick-platinum foil and ion-milled the Mercedes star using a FEI Helios microscope. Special care was taken to fabricate an as-smooth-as-possible aperture to avoid beam charging and image drift. Detailed geometry and dimensions of the delicate DF aperture is provided in SI, Figure S2.9, as well as an electron optical comparison with STEM (SI, Figure S2.10). The DF aperture achieves a 1-Å-information cutoff (SI, Figure S2.10c). We have previously shown that an information cutoff beyond 1Å would have a minimal effect on the contrast of weak-phase objects such as DNA origami supported onto graphene, whereas removal of the central beam has a major effect due to elimination of the Poisson noise [22]. Therefore, 1 Å information cutoff seems satisfactory for the DF aperture. Collection of all scattered electrons while omitting the central beam results in a dramatic contrast enhancement, as shown on a graphene test sample in SI, Figure S2.11. In contrast to conventional bright-filed imaging, the interference of diffracted beams enhances the contrast in our DF technique (non-linear imaging) [22]. Note that for complete blockade of the central beam, parallel illumination is a prerequisite. Hence, the C3 lens in the condenser system of the Titan microscope should be well tuned. We did DF image simulations to find the optimum focus for imaging. Based on our simulations (SI, Figure S2.12 and Figure S2.13), the best contrast is achieved at near zero focus with a Cs-corrected microscope. Finally, it should be mentioned that the temperature rise during STEM/DF imaging is negligible (only 1-2 K) [23] and will not cause any structural melting under the electron beam (as double-helix unwinding only occurs above 50 °C).

AFM imaging: AFM investigations were carried out on freshly cleaved surfaces of mica and HOPG under dry condition unless indicated otherwise. 4 µL of origami sample (5 nM) was drop casted onto 3 mm wide mica or HOPG disks, incubated for 1 minute, washed three times with MQ, and finally blown dry with nitrogen gas. Image acquisition was carried out in tapping mode and data analysis was done with NanoScope (Bruker, USA) and the open-source Gwyddion package [35]. For liquid-cell AFM imaging, DNA origami was incubated on mica for 1 minute, buffer-washed to remove the unbound plates, while the structure was kept in liquid for imaging without any further drying. The washing and imaging buffer was supplemented with an additional 1mM NiCl2 for better attachment of the origami to mica, which resulted in more stable AFM imaging.

2.5. Supporting Information

2.5.1. AFM images of nanoplates on mica under dry condition

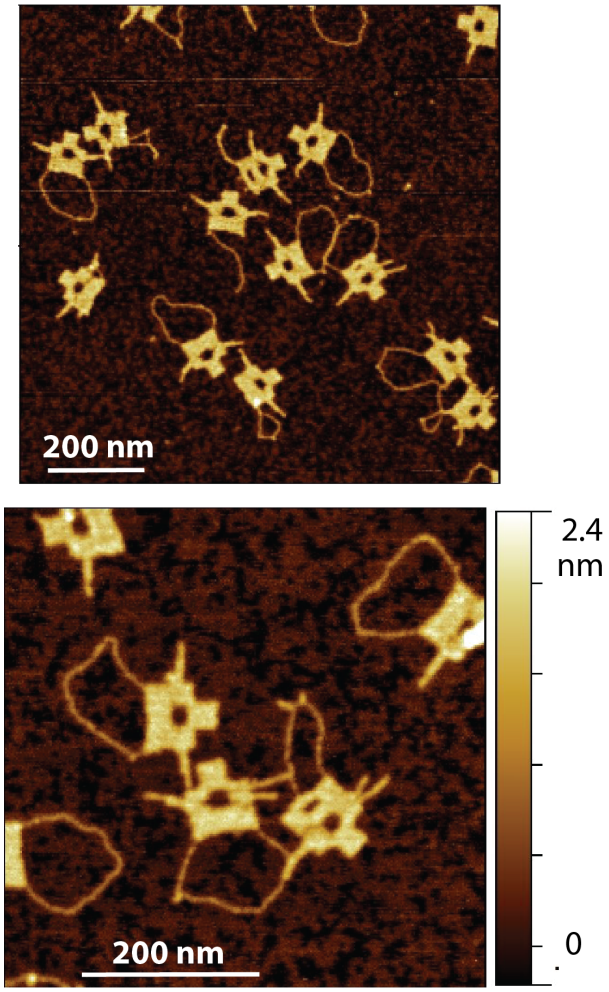

Figure S2.1: AFM images of origami nanoplates on mica under dry condition. We observe the following points: (1) Concealment of the smaller cavity inside the nanoplate. (2) A curvature at the bottom of the nanoplates (3) Side arms stick to one another.

2.5.2. Effect of magnesium and EDTA on the distortion of the origami plates

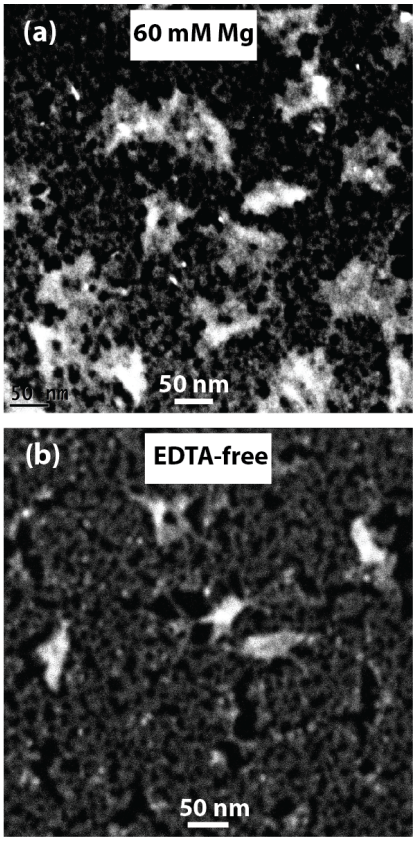

Figure S2.2: Distortion was found to be independent from ionic strength and presence of EDTA. We speculated whether increasing the Mg^{2+} ions in the buffer could stabilize the origami plates against adverse interactions with graphene. Hence, we acquired images of origami plates, which were purified in the working buffer supplemented with 60 mM MgCl2. Panel (a) depicts a typical DF image of such origami plates on graphene, where a similar distortion is observed. Thus, distortion is independent of Mg^{2+} screening ions. We also removed the EDTA from the buffer (using Trizma buffer instead of Tris-EDTA) and imaged the nanoplates on graphene. Panel (b) shows a typical STEM image of such origami plates in an EDTA-free buffer, which shows that origami distortion is not caused by presence of EDTA in the buffer.

2.5.3. AFM control experiments

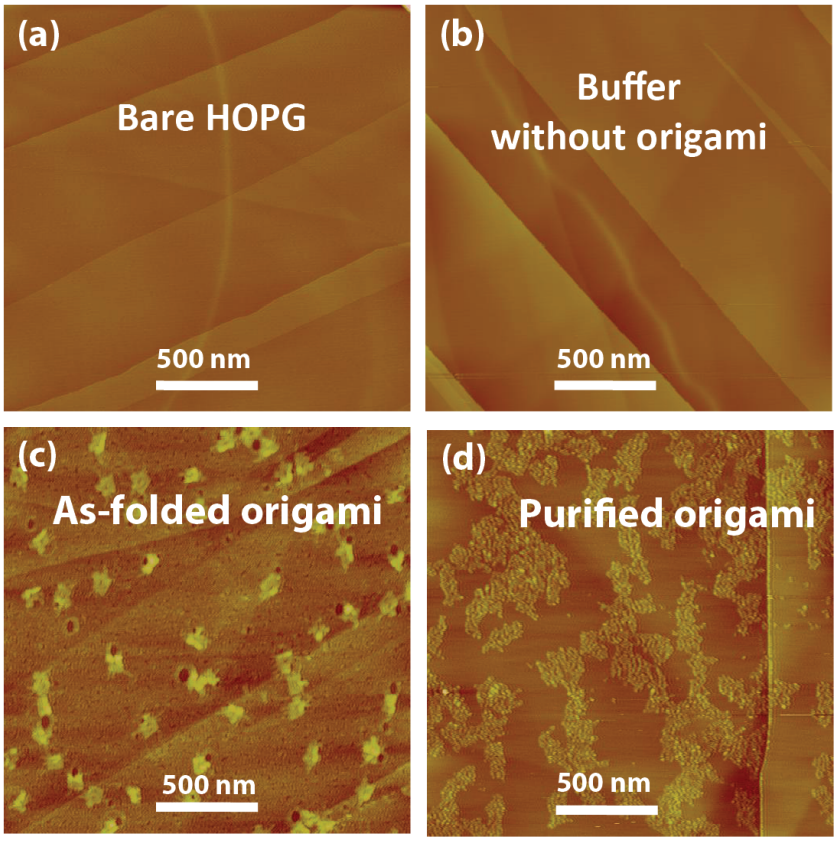

Figure S2.3: The distorted structures on HOPG (Figure 2.4a) are not related to presence of hydrophobic contamination in the buffer. We checked the purity of our buffers (either origami working buffer or origami folding buffer) on HOPG. A typical AFM image of a freshly cleaved HOPG surface is shown in panel (a). We deposited droplets of our buffer solutions onto such HOPG surface, rinsed it with MQ water, and imaged the surface to detect any hydrophobic residues. Panel (b) shows that our buffers are indeed very clean and do not leave any contaminants on HOPG surface. Panel (c) is a typical image of as-folded origami sample (which still contains excess oligos) onto HOPG. Due to exposed hydrophobic bases of single-stranded staples, they show a higher affinity towards HOPG surface compared to the origami plate [36]. Therefore, these staples bind to HOPG first, followed by adsorption of the origami plates afterwards. Without these staples, origami plates interact with HOPG and lose their structural integrity (panel d).

2.5.4. Graphene CVD growth and Raman spectroscopy

High-quality monolayer graphene was grown on 25 um thick Cu foils (99.8%, Alfa Aesar) using a LPCVD method that we demonstrated previously [37]. Briefly, the Cu foil (2 × 8 cm) was loaded into a CVD chamber. Under low pressure (1.5 Torr), the textured Cu foil was annealed in a gas flow of 50 standard cubic centimeters (sccm) of hydrogen (H2) at 1000 °C for 60 min. After the annealing step, 6 sccm of methane (CH4) gas was introduced to initiate the graphene growth for 40 minutes. The graphene growth was carried out at 1000 °C. To control the graphene growth rate, 20 sccm of H2 flow was used during the growth period. Once the growth was finished, the CVD chamber was cooled down under 20 sccm of H2 to prevent oxidation and to minimize hydrogenation reactions of the graphene. The Raman measurement was carried out using a Horiba-Jobin Yvon system with a 532 nm Ar+ laser line. The laser power used is around 1 mW on the sample and a 100× objective was used to focus the beam. The size of the laser beam on the sample is around 1 µm. Raman spectroscopy was used to investigate the quality of the single-layer graphene on the Cu foil using a 532 nm laser excitation. As indicated in Figure S2.4, the graphene on a SiO2/Si wafer shows a typical monolayer Raman spectrum with two typical G- and 2D-bands at 1590 and 2675 cm^{-1}, respectively with a ratio of integrated peak intensities (I2D/IG) larger than 2.0 [38].

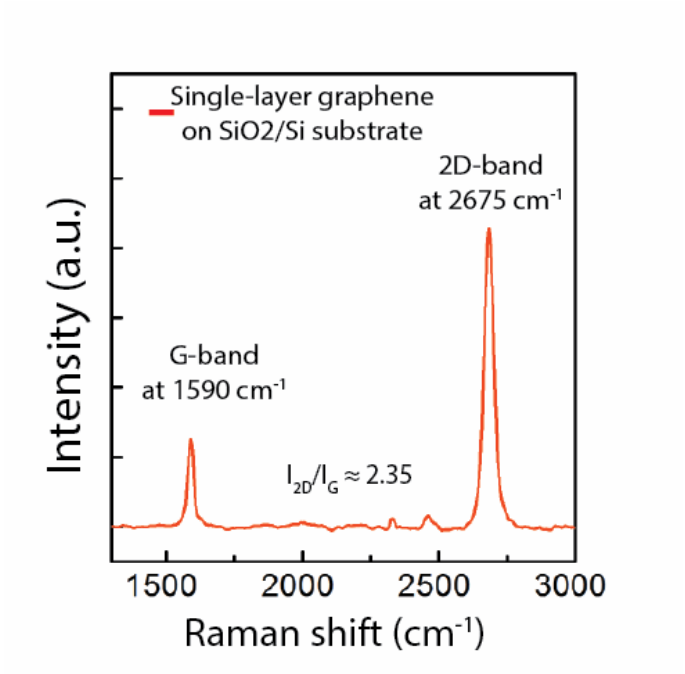

Figure S2.4: Raman spectroscopy for the CVD-grown graphene transferred onto SiO2/Si substrate depicting the typical spectrum for single-layer graphene.

2.5.5. Polymer-free graphene transfer

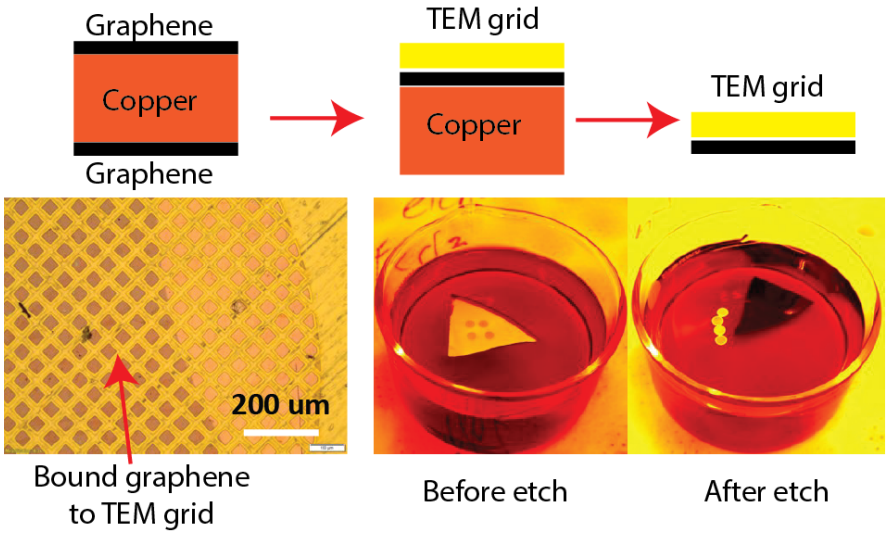

Figure S2.5: Graphene transfer via a polymer-free method. The sequence of transfer is as follows: 1) After CVD growth, both sides of copper foil is covered with graphene. We removed one side using FeCl3 (Sigma Aldrich) for 5 minutes. Copper foil is then washed thoroughly several times with MQ water (18.2 MΩ). 2) The carbon side of the TEM grids (Quantifoil® 200-mesh size, Au-coated) is placed onto the graphene side of the copper foil and several droplets of isopropylalcohol (IPA) are gently applied. When IPA evaporates, it binds the graphene to the carbon layer of the TEM grid through capillary forces. 3) The bound TEM grids to copper are then transferred to the metal etching bath (FeCl3), where the copper is removed. 4) The graphene-coated TEM grids are then picked up gently using a tweezer and washed several times with MQ water. Following this procedure, we achieve free-standing single-layer graphene spanning over 1-2 µm apertures in the perforated carbon film, covering almost 80% of each TEM grid.

2.5.6. TEM quality characterization of free-standing graphene

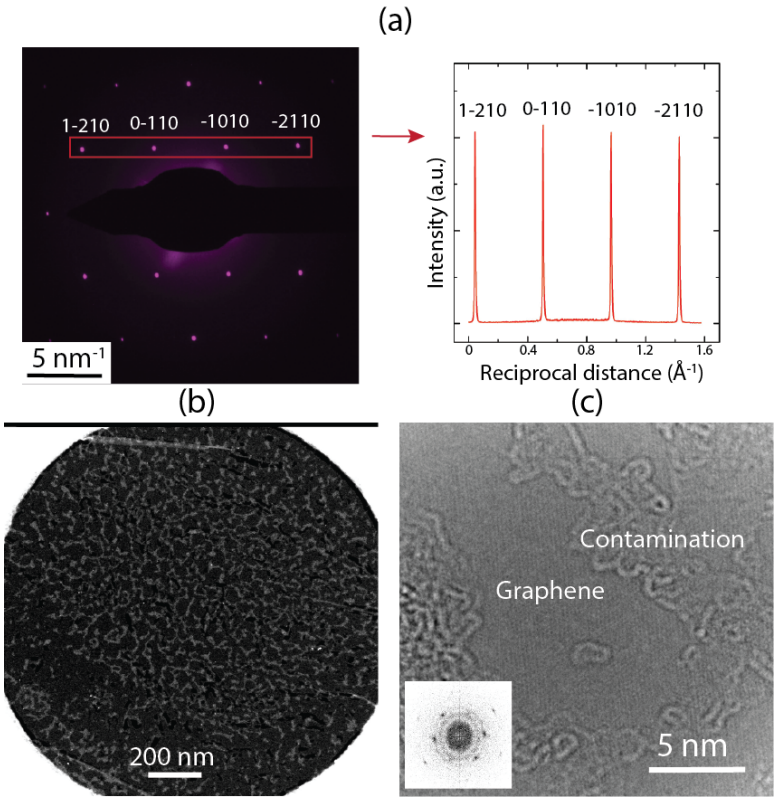

Figure S2.6: Complementary TEM characterization techniques to determine cleanness and number of layers for the graphene coated TEM grids. (a) A typical selected-area electron diffraction (SAED) pattern of single-layer graphene. Due to continuous rod shape of the reciprocal lattice points for the monolayer graphene, the intensity ratio between the 10-10 and 11-20 reflections is equal across different tilt angles [39]. In accord with the Raman data, we find mostly single-layer membranes. But the presence of AA or AB stacked multilayer, turbostratic, or graphene scrolls was also notable in the microscopic investigations. (b) STEM overview image of the single-layer graphene membrane. The contrast is stretched to show the bound contamination. We do not find any un-etched copper after the graphene transfer since the intensity within the circular aperture is always smaller than the carbon layer (the white corners in the panel). (c) A typical HRTEM image of monolayer graphene taken at 300 kV. Inset shows the FFT of the HRTEM image with the pronounced graphene reflections. Hydrocarbon contaminations are discernable from the graphene lattice.

2.5.7. Origami design

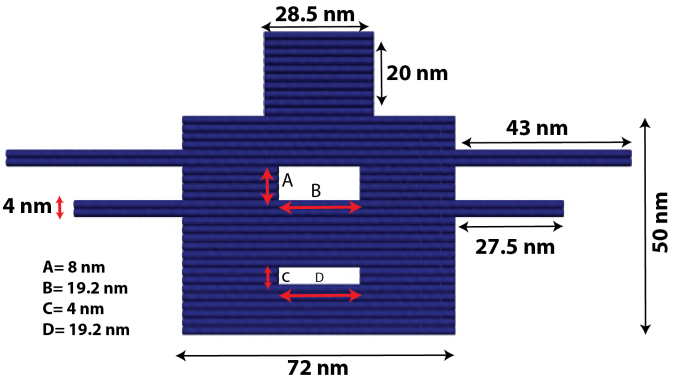

Figure S2.7: Detailed scheme of our origami design

2.5.8. Excess-staples purification

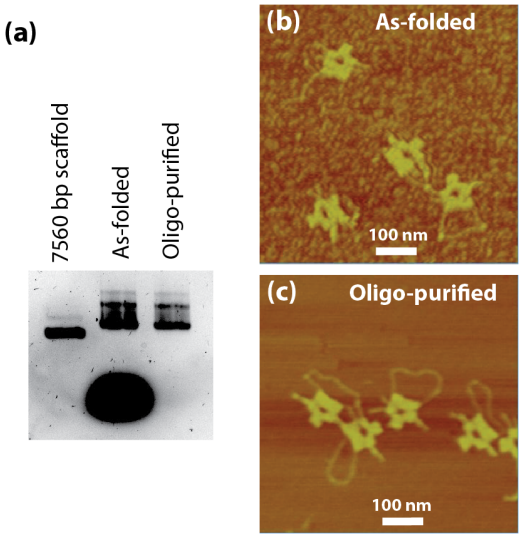

Figure S2.8: Gel electrophoresis (a) together with AFM images of as-folded (b) and staple-purified origami samples (c) on mica under dry conditions. Excess staples are visible on the mica surface for the as-folded sample.

2.5.9. DF aperture fabrication

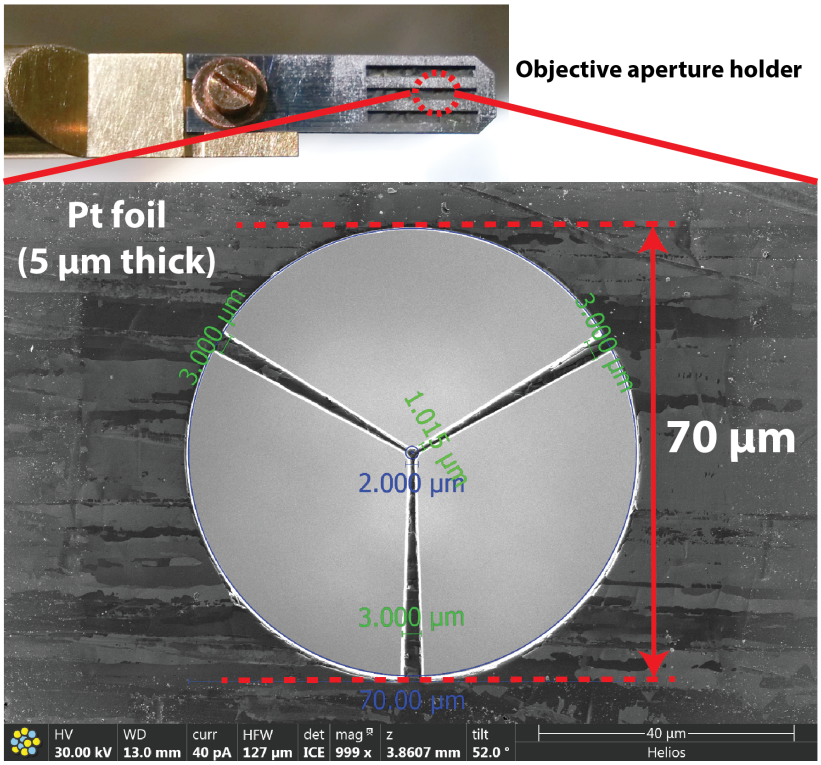

Figure S2.9: Delicate DF aperture fabricated using a FIB Helios microscope. Three-legged "Mercedes star" geometry proved to be useful in avoiding electron charge built-up, which causes image drift. The aperture was milled inside the objective lens cassette holder. SEM image shows a very smooth finish after the ion milling. Milling was done using a semi-automated CAD-assisted software in Helios platform. Afterwards, the whole cassette was immersed in nitric acid for 5 minutes and subsequently rinsed thoroughly with MQ water prior to insertion into the Titan microscope. This was done since contaminants will cause charging on the aperture, which consequently cause drift or instability during imaging. Diameter of the aperture (70 µm) was chosen based on calibration with a silicon sample in order to correspond to a 1-Å-information cutoff.

2.5.10. Electron optical comparison between STEM and DF

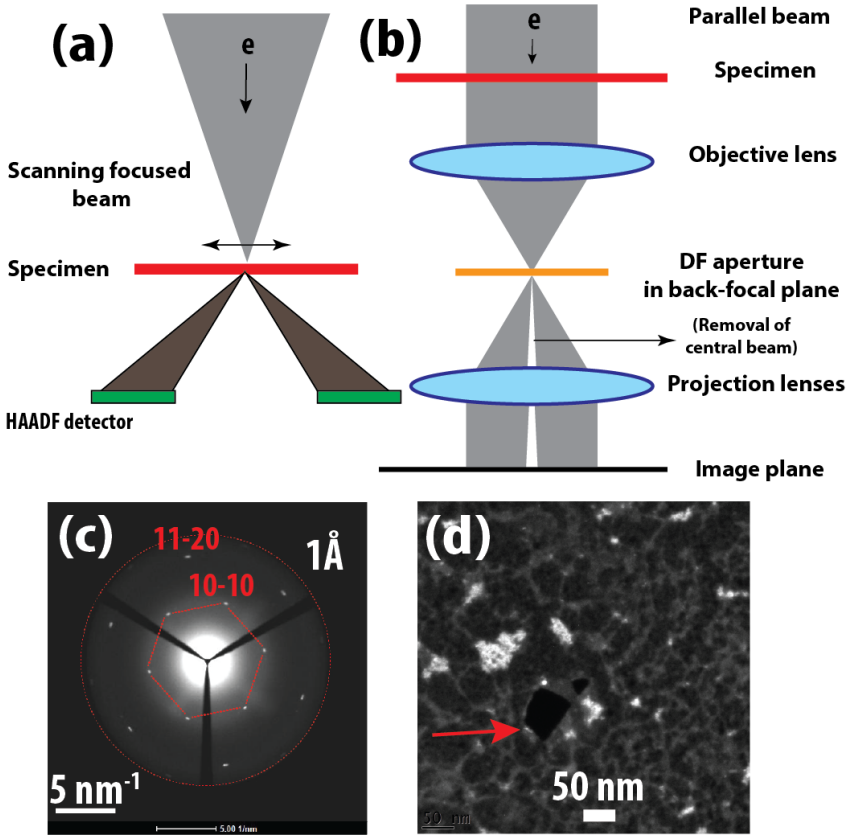

Figure S2.10: (a) Electron-ray diagram for STEM, where a highly focused electron beam (2 Å in diameter) raster above the sample, and the corresponding intensity for each pixel is collected by HAADF detector to form the image. (b) For DF, a very parallel illumination is provided by the condenser lens system of Titan microscope. Contrast enhancement happens at the back-focal plane of the objective lens, where we insert our custom-made DF aperture. (c) Electron diffraction pattern of monolayer graphene while the aperture is inserted in the back-focal plane. The contrast was stretched to depict the graphene reflections. The outer diameter of the aperture cuts the graphene 200 reflections in reciprocal space, indicating an information cutoff of about an Angstrom in real space. (d) DF image of the corresponding diffraction pattern in (c). We can distinguish graphene from the white hydrocarbon contaminants together with a rupture area inside the continuous graphene layer indicated by an arrow.

2.5.11. Contrast enhancement using DF

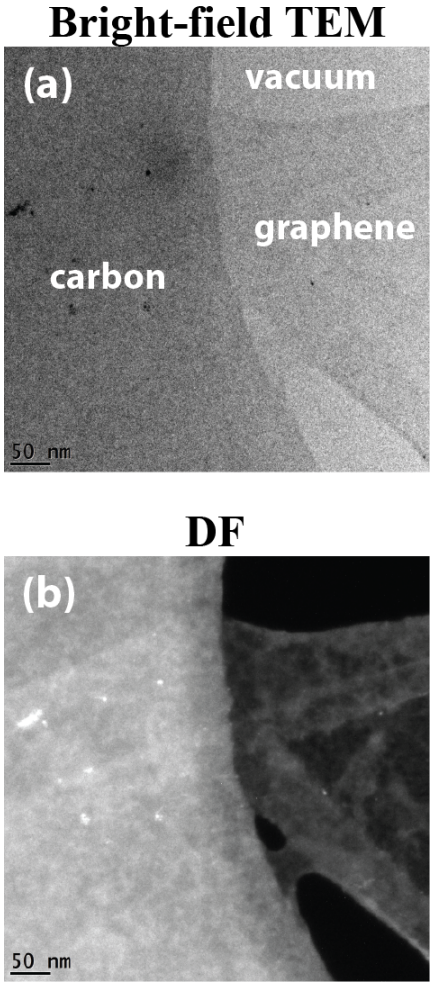

Figure S2.11: The DF aperture boosts the in-focus contrast. (a) A typical bright-field TEM image of the transferred graphene onto TEM grids (b) The same area imaged with DF technique. The edges and the thickness variations in graphene become readily visible using the DF technique.

2.5.12. Effect of spherical aberration and focus on DF images

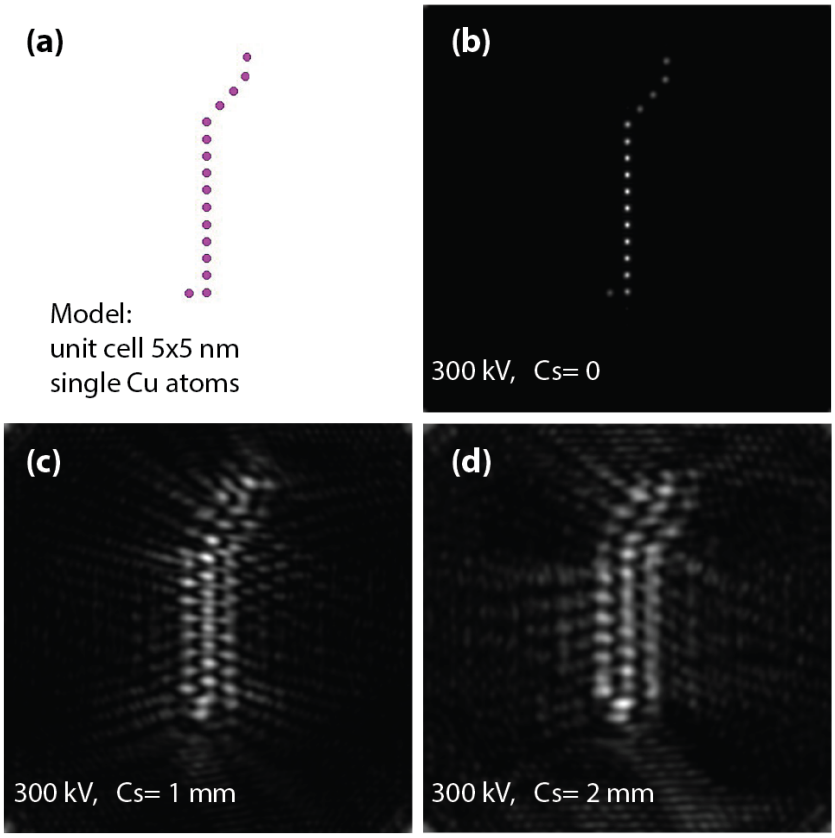

Figure S2.12: Image simulations (using MacTempas package) to evaluate the effect of spherical aberration on the DF images. (a) The model is composed of copper atoms in a 5x5 nm unit cell. (b-d) DF simulated images with Cs=0, Cs=1 mm, and Cs=2mm respectively. Contrast is stretched in panels (c-d). Best imaging condition with lowest delocalization is achieved with a Cs-corrected microscope (panel b). Hence, using a Cs-corrected microscope (such as FEI Titan) is necessary for the DF technique.

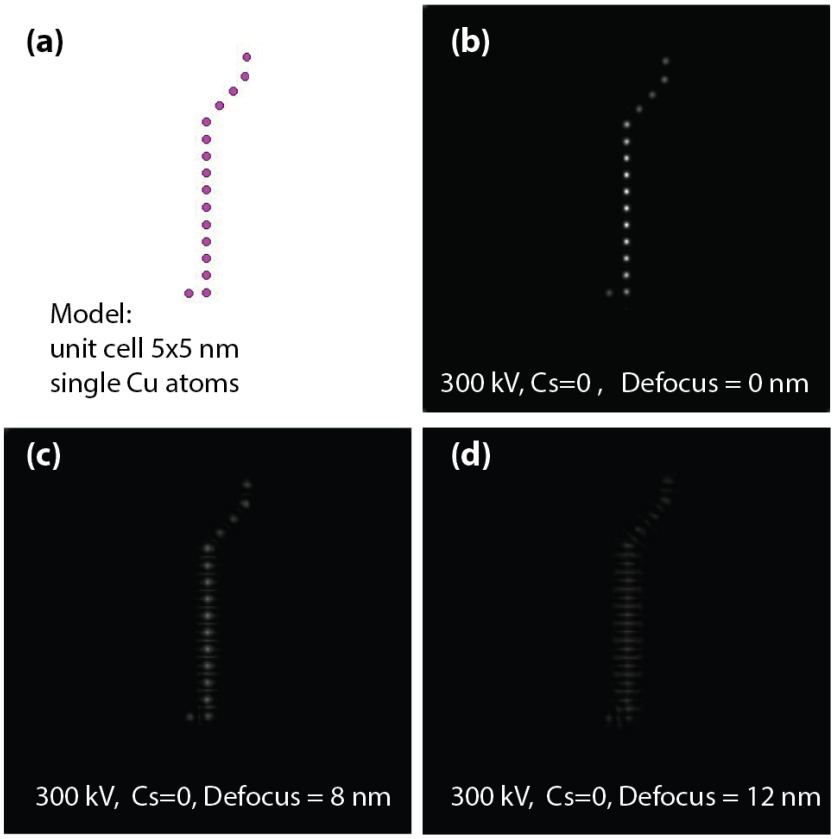

Figure S2.13: Similar image simulations as discussed in Figure S2.12, but now evaluating the effect of focus on the DF images. The defocus ranges from zero in (a) to +12 nm in (d). No contrast stretching is performed on the panels. It is clear that DF images are very sensitive to defocus variations and the highest contrast is achieved at zero focus.

2.5.13. Nanoplate finite-element simulations

To test the mechanical stability of the origami plates, we used the CanDo simulation package (http://cando.dna-origami.org/). CanDo uses a finite-element method to model different constituents of the origami (base pairs, staple oligos, cross-overs, and scaffold strand) with different geometric and material parameters, in which the cross-overs serve as rigid constraints. Upon application and removal of external forces, CanDo generates local root-mean-square fluctuations (RMSF) as a heatmap onto the structure. This heatmap is a fingerprint of the local flexibility, which helps to better understand the basic mechanical properties of the design such as bending and twist. One such heatmap for our structure is shown in Figure S2.14, where we see a high local flexibility at the corners of the structure as well as in the side arms and DNA loop at the bottom. Whereas 3D origami objects can be extremely rigid [33], a high floppiness is quite expected for their 2D counterparts, which is due to square-lattice routing. This is unlikely to be the source of distortion of origami on the graphene since we always see flat structures on our carbon membranes (Figure 2.3). Moreover, it has been shown that twist deformations vanish after the origami plates are electrostatically immobilized on the surface [33].

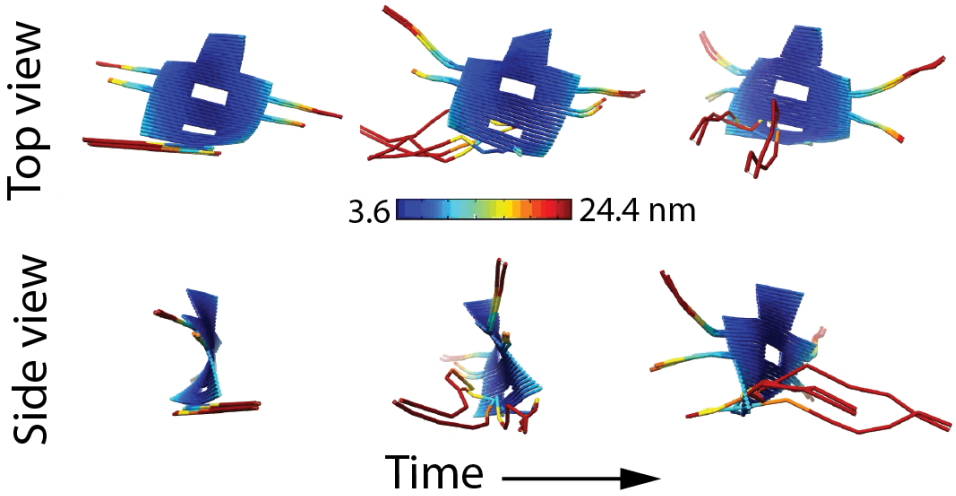

Figure S2.14: The floppy nature of our 2D DNA origami nanoplates simulated with computer modeling (CanDo package). This high flexibility is inherent to the 2D origami designs.

2.5.14. Oligomer sequences

Please see the online version of the SI for the complete oligomer sequences.

References

[1] R. Westervelt, *Graphene nanoelectronics,* Science **320**, 324 (2008).

[2] Y. Liu, X. Dong, and P. Chen, *Biological and chemical sensors based on graphene materials,* Chemical Society Reviews **41**, 2283 (2012).

[3] J. Jeon, M. S. Lodge, B. D. Dawson, M. Ishigami, F. Shewmaker, and B. Chen, *Superb resolution and contrast of transmission electron microscopy images of unstained biological samples on graphene-coated grids,* Biochimica et Biophysica Acta (BBA)-General Subjects **1830**, 3807 (2013).

[4] R. S. Pantelic, J. W. Suk, C. W. Magnuson, J. C. Meyer, P. Wachsmuth, U. Kaiser, R. S. Ruoff, and H. Stahlberg, *Graphene: Substrate preparation and introduction,* Journal of structural biology **174**, 234 (2011).

[5] R. Zan, Q. M. Ramasse, R. Jalil, T. Georgiou, U. Bangert, and K. S. Novoselov, *Control of radiation damage in mos2 by graphene encapsulation,* ACS nano **7**, 10167 (2013).

[6] C. Wang, Q. Qiao, T. Shokuhfar, and R. F. Klie, *High-resolution electron microscopy and spectroscopy of ferritin in biocompatible graphene liquid cells and graphene sandwiches,* Advanced Materials **26**, 3410 (2014).

[7] M. R. Jones, N. C. Seeman, and C. A. Mirkin, *Programmable materials and the nature of the dna bond,* Science **347**, 1260901 (2015).

[8] S. Woo and P. W. Rothemund, *Programmable molecular recognition based on the geometry of dna nanostructures,* Nature chemistry **3**, 620 (2011).

[9] P. W. Rothemund, *Folding dna to create nanoscale shapes and patterns,* Nature **440**, 297 (2006).

[10] S. M. Douglas, A. H. Marblestone, S. Teerapittayanon, A. Vazquez, G. M. Church, and W. M. Shih, *Rapid prototyping of 3d dna-origami shapes with cadnano,* Nucleic acids research **37**, 5001 (2009).

[11] J. D. Griffith, S. Lee, and Y.-H. Wang, *Visualizing nucleic acids and their complexes using electron microscopy,* Current opinion in structural biology **7**, 362 (1997).

[12] M. Marini, A. Falqui, M. Moretti, T. Limongi, M. Allione, A. Genovese, S. Lopatin, L. Tirinato, G. Das, B. Torre, *et al.*, *The structure of dna by direct imaging,* Science advances **1**, e1500734 (2015).

[13] M. Marini, T. Limongi, A. Falqui, A. Genovese, M. Allione, M. Moretti, S. Lopatin, L. Tirinato, G. Das, B. Torre, *et al.*, *Imaging and structural studies of dna–protein complexes and membrane ion channels,* Nanoscale **9**, 2768 (2017).

[14] F. Gentile, M. Moretti, T. Limongi, A. Falqui, G. Bertoni, A. Scarpellini, S. Santoriello, L. Maragliano, R. Proietti Zaccaria, and E. di Fabrizio, *Direct imaging of dna fibers: the visage of double helix,* Nano Letters **12**, 6453 (2012).

[15] S. Buckhout-White, J. T. Robinson, N. D. Bassim, E. R. Goldman, I. L. Medintz, and M. G. Ancona, *Tem imaging of unstained dna nanostructures using suspended graphene,* Soft Matter **9**, 1414 (2013).

[16] K. Nagayama and R. Danev, *Phase contrast electron microscopy: development of thin-film phase plates and biological applications,* Philosophical Transactions of the Royal Society B: Biological Sciences **363**, 2153 (2008).

[17] B. J. Pages, D. L. Ang, E. P. Wright, and J. R. Aldrich-Wright, *Metal complex interactions with dna,* Dalton transactions **44**, 3505 (2015).

[18] R. Erni, *Aberration-corrected imaging in transmission electron microscopy: an introduction* (World Scientific Publishing Company, 2010).

[19] R. F. Egerton, F. Wang, and P. A. Crozier, *Beam-induced damage to thin specimens in an intense electron probe,* Microscopy and microanalysis **12**, 65 (2006).

[20] P. A. Midgley, M. Weyland, J. M. Thomas, and B. F. Johnson, *Z-contrast tomography: a technique in three-dimensional nanostructural analysis based on rutherford scattering,* Chemical Communications , 907 (2001).

[21] R. M. Glaeser, *Limitations to significant information in biological electron microscopy as a result of radiation damage,* Journal of ultrastructure research **36**, 466 (1971).

[22] C. Zhang, Q. Xu, P. J. Peters, and H. Zandbergen, *The use of a central beam stop for contrast enhancement in tem imaging,* Ultramicroscopy **134**, 200 (2013).

[23] R. Egerton, P. Li, and M. Malac, *Radiation damage in the tem and sem,* Micron **35**, 399 (2004).

[24] G. Algara-Siller, S. Kurasch, M. Sedighi, O. Lehtinen, and U. Kaiser, *The pristine atomic structure of mos2 monolayer protected from electron radiation damage by graphene,* Applied Physics Letters **103**, 203107 (2013).

[25] R. M. Glaeser, *How good can cryo-em become?* Nature methods **13**, 28 (2015).

[26] G. Algara-Siller, O. Lehtinen, A. Turchanin, and U. Kaiser, *Dry-cleaning of graphene,* Applied Physics Letters **104**, 153115 (2014).

[27] B. S. Husale, S. Sahoo, A. Radenovic, F. Traversi, P. Annibale, and A. Kis, *ssdna binding reveals the atomic structure of graphene,* Langmuir **26**, 18078 (2010).

[28] N. S. Green and M. L. Norton, *Interactions of dna with graphene and sensing applications of graphene field-effect transistor devices: A review,* Analytica chimica acta **853**, 127 (2015).

[29] W. Liu, H. Zhong, R. Wang, and N. C. Seeman, *Crystalline two-dimensional dna-origami arrays,* Angewandte Chemie International Edition **50**, 264 (2011).

[30] R. Campos, S. Zhang, J. Majikes, L. Ferraz, T. LaBean, M. Dong, and E. Ferapontova, *Electronically addressable nanomechanical switching of i-motif dna origami assembled on basal plane hopg,* Chemical Communications **51**, 14111 (2015).

[31] J. M. Yun, K. N. Kim, J. Y. Kim, D. O. Shin, W. J. Lee, S. H. Lee, M. Lieberman, and S. O. Kim, *Dna origami nanopatterning on chemically modified graphene,* Angewandte Chemie International Edition **51**, 912 (2012).

[32] R. S. Pantelic, W. Fu, C. Schoenenberger, and H. Stahlberg, *Rendering graphene supports hydrophilic with non-covalent aromatic functionalization for transmission electron microscopy,* Applied physics letters **104**, 134103 (2014).

[33] C. E. Castro, F. Kilchherr, D.-N. Kim, E. L. Shiao, T. Wauer, P. Wortmann, M. Bathe, and H. Dietz, *A primer to scaffolded dna origami,* Nature methods **8**, 221 (2011).

[34] W. Regan, N. Alem, B. Alemán, B. Geng, Ç. Girit, L. Maserati, F. Wang, M. Crommie, and A. Zettl, *A direct transfer of layer-area graphene,* Applied Physics Letters **96**, 113102 (2010).

[35] D. Nečas and P. Klapetek, *Gwyddion: an open-source software for spm data analysis,* Open Physics **10**, 181 (2012).

[36] V. C. Sanchez, A. Jachak, R. H. Hurt, and A. B. Kane, *Biological interactions of graphene-family nanomaterials: an interdisciplinary review,* Chemical research in toxicology **25**, 15 (2011).

[37] Y. C. Shin and J. Kong, *Hydrogen-excluded graphene synthesis via atmospheric pressure chemical vapor deposition,* Carbon **59**, 439 (2013).

[38] A. C. Ferrari, J. Meyer, V. Scardaci, C. Casiraghi, M. Lazzeri, F. Mauri, S. Piscanec, D. Jiang, K. Novoselov, S. Roth, *et al., Raman spectrum of graphene and graphene layers,* Physical review letters **97**, 187401 (2006).

[39] J. Meyer, A. Geim, M. Katsnelson, K. Novoselov, D. Obergfell, S. Roth, C. Girit, and A. Zettl, *On the roughness of single-and bi-layer graphene membranes,* Solid State Communications **143**, 101 (2007).

3

Intercalating electron dyes for TEM visualization of DNA at the single-molecule level

Don't make people feel stupid, drop the jargon.

Anonymous

Staining compounds containing heavy elements (electron dyes) can facilitate the visualization of DNA and related biomolecules using transmission electron microscopy (TEM). However, research on the synthesis and utilization of alternative electron dyes has been limited. Here, we report the synthesis of a novel DNA intercalator molecule, bis-acridine uranyl (BAU). Nuclear magnetic resonance (NMR) spectroscopy and mass spectrometry (MS) confirmed the validity of our synthesis scheme and gel electrophoresis verified the binding of BAU to DNA. For TEM imaging of DNA, we use two-dimensional DNA origami nanostructures as a robust microscopy test object. Using scanning TEM (STEM) imaging, which is favored over conventional wide-field TEM for improved contrast and therefore quantitative image analysis, we find that the synthesized BAU intercalator can render DNA visible, even at the single-molecule scale. For comparison, we also evaluated other staining compounds with a purported affinity towards DNA, such as dichloro platinum, cisplatin, osmium tetroxide, and uranyl acetate. We discuss the STEM contrast in terms of the DNA-dye association constants, number of dye molecules bound per base pair, and the electron-scattering capacity of the metal-containing ligands. Our findings pave the way for future development of electron dyes with specific DNA-binding motifs for high-resolution TEM imaging.

This chapter has been published as: Yoones Kabiri, Alessandro Angelin, Ishtiaq Ahmed, Hatice Mutlu, Jens Bauer, Christof M. Niemeyer, Henny Zandbergen, Cees Dekker, Intercalating electron dyes for TEM visualization of DNA at the single-molecule level, ChemBioChem, 20, 2019.

3.1. Introduction

Unstained DNA and related biomolecules contain mostly light elements such as carbon, nitrogen, and phosphorous, that all have low electron scattering strength. As a result, high-resolution TEM imaging of unstained single DNA molecules supported on commercial carbon supports has been unsuccessful because when the electron wave passes through DNA, only negligible changes occur to its amplitude or phase, which consequently leaves the unstained DNA invisible under TEM. The use of electron dyes is therefore a stringent requirement for increasing the electron scattering and hence the TEM visualization of DNA.

Surprisingly, despite the pressing need for DNA-staining compounds, there is a historical gap in the systematic investigation of effective and accessible electron dyes, as uranyl acetate and its analogues monopolized as the only DNA stain since 1961 [1]. It binds covalently to the negatively charged backbone of DNA [1], and with the heavy atomic number of 92 for the uranium element, it provides excellent electron scattering in TEM. Practically, the use of uranyl acetate is not ideal, since it is extremely toxic and its access needs governmental permissions due to tight restrictions on nuclear fuel materials. It is well known that the DNA-binding mode, and consequently the cellular response to compounds changes with even slight modifications in the coordination chemistry of the transition metals [2]. Hence, from a biochemistry point of view, it remains an interesting question whether it would be possible to engineer a synthetic compound with the compatible uranium core element for providing excellent TEM contrast, but with an intercalation binding mode rather than covalent attachment to the DNA phosphate backbone.

Can intercalation be utilized for TEM imaging of DNA? The design or application of intercalating molecules containing heavy elements as electron dyes has been very limited so far. For example, although many DNA-binding compounds that contain heavy elements (Pt, Ag, Au, etc.) are conceivable, only platinum has gained attention due to its rich library of coordination chemistry. Indeed, since the first successful application of cisplatin as an anticancer agent, the field of synthetic Pt compounds has evolved exponentially [2, 3]. Cisplatin is a covalent DNA binder, whereas other Pt complexes especially those containing a planar aromatic terpyridine moieties, are intensively studied DNA intercalators, owing to their vast therapeutic applications in chemotherapy and cancer treatment [3–6]. In addition, it has recently been shown that some derivatives of Pt complexes can penetrate into the cell nucleus and show cell viability [4, 6, 7]. This grants them a clear advantage for TEM imaging applications of biological samples. However, despite these promising intercalation properties, no TEM visualization of single-DNA molecules has been reported so far through intercalation binding of platinum or any other heavy elements such as uranium.

Two major drawbacks have impeded the progress towards the systematic investigation of contrast agents for TEM visualization of DNA: (i) demanding and sometimes ambiguous sample preparations, and (ii) non-optimized choices for the TEM imaging mode. With regards to the first point, most reports in the literature use plastic-embedded tissue sections or viruses as the model system for microscopic investigations [8, 9]. Apart from tedious sample preparation, artifacts often affect the results due to the crowded environment (presence of proteins, lipids, DNAs, etc.) [10]. The second drawback is as-

sociated with inherently noisy TEM images, even for stained DNA. Due to the faint signal of DNA, contaminations or the substrate signal often interfere with the imaging and reduce the obtained DNA contrast. Accordingly, reliable and quantitative analysis of DNA images has proven to be difficult and sometimes impossible.

Here, we present a novel intercalating agent which is synthesized by covalently tethering a bis-acridine moiety to a salophen ligand, i.e., Schiff base, that functions as a chelator for an uranium atom (Figure 3.1). We fully characterized our synthesized intercalator by means of NMR, MS, and gel electrophoresis. We then present our TEM investigations. To overcome the sample preparation problems, we utilized a well-defined DNA origami nanostructure as a microscopic test model system for TEM imaging (Figure 3.2). DNA origami, i.e., DNA that is folded into a user-defined shape [11], provides a facile and straightforward approach to directly evaluate the stained DNA and strongly reduces the above-mentioned sample-preparation challenges, as the characteristic shape of the origami design facilitates the detection and the quantitative analysis of the DNA contrast. Furthermore, we significantly improve the TEM imaging by using the scanning TEM (STEM) technique. STEM is advantageous over conventional wide-field TEM since it provides higher signal-to-noise-ratio (SNR) for single image acquisitions. Indeed, STEM enabled us to quantitatively analyze the DNA contrast stained with different DNA-binding electron dyes including our synthesized bis-acridine uranyl as well as other compounds reported in the literature such as the Dichloro platinum (Pt intercalator), cisplatin, and osmium tetroxide.

3.2. Results

Synthesis, characterization, and binding properties of BAU to DNA

Intercalators are widely applied in analytical and medical chemistry [12], and they offer the potential for tailoring the surface properties of DNA nanostructures [13]. Inspired by the wide range of useful properties of acridine derivatives, and in continuation of efforts for expanding its applications as staining agents, we synthesized (Figure 3.1) a novel bidentate intercalator compound bis-acridine uranyl (BAU) that contains one uranyl cation confined inside the chelating salophen moiety in the center of its structure, which acts as a TEM-contrast enhancer. This unit is tethered to two acridine heterocycles (bis-acridine), that serve as DNA-intercalating ligands. The linker strategy for tethering the bis-acridine moiety to the uranium metal center was adopted from the salophen-type coordination chemistry [14]. The full description of the experimental procedures for the synthesis of BAU is given in the experimental section and supporting information (SI).

NMR spectroscopy and mass spectrometry confirmed the structure of BAU, and validated our synthesis scheme. Proton and carbon chemical shifts of BAU were assigned upon standard 1D and 2D NMR characterization (Figures 3.3-3.4). Specifically, the 2D NMR measurements (Figure 3.4) allowed assigning the spin systems corresponding to the following structural patterns: the salophenUO2 complex, the acridine moiety, and the connecting hexyl spacer. In particular, the signal of the magnetic resonances attributable to the azomethine groups of the salophen-UO2 complex was observed at 9.60 ppm, while the significant magnetic resonances for the three phenyl rings bridged by these azomethine groups appeared in the range of 7.22–6.56 ppm. The signals corre-

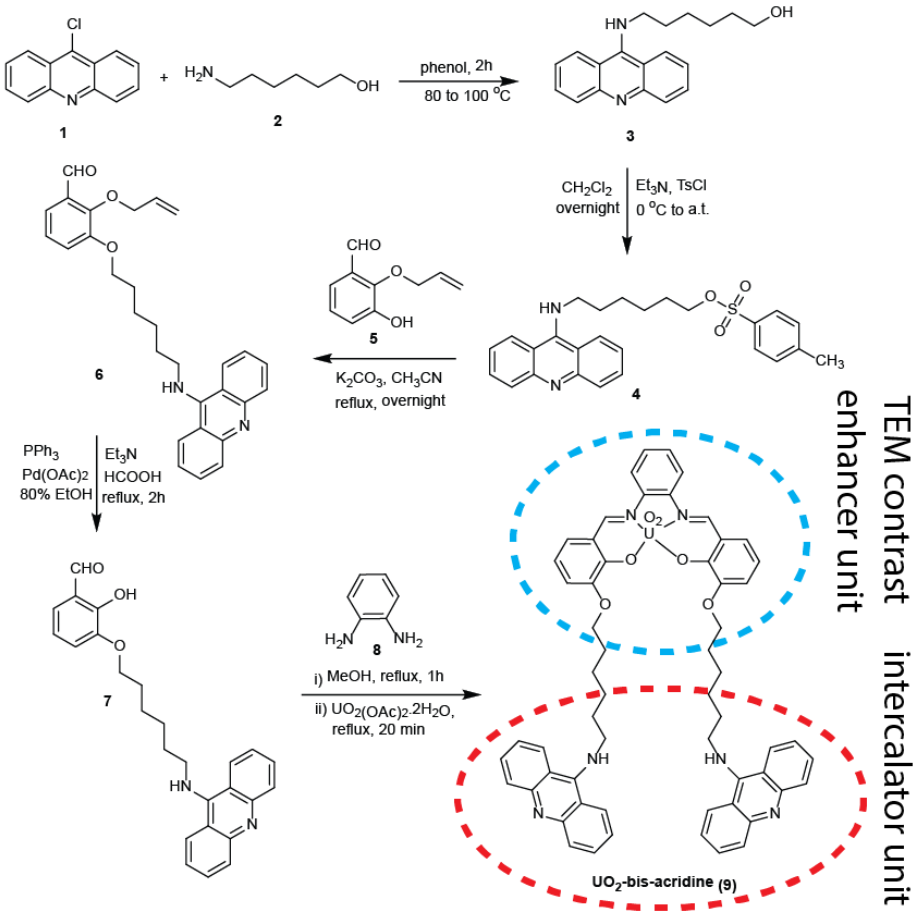

Figure 3.1: Synthetic scheme of bis-acridine uranyl (BAU). The complete protocols for the synthesis are given in the SI.

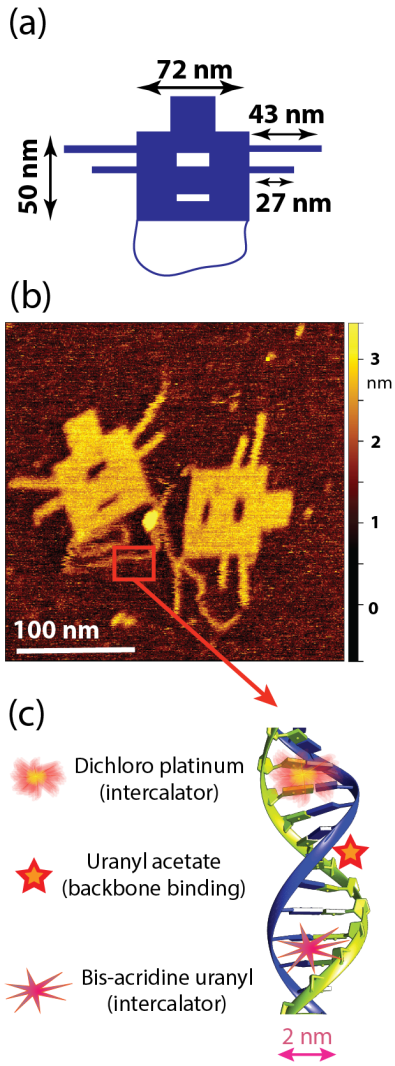

Figure 3.2: DNA origami structures as a robust and straightforward microscopic model specimen to probe various TEM contrast agents for DNA visualization. (a) Schematic representation of our 2D DNA origami design with various features such as cavities in the main rectangle, side arms (2 DNA helices, 4 nm wide), and an individual dsDNA loop at the bottom (2 nm wide). (b) Liquid-cell atomic force microscopy images of the DNA nanoplates on mica. (c) Schematic illustration of the binding sites for the compounds discussed in the manuscript.

sponding to the aromatic pattern of the acridine moiety were assigned in the range of 8.45-7.30 ppm. The presence of the hexyl chain spacer, was confirmed by the magnetic resonances of the CH2 groups attached to the phenyl-group of the salophenUO2 complex and the amino-group at the 9-position of acridine, which were underpinned at 4.15 and 3.93 ppm, respectively. We refer to Figures S3.1-S3.5 in the SI for further 1H and 13C NMR characterization of the intermediate synthesized compounds (i.e. compounds 3-7). The complementary characterization of the exact mass by high-resolution ESI-MS confirmed the formation of the targeted BAU (Figure 3.3b). Based on the thorough structure confirmation by NMR and ESI-MS, we thus explicitly showed the feasibility of synthesizing a metallointercalator molecule associating a very heavy element such as uranium.

As a prerequisite to use BAU as a DNA electron dye, it should bind strongly to DNA. We performed gel electrophoresis to evaluate the bulk binding properties of BAU to DNA origami nanostructures (Figure 3.5). DNA origami nanostructures, containing fluorescent Cy5-labeled staple strands, were incubated with variable molar ratios of BAU to DNA base pairs, starting from an excess value of 5 BAU/bp to lower ratios down to 0.05 BAU/bp, as calculated from the scaffold length of the DNA origami. Visualization of the origami nanostructures was achieved by fluorescent imaging of the Cy5 fluorophores as well as by staining with SYBR gold. Figure 3.5 shows the data and elucidates two important points: (i) a close look at the immobile band indicated inside the dashed white rectangles reveals an increasing intensity in the SYBR gold channel with lower BAU concentration, but a uniform intensity in Cy5 channel. This suggests that BAU competitively inhibits the binding of SYBR gold to DNA nanoplates, most likely through intercalation. Our observation is consistent with the general consensus that bis-acridine moieties are indeed excellent intercalators [15, 16]. (ii) BAU binding alters the electrophoretic mobility of the DNA origami, as we observe that the origami structures become completely immobilized inside the gel pockets (lanes 1 to 4), and can only acquire partial mobility below stoichiometric ratios of 0.5 BAU/bp (lanes 5 and 6). This is attributed to both the positive charge of BAU and inter-origami cross-linking that can occur when the two acridine intercalating units of BAU bind to two different origami plates. Indeed, TEM images taken from these complexes confirmed such BAU-induced origami interaction (see Figure S3.6 in the SI). Collectively, the results of the electrophoretic analysis indicate that BAU binds tightly to DNA, thereby suggesting its potential to be used as a DNA electron dye.

TEM imaging

We find that it is not possible to image the stained DNA nanostructures with high contrast in wide-field TEM, even with a state-of-the-art direct detection device (DDD). In the past years, the field of TEM has gone through a dramatic improvement in instrumentation, especially due to the emergence of DDD technology. With eliminating the scintillator layer, the DDDs became advantageous over the conventional CCD cameras since they yield a higher dynamical range, higher detective quantum efficiency for all spatial frequencies up to Nyquist limit, sample-motion correction, and a lower shot noise [17]. As the improvements in the detector would be beneficial to boost the contrast in wide-field TEM, a recent state-of-the-art DDD (Model: DE16, Direct Electron, Califor-

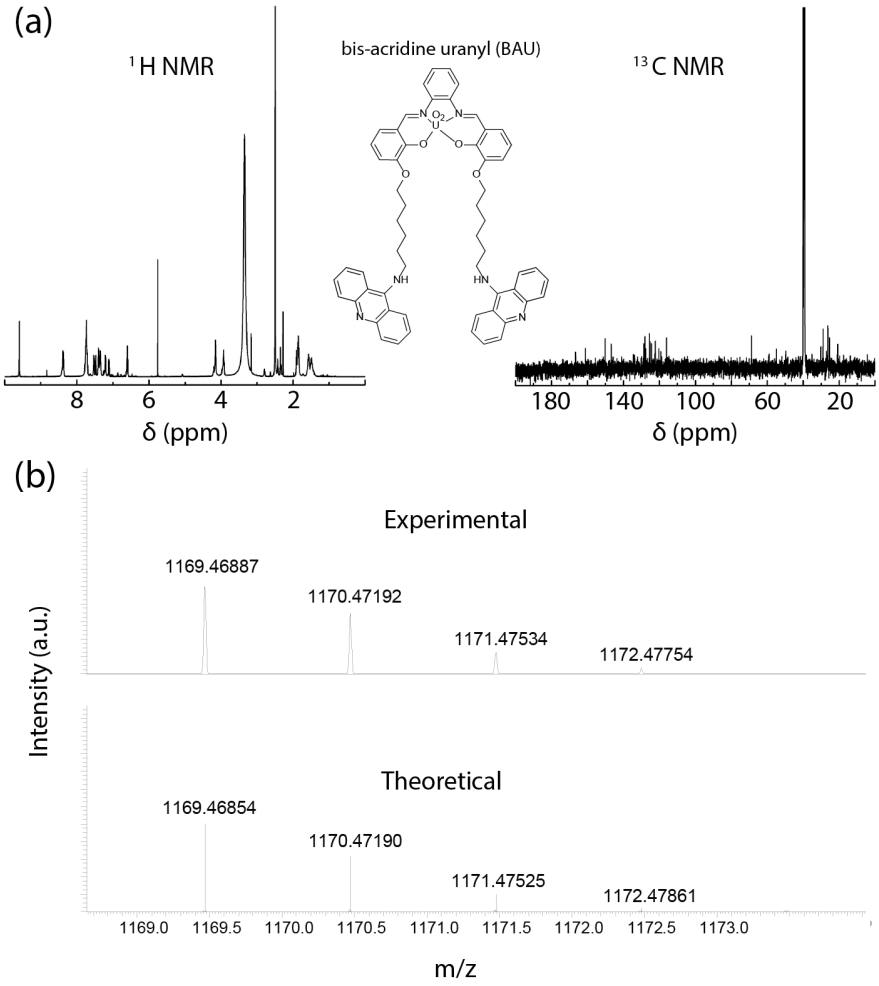

Figure 3.3: (a) 1D NMR (solvent: DMSO) and (b) comparison of experimentally obtained spectrum (positive ion mode) and simulated isotopic patterns of bis-acridine uranyl. Experimental m/z for [M+H]+ was 1169.4689, matching the theoretical value of 1169.4685.

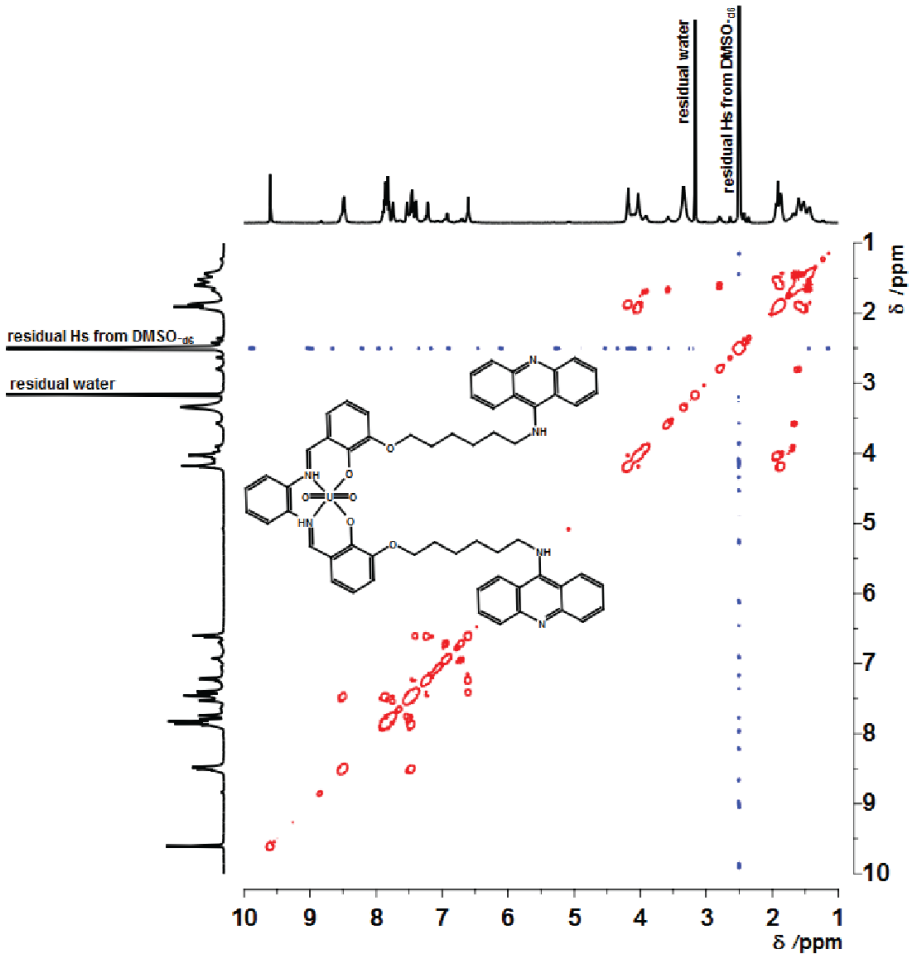

Figure 3.4: 2D COSY NMR spectrum (400 MHz, DMSOd6) of bis-acridine uranyl.

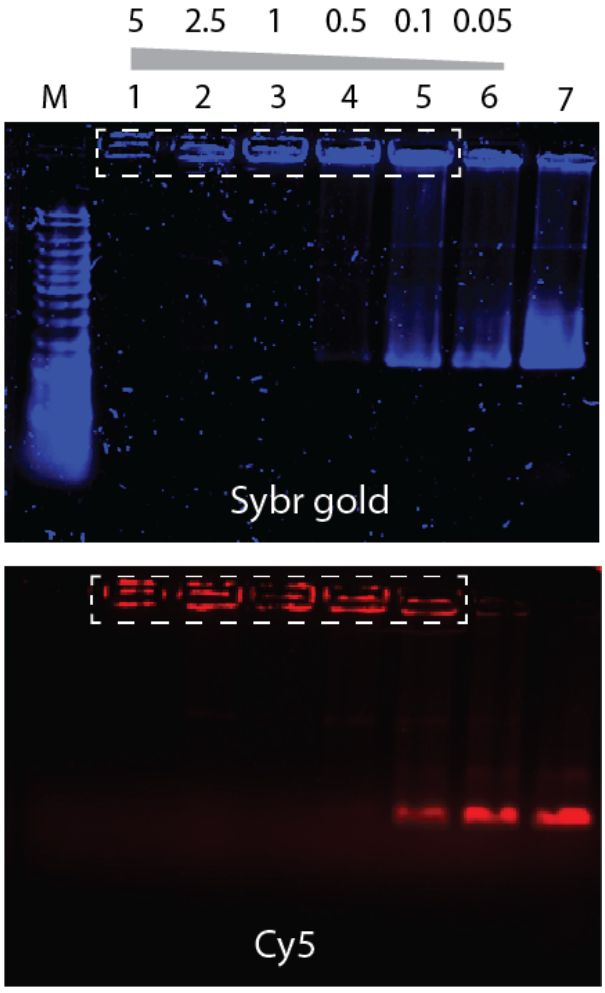

Figure 3.5: Gel electrophoresis reveals binding of BAU intercalator to DNA origami nanostructures. The origami nanoplates were labeled with Cy5 fluorophores (red) and incubated with different molar ratios of intercalator per DNA base pair, ranging from 5 to 0.05 in lanes 1 to 6, respectively. Note that Sybr-gold staining intensity is decreased in the presence of high amounts of BAU (lanes 1-2) and the electrophoretic mobility of the origami plates is significantly altered upon binding of the positively charged intercalator (lanes 1-4) as compared to the free origami control (lane 7). This is a 0.7% agarose gel run at 7 V/cm in TBE-Mg for 130 min at 4°C. M: GeneRuler DNA Ladder Mix (SM0333, ThermoFisher).

nia, USA) was employed in our aberration-corrected microscope. Figure 3.6a-b show the best micrographs that we could acquire under near-focus and strongly-defocused objective-lens settings, respectively. It is seen that the uranyl acetate-stained DNA structures are completely invisible at near focus (panel a), but they do appear very faintly under the strongly defocused illumination conditions (panel b). Only the origami main rectangle and occasionally the side arms (4 nm wide) are distinguishable, but the dsDNA loop at the bottom is not recognized at all. Note that the contrast in Figure 3.6a-b is very faint, because we do not perform negative staining, where the contrast is generated by a shadow image of the DNA in a uniform stain background. Rather, to investigate the "selectivity" of electron dyes, the contrast is generated by direct interaction of the compounds with DNA (i.e., positive staining). Note that, to investigate the visibility at the single molecule level, our origami contains only one layer of DNA, unlike multi-layer 3D DNA origami designs [18], and hence it yields very low electron scattering.

The poor visibility of the stained DNA origami structures in wide-field TEM imaging is explained by electron-optical reasons. For materials science specimens (mostly metals and ceramics), wide-field TEM at a focus close to zero is extensively used to resolve microscopic features with atomic resolution (even below 1 Angstrom resolution). However, in the case of biological samples, TEM imaging at near-focus conditions fails to provide enough contrast for visualization [19]. This is illustrated in Figure 3.6, where we calculate the contrast transfer function (CTF) of our aberration-corrected Titan microscope at near-focus and at strongly defocused imaging conditions, see panels (c) and (d), respectively. The CTF is a mathematical function which takes into account various imaging parameters such as the objective lens defocus, acceleration voltage, aberration coefficients, etc., and it plots the phase-to-amplitude conversion efficiency as a function of spatial frequencies of the electron wave (viz. the k vectors). For example, in the case of near-focus imaging (panel c), we observe no information transfer for the 2 nm fringe, which is the periodicity of the stacked DNA bundles within the origami rectangle, while the microscope can still resolve spatial features up to 2 Angstrom (the right end of curve with k=0.5 Å-1). All spatial frequencies in the green-highlighted area in Figure 3.6c will be absent in the final image. When the objective lens is strongly defocused up to 3000 nm (panel d), however, the 2 nm phase component is converted to amplitude with a better efficiency, though damped by the total spatial and temporal envelope. At this strong-defocus illumination, the CTF oscillates rapidly with its first zero shifting to lower spatial frequencies, which consequently results in a resolution loss (well below 5 Angstrom, i.e., more than a 50% drop in resolution compared to Figure 3.6c). We therefore conclude that wide-field TEM, is not a good approach to visualize DNA nanostructures with high contrast.

Unlike wide-field TEM, we find that the STEM technique is well-suited to probe the DNA-dye interactions. STEM is an imaging technique with a very different image-formation mechanism [20], which does not suffer from the CTF constraints. A main advantage of STEM over TEM for our purpose hinges on the fact that the obtained contrast is almost quadratically proportional to the atomic number (Z-contrast imaging) [20], and dyes containing elements with atomic number of 92 (uranyl acetate, BAU) or 78 (DP) thus generate a crisp contrast over the substrate with a low atomic number of 6 (carbon). Figure 3.7a-c summarizes our STEM results for the electron dyes that rendered

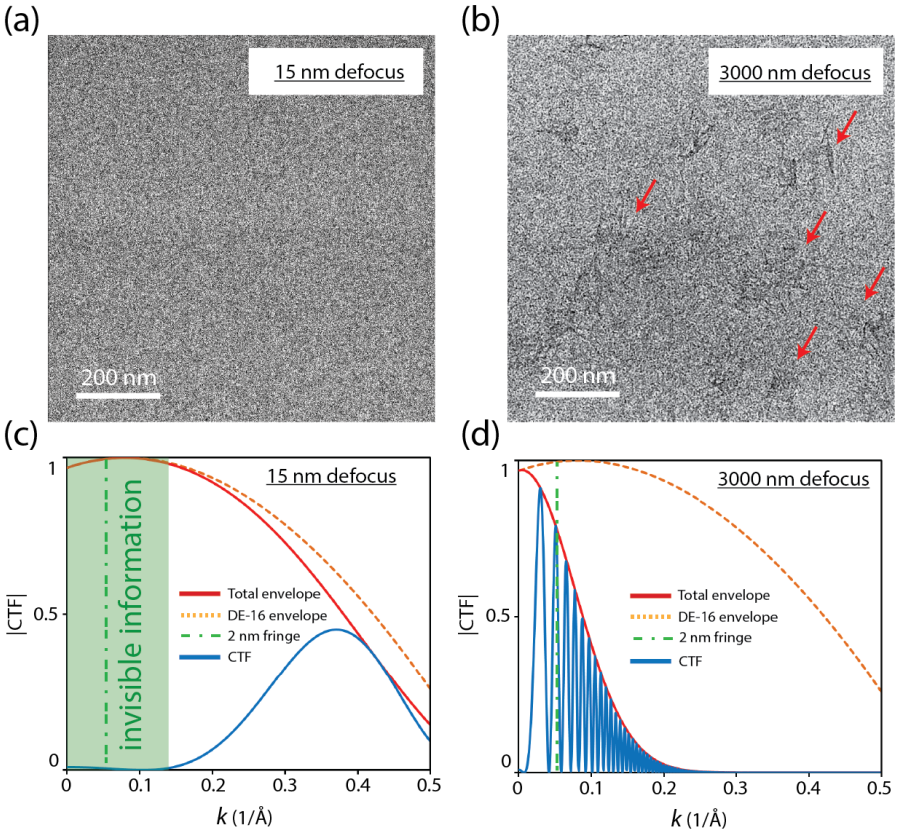

Figure 3.6: Conventional wide-field TEM suffers from poor contrast for imaging stained DNA-origami nanostructures. (a-b) Wide-field TEM images of DNA origami stained with uranyl acetate, taken by a DDD detector (DE-16) assisted by dose fractionation and drift correction. The origami plates are only partially visible in panel (b), but completely invisible at the near-focus condition in panel (a). Contrast transfer function (CTF) simulations for our aberration-corrected Titan microscope at different objective lens defocus values of 15 and 3000 nm, shown in (c) and (d), respectively. The simulation input values were set according to our microscope settings.

origami nanoplates visible. All images were taken under the same STEM acquisition parameters in the microscope and were treated with a similar despeckle noise reduction and contrast adjustment for better visibility.

Importantly, our new BAU dye is seen to yield good DNA contrast in STEM (Figure 3.7b). For BAU as well as for DP, we see contrast enhancement not only for the main origami rectangle (72 nm x 50 nm) but also for individual DNA strands (the floppy loop at the bottom that is only 2 nm (single DNA helix) wide as well as the side arms that are composed of 2 DNA helices, i.e., 4 nm wide). Such high-contrast single-shot STEM images of DNA supported on commercial carbon membranes indicate that STEM is a particularly fit technique for imaging stained DNA nanostructures. Excitingly, unlike staining protocols used for tissue sections, it is clear that no post-fixation is necessary for our DNA origami samples, which presents an important advantage for artefact-free imaging. To probe whether it is possible to increase the contrast even further, we stained the DNA nanoplates with high stain concentrations and increased the incubation times. We found that the contrast saturated at a certain concentration for each dye (see SI, Figure S3.7). The images in Figure 3.7 thus represent the highest contrast that could be achieved for each compound, likely representing the maximum number of dye molecules bound to the DNA strands.

We also investigated other staining agents reported in the literature, such as OsO4 and cisplatin, but we found no visibility in STEM imaging of DNA origami using these compounds. OsO4, with its high atomic number of 76 for osmium, plays a unique role in TEM imaging of biological samples [21], and it is often reported as a fixative agent for plastic-embedded tissue sections. Bahr reported that OsO4 does not react with nucleic acids [21], though no microscopic evidence was presented. To attempt to provide microscopic evidence for DNA binding, we stained our origami nanoplates with OsO4 and performed STEM imaging. We could however not detect any discernible contrast. Cisplatin, one of the most successful antitumor drugs, can potentially also be considered as an electron dye. It is well known that cisplatin binds quasi-covalently to DNA on the N^7 positions of the bases, which consequently causes double helix unwinding, kinking, and DNA cross-linking [2, 3, 22–24]. Despite this purported covalent affinity towards DNA, we were unable to visualize cisplatin-stained DNA origami with STEM. Some studies pointed out that cisplatin requires long incubation times to interacts with the DNA [3, 7, 23]. We therefore prolonged the incubation time of the cisplatin with DNA origami nanoplates on the TEM grid up to 2 days. After this long incubation period, we could observe large amounts of nanoparticles deposited on the TEM grids, but unfortunately still not any visible DNA origami (see SI, Figure S3.8). Our microscopic findings thus show that cisplatin and OsO4 are not suitable for in vitro staining studies of DNA.

We quantified the contrast of the stained DNA origami nanoplates. Different origami nanoplates were selected from random acquisitions at different locations on the TEM grids, and the HAADF detector signals were extracted along the origami main body (Figure 3.7d). SNR and contrast were computed according to SNR=(Is-In)/Stdn and contrast=(Is-In)/In, respectively, where Is denotes the average signal along the origami main rectangle, In the average background noise as measured along the carbon support, and Stdn the standard deviation of the background noise. Remarkably, Figure 3.7e-f shows that BAU with the bis-acridine intercalating ligand provides an excellent SNR and contrast,

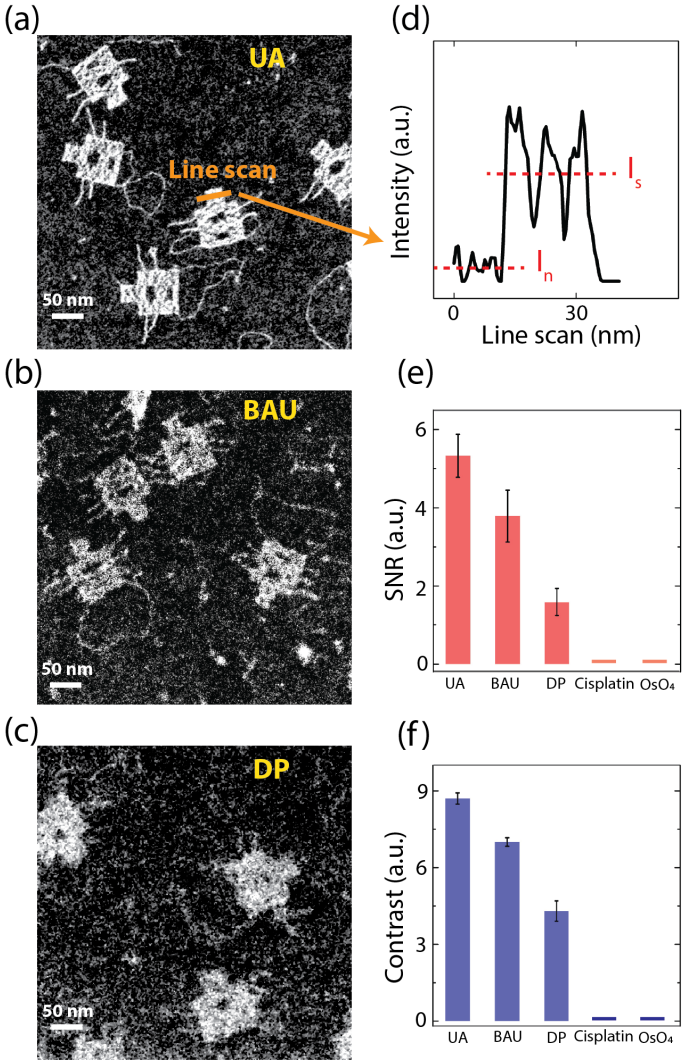

Figure 3.7: STEM imaging visualized stained-DNA nanostructures at the single-molecule level. (a-c) STEM images of DNA origami nanoplates stained with uranyl acetate (UA), BAU, and DP, respectively (see the experimental section for the dye concentrations). All images are single-frame acquisitions, without any class-averaging. (d) HAADF signal taken along the dashed line in panel (a). (e-f) Statistical analysis of the SNR and contrast obtained for each dye. The processed HAADF signals were extracted from different origami plates similar to an example shown in panel (d).

	Uranyl acetate	Bis-acridine uranyl	Dichloro platinum
binding mechanism	backbone	intercalation	intercalation (eventually covalent after ligand exchange)
association constant Ka(M^{-1})	8x10^6!	1.2x10^4	1.3x10^5-1.2x10^6*
number of bound dyes per base pair	1	0.25@ (ToTo bis-inercalator)	0.2*
atomic number (Z) of the core metal	92	92	78
Reference	! Ref [1]	@ Ref [25]	* Ref [26, 27]

Table 3.1: Biochemistry of DNA-dye interactions.

approaching the values of the uranyl acetate, but now as a positive-stain intercalator. The SNR and contrast values for BAU exceeds that of dichloro platinum with the terpyridine intercalating moiety (more than twice higher SNR, and 60% higher contrast). This indicates that our design strategy to consider bis-acridine ligand was indeed more effective than the intensively studied terpyridine conjugation. Note that, while the backbone binder uranyl acetate provides the highest contrast among the stains, we here aimed to synthesize and investigate intercalating electron dyes. When using the intercalating BAU and DP compounds, we always observed a higher noise (carbon appears to be brighter), which we could not avoid even by several washing steps. This may be due to some affinity of the intercalating ligands to the surface of the amorphous carbon. Nevertheless, single-DNA molecules are clearly visible over the background stained with BAU and DP intercalating dyes.

3.3. Discussion

We designed a new intercalating electron dye and presented single-molecule visualizations of DNA. In our experiments, Z-contrast STEM images were generated through direct interaction of these dyes with the DNA strands instead of conventional negative staining protocols where the contrast is rendered through a shadow image of DNA. Table 3.1 provides an overview for association constants, number of dye-molecules bound to each DNA base pair, and the electron-scattering capacity of the heavy metal center. Various of these attributes are important for rendering high contrast images, as discussed below.

First, we note that the common denominator between all these dyes is their high binding constants, in the range of 10^4-10^6 M^{-1}. This strong affinity is indispensable for visualization, rendering single-molecule DNA visible even after several washing steps during the sample preparation. Regarding the BAU, this strong binding affinity was verified by gel electrophoresis (Figure 3.5). The use of bis-acridine moiety in the BAU design

approach as the intercalating ligand was intentional with respect to a high binding constant, since it has been shown that bis-acridines have a substantially higher affinity to DNA than their corresponding mono-acridine analogues [15, 16]. Next to a high DNA affinity, another advantage of bis-acridine conjugation to the salophen ligand containing uranium, is that bis-acridine moieties are known to be biocompatible agents with excellent antitumor properties [15, 16].

Second, the dye density along the DNA helix should be maximized in order to obtain the highest scattering efficiency. Certainly, uranyl acetate provides the highest value of 1 dye bound per base pair compared to BAU and DP that perform a factor of 4 or 5 worse. Beer et al. showed that attachment of three heavy markers per base pair is required for one full amplitude contrast onto thin carbon membranes in wide-field TEM [28], whereas staining with uranyl acetate can yield only one heavy atom of uranium at maximum. This, together with phase contrast limitations imposed by CTFs shown in Figure 3.6c-d, explains the faint contrast that one obtains in normal wide-field TEM mode, where even utilization of a direct detection device is not helpful to boost the contrast (Figure 3.6a-b).

Finally, although on the basis of theoretical arguments, the STEM contrast is expected to scale as Z^2 versus atomic number, technically the current in the HAADF detector reaches a plateau, which consequently saturates the greyscale values in the STEM images and impedes to distinguish heavy elements from one another. For example, Ferrer et al. showed that the intensity difference between the Au (Z=79) and Pd (Z=46) columns in an Au/Pd nanoparticle is very small [29]. Accordingly, we expect that obtained STEM contrast for the dyes mentioned in Table 3.1 (with Z=92 for uranium and Z=78 for platinum) is likely not strongly dependent on the core heavy element. In other words, we estimate that the effects of binding constant and dye loading density are much more pronounced in determining the overall contrast in STEM than the atomic number of the core heavy metal. Note that this is only true for heavy elements, whereas Z-contrast imaging remains strongly beneficial when heavy atoms are supported onto light substrates such as carbon (Figure 3.7).

Maximizing the above-mentioned parameters provides a strategy for biochemists to further develop highly efficient electron dyes. Most importantly, the binding constant and dye loading density significantly contribute to contrast. We have shown the feasibility of bis-acridine conjugation to the salophen ring as one strategy for incorporating uranium (in bis-acridine uranyl). Also, the Pt(II) compounds containing terpyridine moieties (in dichloro platinum) are shown to be suitable candidates as intercalating electron dyes. The application of many Pt(II) or osmium complexes have been demonstrated for chromatin imaging. In fact, there are numerous papers presenting such chromatin data [4, 7, 30], but virtually none on in vitro imaging of single-molecule DNA through intercalation binding, which is the focus of our work. Based on our quantitative analyses in Figure 3.7e-f, such compounds perform worse than our bis-acridine design strategy for single-molecule visualization because our BAU compound has two DNA binding sites and a spatially distant heavy metal, which allows a tweezer-like binding to the DNA molecule. Tethering other intercalating ligands can be considered. The rich coordination chemistry of the transition metals together with the diverse conjugation possibilities to flat aromatic ligands are promising factors for the future synthesis of electron dyes. We

hope that our findings and methodology will spur the interests of the chemists to further develop highly-efficient intercalating electron dyes.

3.4. Conclusions

Summing up, we imaged single DNA molecules with high contrast using a newly designed intercalating molecule, and we compared the results to those for other electron dyes. By introducing DNA origami as a microscopy test object and using STEM over conventional wide-field TEM, we could characterize electron dyes that were appropriate for single-molecule DNA visualization. Imaging artefacts in hitherto investigations were eliminated, as a result of facile sample preparation and the absence of other biological molecules such as lipids and proteins. Our methodology is well-suited to investigate other newly synthesized electron dyes in the future. Looking forward, one intriguing application of intercalating electron dyes is in multi-color electron microscopy of biological systems. The first ever multicolor TEM images of such samples was shown by Adams et al. in 2016, who visualized different cellular components, very much similar to what multi-color fluorescence microscopy can offer, but with the full spatial resolution of TEM [31]. This is opening up new possibilities to push the resolution limits in life-science TEM, further expanding our understandings about the molecular processes of life.

3.5. Experimental Section

Staining compounds

The bis-acridine uranyl dye was synthetized as shown in Figure 3.1. To get an optimal linker length between the DNA intercalating ligand (i.e. the acridine moiety) and the TEM-contrast-enhancer scaffold (the uranyl unit), a commercially available 9-chloroacridine (1) was reacted with 6-aminohexan-1-ol (2) as described previously [32]. The isolated 9-hexylaminoacridine compound (3) was tosylated to afford (4), which was subsequently reacted with the selective allyl-protected 2-(2-Propenyloxy)-3-hydroxybenzaldehyde (5) to yield compound (6) having a benzaldehyde unit. The successful deprotection of (6) provided the free hydroxybenzaldehyde unit (7). The salophen base unit was synthesized by refluxing compound (7) with 1,2-benzenediamine (8) in methanol, followed by treating the mixture with uranyl acetate dihydrate to afford the uranyl-bis-acridine metallo-intercalator (9). For the complete synthesis, we refer to the SI. The stock concentration for staining experiments was 250 µM dissolved in DMSO. For staining compounds as reference measurements, we selected compounds with a known chemistry and specific DNA binding modes, while commercial drug cocktails of unknown type of interactions with DNA were neglected. For uranyl acetate, a solution of 2% uranyl acetate in Milli-Q water was used, which was filtered through a 0.2-µm PTFE membrane. Among the huge family of Pt(II) compounds, the rationale for choosing an appropriate molecule was having the simplest molecule with the presence of a common intercalating motif, namely the planar terpyridine subunit. Based on this, we selected dichloro platinum (Sigma Aldrich) [26, 27, 33], (10 mM in TE buffer).

Nuclear Magnetic Resonance Spectroscopy (NMR)
NMR (^1H- and ^{13}C) measurements were carried out using either a Bruker Avance III 400 spectrometer (^{1}H, 400 MHz; ^{13}C, 100 MHz) or a Bruker Avance 500 MHz spectrometer equipped with Ultrashield magnets (^{1}H, 500 MHz; ^{13}C, 125 MHz). The residual solvent signals were employed for shift correction (for ^{1}H-NMR spectra at 2.50, 4.87 and 7.26 ppm, for ^{13}C-NMR at 39.52, 49.00 and 77.16 ppm, respectively, for the following deuterated solvents CD3OD, DMSO-d6 and CDCl3). All NMR data were reported as follows: chemical shift, multiplicity (s = singlet, d = doublet, t = triplet, q =quartet), coupling constant (s) in Hertz (Hz) and integration. Multiplets (m) were reported over the range (ppm) where they appeared at the indicated field strength.

Mass Spectrometry (MS)
Fast atom bombardment (FAB) mass spectra and high-resolution mass spectra (HRMS) were measured with MAT95 of the Finnigan company. Electrospray ionization mass spectrometry (ESI-MS) data were recorded on a Q-Exactive (Orbitrap) mass spectrometer (Thermo Fisher Scientific, San Jose, CA, USA) equipped with an HESI II probe. The instrument was calibrated in the m/z range 74-1822 using premixed calibration solutions (Thermo Scientific). A constant spray voltage of 4.7 kV and a dimensionless sheath gas of 5 were applied. The capillary temperature and the S-lens RF level were set to 320 °C and 62.0 V, respectively. The samples were dissolved with a concentration of 0.05 mg·mL^{-1} in a mixture of THF:MeOH (3:2) containing 100 µmol of sodium trifluoroacetate (NaTFA) and infused with a flow of 5 mL·min^{-1}.

Association constant (ka) measurements of BAU
The quantification of the association constant of BAU toward dsDNA was performed by UV-VIS absorbance titration following two different procedures. In a first set of experiments, a freshly prepared solution of BAU (45 µM in 11.5% DMSO and 88.5% TEMg-buffer (20 mM Tris, 2 mM EDTA, 12.5mM MgCl2, pH 8)) was transferred into a quartz cuvette. Subsequently, small volumes (2-10 µl) of dsDNA solution of known concentration were subsequently added to the ligand solution and incubated for 5 minutes, followed by recording of the UV-Vis spectra. The dilution of the ligand was taken into account during the data analysis. In the second set of experiments, a freshly prepared solution of BAU (40 µM in 10% DMSO and 90% TEMg-buffer) was divided into different aliquots and individually mixed with a known amount of dsDNA and incubated for 5 minutes, followed by recording of the UV-Vis spectra. In each sample, the volume was maintained constant (280 µl). All UV-VIS absorbance spectra were recorded by means of Cary Series UV-Vis Spectrophotometer, Agilent Technologies. For these experiments, a 5438 bp bacterial plasmid (109Z5 [34]) was used as dsDNA. The concentration of dsDNA stock solution (expressed as base-pair concentration) was determined by UV-VIS measurements in TE buffer (20 mM Tris, 2 mM EDTA pH 8). The affinity constants were determined from changes in the absorbance, according to a reported equation [35], which was derived from the previously reported neighbor-exclusion model [36].

DNA Origami as a calibration tool for TEM imaging
We designed a two-dimensional DNA origami nanoplate as a test object for the scattering contrast of dsDNA (Figure 3.2). Our origami structure contains various DNA features

of interests such as side arms (4 nm wide, 27 and 43 nm long), two cavities in the middle (4 and 8 nm wide, 19 nm long), and a (flexible) individual dsDNA (2 nm wide) molecule loop at the bottom. Incorporation of these features into the design makes it convenient to evaluate if various contrast agents can visualize individual DNA molecules as well as more extended DNA structures. For details of the origami design and its characterization, we refer to our previous work [37].

TEM sample preparation

Commercial carbon-coated TEM grids (nominal 3-4 nm thin carbon supported by a 5-6 nm formvar layer, Electron Microscopy Science, USA) were used for supporting the origami nanoplates. 4 µl of the origami solution (at a concentration of 5 nM) was applied to freshly glow-discharged TEM grids and incubated for 2 minutes. Grids were washed with ultra-clean Milli-Q water to remove unadhered origami plates. Next, without drying the sample, the staining compound was pipetted onto the TEM grids and left to react for 1 minute. Finally, the grids were thoroughly washed to remove all the chemicals from the carbon surface. Removing the residual stain at the last step is a key point to avoid generation of contrast by the common negative staining protocols (where the thickness variation of the stain layer across the biomolecule creates detectable mass-thickness contrast). In the current work, the observed contrast is instead the consequence of direct physiochemical interaction of the staining chemicals with the DNA. Following the above TEM preparation protocol, we obtained uniform distributions of origami nanoplates with a high density onto the TEM grids, which allowed facile investigation of the staining compounds, a clear advantage over the tedious sample preparation protocols for tissue sections or other DNA-containing biological samples.

TEM imaging

For S/TEM imaging, we used a FEI Titan microscope equipped with a post-specimen aberration corrector operating at 300 kV acceleration voltage. Imaging at 300 kV was preferred over 80 kV for lower ionization damage to DNA. A high-angle annular dark-field (HAADF) detector (Fischione, USA) at camera length of 28.3 cm was used for obtaining mass-thickness-dominated contrast (Z-contrast). For quantitative comparison, all STEM images were acquired with the same imaging parameters (convergence angle, dwell time, pixel size) and post-processing for contrast evaluation. In TEM mode, the third-order spherical aberration (C3) coefficient was set to zero in the image corrector to minimize the information delocalization.

3.6. Supporting Information

3.6.1. Synthesis of bis-acridine-uranyl (BAU) metallo-intercalator, and NMR spectra of intermediate compounds

Uranyl metallo-intercalator based on the Salophen base unit was synthesized by starting with commercially available 9-chloroacridine. In the first step, a spacer chain was attached by treating 9-chloroacridine (1) with 6-aminohexan-1-ol (2) followed by tosylation to get the tosylated product (4). Selective allyl protected 2-(2-Propenyloxy)-3-hydroxybenzaldehyde (5), obtained according to the literature [38], was refluxed with tosyl derivative (4) to afford compound 6 having benzaldehyde attached with an acridine unit through spacer chain, which on deprotection gave the free hydroxybenzaldehyde unit (7). The salophen base unit was synthesized by refluxing compound 7 with 1,2-benzenediamine (8) in methanol followed by treating the mixture with uranyl acetate dihydrate to afford uranyl-bis-acridine metallo-intercalator (9).

6-(acridin-9-ylamino)hexan-1-ol (compound 3)
A mixture of 9-chloroacridine (1) (3.12 g, 14.6 mmol, 1.0 eq) and 6-aminohexan-1-ol (2) (1.71 g, 14.6 mmol, 1.0 eq) was added to phenol (20 g, at 80 °C), and the resulting mixture was heated for 2 h at 100 °C. The reaction mixture was cooled to room temperature, and the solvent was removed under reduced pressure at 70 °C. The brown residue was refluxed with ethanol and further treated with minute amounts of diethylether to afford crude product 3 (93 %, 4 g, 13.6 mmol) as a yellow solid.

^{1}H NMR (500 MHz, CD3OD): δ (ppm) 1.36-140 (m, 2H), 1.49-1.61 (m, 6H), 3.22 (t,J = 7.2Hz, 2H), 4.11 (J = 7.7, 2H), 7.48-7.55 (m, 2H), 7.79 (d, J = 8.6Hz, 2H), 7.88-7.99 (m, 2H), 8.04, s, 1H), 8.45 (d, J = 8.6 Hz, 2H).

^{13}C NMR (125 MHz, CD3OD): δ (ppm) 26.2, 28.9, 29.2, 32.1, 49.1, 61.4, 118.2, 123.5, 125.2, 127.7, 130.9, 134.9, 135.5, 162.3.

HRMS-FAB: theoretical C19H23N2O [M+H] + 295.1859, experimental 295.1856

6-(acridin-9-yl-amino)hexyl-4-methylbenzenesulfonate (compound 4)
Triethylamine (1.13 mL, 8.10 mmol, 1.3 eq) was added to a mixture of 6-(acridin-9-ylamino)hexan-1-ol (3) (1.83 g, 6.23mmol, 1 eq) in anhydrous dichloromethane (20 mL) under inert atmosphere. The mixture was stirred for 1 hour at ambient temperature. The solution of p-toluenesulfonyl chloride (1.43 g, 7.48mmol, 1.2 eq) in 10 mL of anhydrous dichloromethane) was then added in a dropwise manner to the reaction mixture at 0 °C. The reaction mixture was stirred overnight at ambient temperature; subsequently dichloromethane (100 mL) was added to quench the reaction. The organic phase was washed with water (3 x 100 mL and brine (1 x 100 mL), and afterwards dried over anhydrous MgSO4. The solvent was then removed under reduced pressure to afford the crude tosylated product 4 (97 %, 2.71 g, 6.04mmol) as a yellow solid.

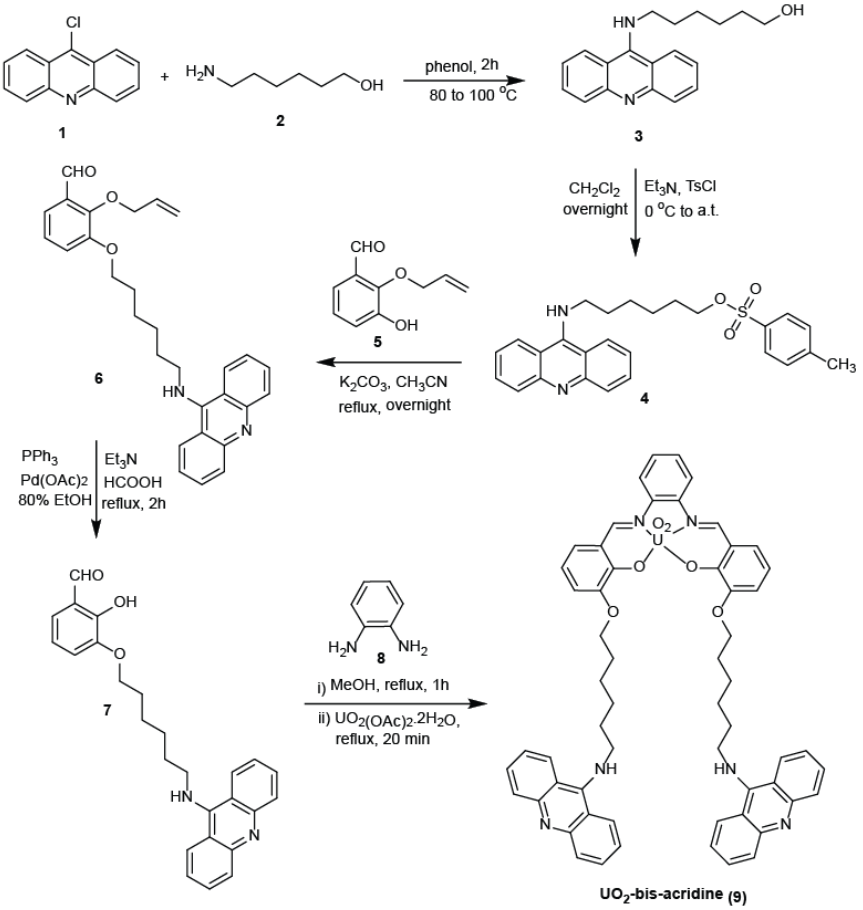

Figure S3.1: Synthesis of uranyl-bis-acridine metallo-intercalator (9)

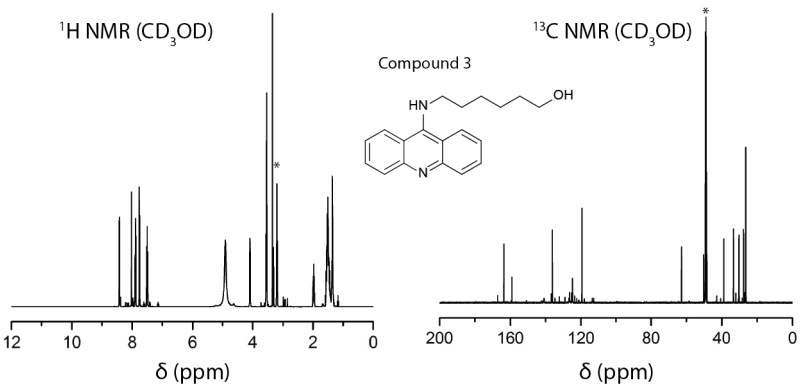

Figure S3.2: ^{1}H (500 MHz, CD3OD) and ^{13}C (125 MHz, CD3OD) NMR spectra of compound 3

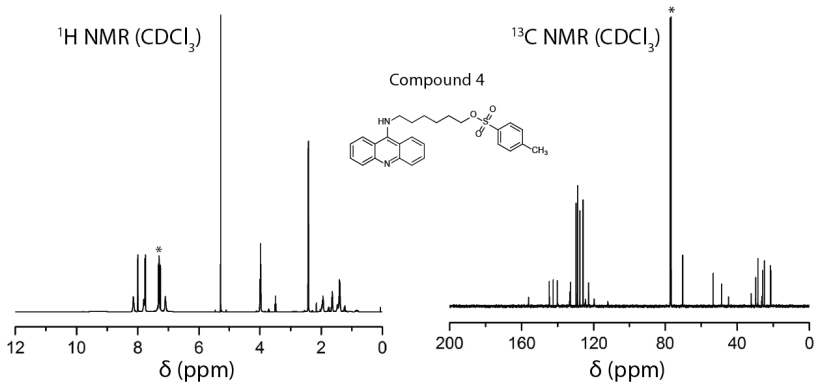

Figure S3.3: ^{1}H (500 MHz, CDCl3) and ^{13}C (125 MHz, CDCl3) NMR spectra of compound 4

^{1}H NMR (500 MHz, CDCl3): δ (ppm) 1.34-147 (m, 4H), 1.55-1.72(m, 2H), 1.91-2.02 (m, 2H), 2.45 (s, 3H), 3.99-4.09 (m, 4H), 7.06-7.12 (m, 2H), 7.31-7.35 (m, 4H), 7.77 (d, J = 8.2 Hz, 2H), 8.02 (d, J = 8.2 Hz, 2H), 8.17 (d, J = 8.6 Hz, 2H).

^{13}C NMR (125 MHz, CDCl3): δ (ppm) 21.6, 25.0, 26.2, 28.6, 29.9, 53.4, 70.4, 119.9, 122.9, 124.8, 126.0, 127.8, 129.0, 129.8, 133.0, 133.5, 140.3, 142.6, 144.7, 156.2

HRMS-FAB: theoretical C26H29N2O3S [M+H] + 449.1730 experimental 449.1739

2-(2-Propenyloxy)-3-hydroxybenzaldehyde (compound 5)
Selective protection of 2,3-dihydroxybenzaldehyde was done according to the literature procedure [38]. Sodium hydride (1.15 g, 0.038 mol, 1.05 eq), which was washed with petroleum ether 40-60 °C before use, was added to the mixture of 2,3-dihydroxybenzaldehyde (5.0 g, 0.036 mol, 1.0 eq) in DMSO (65 mL). After the mixture was stirred at ambient temperature for 2 h, 3-bromo-1-propene (4.5 g, 0.038 mol, 1.05 eq) was added in a dropwise fashion. Subsequently, the reaction mixture was stirred at ambient temperature for 24 h. The product was poured into water (200 mL) and extracted with chloroform (3 x 150 mL). The combined organic phase was washed with distilled water (3 x 150 mL), dried over MgSO4 and concentrated under reduced pressure. The residue was purified by silica gel column chromatography (chloroform was used as eluent), followed by recrystallization (petroleum ether 40-60 °C /ether 95/5) to afford pure the product 5 (65 %, 4.20 g, 0.024 mol) as white needles.

^{1}H NMR (500 MHz, CDCl3): δ (ppm) 4.58-4.62 (m, 2H), 5.34-5.46 (m, 2H), 5.98 (bs, 1H), 6.07-6.17 (m, 1H), 7.13-7.23 (m, 2H), 7.39 (dd, J = 7.7 Hz and 1.7 Hz, 1H), 10.28 (s, 1H).

^{13}C NMR (125 MHz, CDCl3): δ (ppm) 77.3, 120.1, 121.5, 121.8, 125.1, 129.3, 132.4, 147.8, 149.7, 189.8.

HRMS-FAB: theoretical C10H11O3 [M+H] + 179.1625, experimental 179.1621

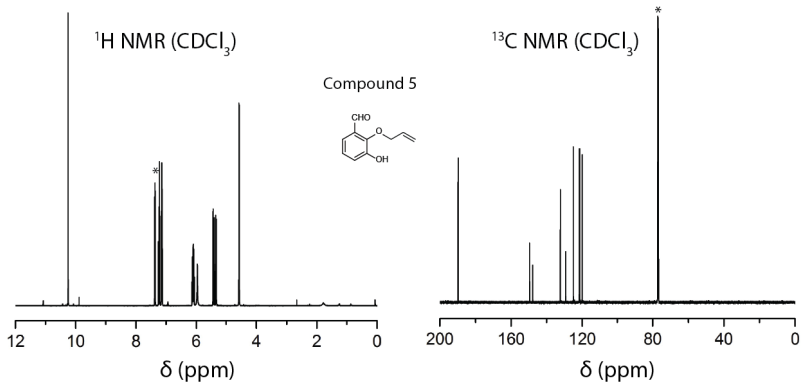

Figure S3.4: ^{1}H (500 MHz, CDCl3) and ^{13}C (125 MHz, CDCl3) of compound 5

3-((6-(acridin-9-ylamino)hexyl)oxy)-2-(allyloxy)benzaldehyde (compound 6)
To a suspension of 6-(acridin-9-ylamino)hexyl-4-methylbenzenesulfonate (4) (2.71 g, 6.04 mmol, 1.0 eq) and 2-(2-Propenyloxy)-3-hydroxybenzaldehyde (5) (1.07 g, 6.00 mmol, 1.0 eq) in anhydrous acetonitrile (200 mL), potassium carbonate (2.60 g, 18.7 mmol, 3.12 eq) was added under inert atmosphere. Subsequently, the reaction mixture was refluxed overnight. After cooling to ambient temperature, the potassium carbonate was filtered off and the solvent was evaporated under reduced pressure. The obtained residue was dissolved in dichloromethane (300 mL) and washed with distilled water (2 x 200 mL and brine (1 x 200 mL). The organic phase was dried over anhydrous MgSO4, filtered and evaporated under reduced pressure to afford the crude product. A silica gel column chromatography (solid deposit) eluted with dichloromethane/methanol (9:1 => 8:2, Rf(DCM MeOH:8/2) = 0,24) gave pure product 6 (34 %, 0.91 g, 2.01 mmol) as a yellow solid.

^{1}H NMR (500 MHz, CDCl3): δ (ppm) 1.48-153 (m, 4H), 1.75-1.81(m, 2H), 1.93-199 (m, 2H), 3.91 (t, J = 6.3 Hz, 2H), 3.99 (t, J = 7.3Hz, 2H), 4.53 (d, J = 6.1 Hz, 2H), 5.10-5.13 (m, 1H), 5.21-5.26 (m, 1H), 5.89-5.95 (m, 1H), 6.96-7.03 (m, 2H), 7.13-7.18 (m, 2H), 7.31 (dd, J = 7.2 Hz and 2.4 Hz, 1H), 7.42 (t, J = 7.7 Hz, 2H), 7.93-8.01 (m, 2H), 8.30 (d, J = 8.6 Hz, 2H), 9.36 (bs, 1H), 10.32 (s, 1H).

^{13}C NMR (125 MHz, CDCl3): δ (ppm) 25.7, 26.5, 29.0, 30.1, 49.0, 112.9, 118.7, 118.8, 119.0, 120.8, 123.0, 124.1, 124.9, 125.9, 128.9, 130.0, 133.1, 133.3, 141.3, 151.2, 152.3, 156.0, 190.4.

HRMS-FAB: theoretical C29H31N2O3 [M+H] + 455-2117, experimental 455.2115

3-((6-(acridin-9-ylamino)hexyl)oxy)-2-hydroxybenzaldehyde (compound 7)
A mixture of 3-((6-(acridin-9-ylamino)hexyl)oxy)-2-(allyloxy)benzaldehyde (6) (0.91 g,2.01 mmol, 1.0 eq), Pd(OAC)2 (4.5 mg, 0.02 mmol, 0.01 eq) and PPh3 (21 mg, 0.08 mmol, 0.04 eq) in 80% ethanol (10 mL) was stirred at ambient temperature for 10 minutes. Triethylamine (0.335 mL, 2.4 mmol, 1.2 eq) and formic acid (0.226 mL, 6.0 mmol, 3.0 eq) was

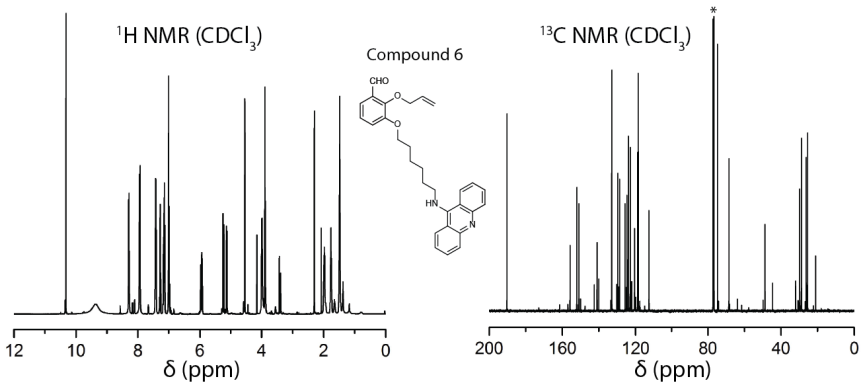

Figure S3.5: ^{1}H (500 MHz, CDCl3) and ^{13}C (125 MHz, CDCl3) NMR spectra of compound 6

added, and the reaction mixture was refluxed for additional 2 h. The solvent was evaporated under reduced pressure and the residue was dissolved in dichloromethane (40 mL). The organic phase was washed, respectively, with distilled water (2 x 25 mL) and brine (25 mL). The organic solvent was removed by rotary evaporator to afford a brown oil which was further purified by silica gel column chromatography (via solid deposition) using chloroform/methanol as eluent (98:2 => 95:5 => 9:1 => 8:2, Rf(CHCl3/MeOH:9/1) = 0,25) to afford pure product 7 (62 %, 514 mg, 1.24 mmol) as an orange solid.

^{1}H NMR (500 MHz, CDCl3): δ (ppm) 1.47-163 (m, 4H), 1.73-1.85 (m, 2H), 1.99-2.03 (m, 2H), 3.99 (t, J = 6.3 Hz, 2H), 4.07 (t, J = 7.3 Hz, 2H), 6.90 (t, J = 7.9 Hz, 1H), 7.05 (d, J = 7.3 Hz, 1H), 7.14-7.19 (m, 3H), 7.35-7.45 (m, 2H), 7.68-7.74 (m, 1H), 7.96-8.04 (m, 2H), 8.31-8.41 (m, 1H), 9.81 (bs, 1H), 9.89(s, 1H), 13.44 (bs, 1H).

^{13}C NMR (125 MHz, CDCl3): δ (ppm) 25.1, 26.2, 28.7, 29.9, 48.5, 69.1, 119.2, 119.5, 20.9, 123.0, 124.5, 126.0, 128.0, 128.9, 130.5, 133.9, 135.5, 140.2, 147.5, 151.8, 156.8, 196.4

HRMS-FAB: theoretical C26H27N2O3 [M+H] + 415.2193, experimental 415.2191.

Synthesis of UO2-bis-acridine (BAU)

Uranyl-bis-acridine (9) was synthesized following la previously reported procedure [39]. IMPORTANT: Care should be taken while handing uranyl compound because of its toxicity and residual radioactivity. In a refluxing solution of 3-((6-(acridin-9-ylamino)hexyl)oxy)-2-hydroxybenzaldehyde (7) (439 mg, 1.06 mmol, 1.0 eq) in methanol (20 mL) was added a solution of 1,2-benzenediamine (8) (57.3 mg, 0.529 mmol, 0.5 eq) in methanol (5 mL) in a dropwise manner under inert atmosphere. After 1 h, uranyl acetate dihydrate (UO2(OAc)2.2H2O) (225.13 mg, 0.529 mmol, 0.5 eq) was added, and the reaction mixture was refluxed for additional 20 min. After cooling to ambient temperature, the precipitate was filtered off and further washed with cold methanol to give UO2-bis-acridine (9) (29 %, 179 mg, 0.153 mmol) as an orange solid.

^{1}H NMR (500 MHz, DMSO-d6): δ (ppm) 1.42-1.52 (m, 4H), 1.54-1.61 (m, 4H), 1.81-1.92 (m, 8H), 3.89-4.01 (m, 4H), 4.15-4.21 (m, 4H), 6.56-6.67 (m, 2H), 7.12 (d, J = 8.1 Hz,

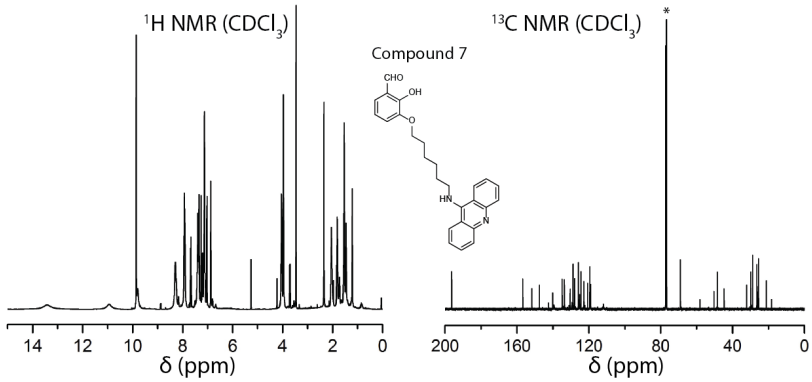

Figure S3.6: ^{1}H (500 MHz, CDCl3) and ^{13}C (125 MHz, CDCl3) NMR spectra of compound 7

1H), 7.18-7.21 (m, 1H), 7.33-7.43 (m, 6H), 7.47 (d, J = 8.1 Hz, 1H), 7.51-7.57 (m, 2H), 7.69-7.81 (m, 9H), 8.33-8.48 (m, 4H), 9.61 (s, 2H).

^{13}C NMR (125 MHz, DMSO-d6): δ (ppm) 25.8, 26.7, 28.4, 30.8, 55.3, 69.1, 116.4, 118.6, 120.7, 122.7, 124.8, 128.6, 129.1, 134.9, 138.0, 141.4, 147.2, 159.6, 156.1, 159.5, 159.8, 161.6, 167.0.

HRMS-FAB: theoretical C58H55N6O6 [M+H] + 1169.3916, experimental 1169.3914.
ESI-MS: theoretical: 1169.4685, experimental m/z 1169.4689.

3.6.2. Cross-linking of DNA origami via BAU tethering

Microscopic investigations of the complexes in lanes 1-4 of Figure 3.5 (main text) indicated DNA origami interaction due BAU-induced tethering (Figure S3.7). To understand the chemical composition of the observed aggregates, we performed energy dispersive X-ray spectroscopy (EDS). EDS analysis was carried out in STEM mode for higher spatial resolution, and using a double-tilt holder with a Beryllium specimen cradle for enabling higher signal sensitivity. For better light element detection, a recent windowless detector (X-MaxN 100TLE, Oxford instruments, UK) was employed. The presence of uranium and oxygen is indicative of DNA-bound BAU molecules, and the phosphor signal stems from the DNA backbone. The experimental parameters for EDS acquisitions were optimized for minimum electron beam damage to DNA.

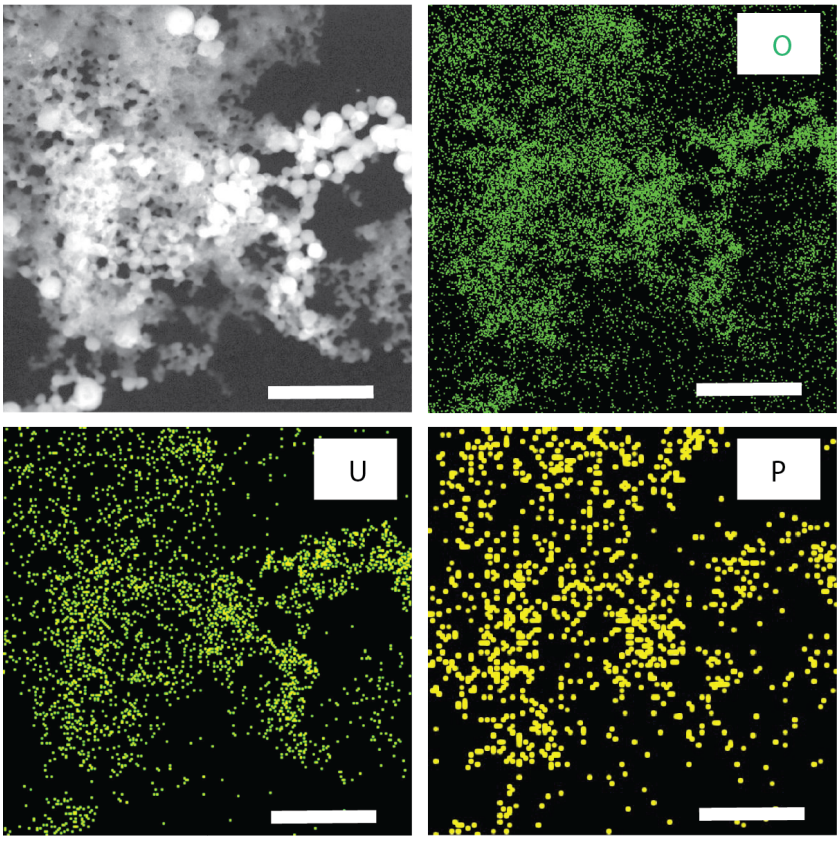

Figure S3.7: STEM imaging and EDS analysis indicates BAU-induced DNA origami cross-linking. Scale bar is 500 nm.

3.6.3. The effects of dye concentration and incubation time on the contrast of the stained DNA origami nanoplates

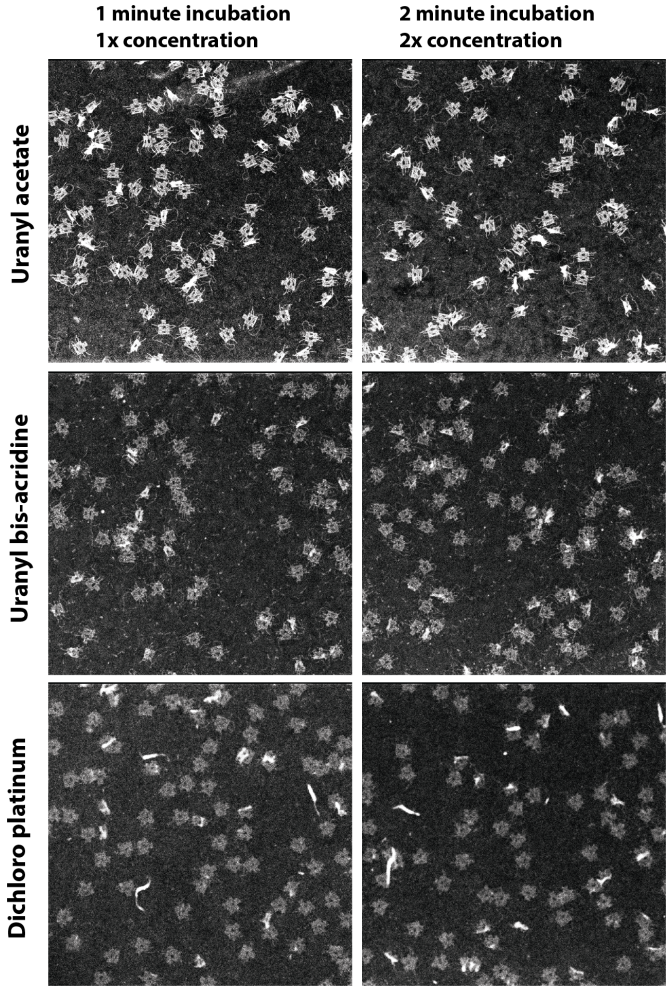

Figure S3.8: Contrast of the stained DNA origami saturates after 1 minute incubation time at 1x stock concentration of the electron dyes. Due to high binding affinity of the dyes, they react immediately with DNA (below 1 minute), after which the STEM contrast could not be increased anymore. The stock concentration (1x) for each dye is given in the experimental section.

3.6.4. Nanoparticle deposition onto TEM grids after incubation with cisplatin

After long incubation of 2 days with cisplatin, we observed very pronounced nanoparticle precipitation onto the TEM grids (panels a-b of Figure S3.9), where the clusters exhibited a dominant Cu/Pt signal in EDS elemental mapping (panels c-f, see also Table S3.1 for quantitative composition analysis of the red dashed squares 1 and 2 in Figure S3.9b). Note that spurious X-rays caused by the stray electrons lead to uncertainty in distinguishing the Cu and Pt from one another. We could not detect any DNA origami nanoplates in the areas where Pt nanoparticles were absent, such as the marked region 2 in panel (b).

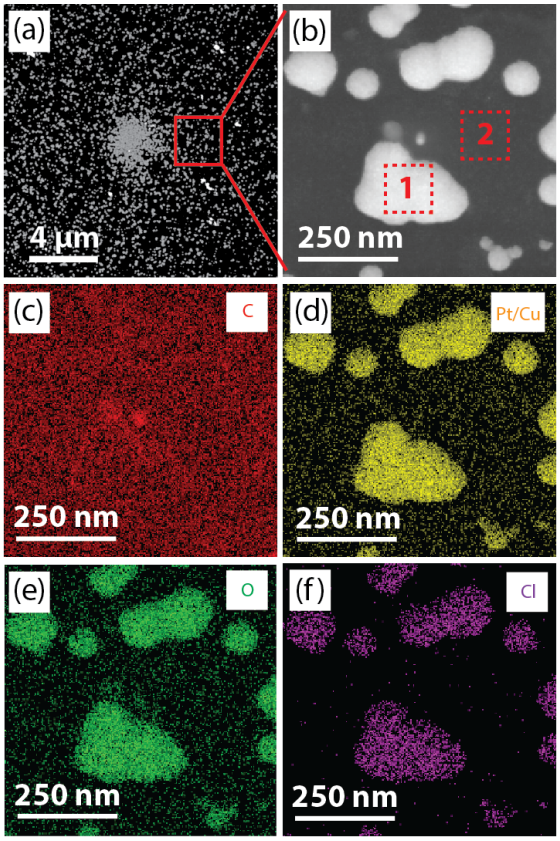

Figure S3.9: STEM imaging and EDS analysis demonstrate nanoparticle deposition onto TEM grids after in vitro staining of the DNA origami samples with cisplatin.

Spectrum	C	Cu/Pt	O	Si	Cl	Other
1	23.1	40.8	25.9	1.1	6.2	2.9
2	81.3	7.6	6.5	4.6	-	-

Table S3.1: EDS chemical analysis of marked regions 1 and 2 in Figure S3.9b.

References

[1] C. R. Zobel and M. Beer, *Electron stains: I. chemical studies on the interaction of dna with uranyl salts,* The Journal of Cell Biology **10**, 335 (1961).

[2] B. J. Pages, D. L. Ang, E. P. Wright, and J. R. Aldrich-Wright, *Metal complex interactions with dna,* Dalton transactions **44**, 3505 (2015).

[3] D. Wang and S. J. Lippard, *Cellular processing of platinum anticancer drugs,* Nature reviews Drug discovery **4**, 307 (2005).

[4] V. M. Manikandamathavan, N. Duraipandy, M. S. Kiran, V. G. Vaidyanathan, and B. U. Nair, *A new platinum (ii) complex for bioimaging applications,* RSC Advances **5**, 24877 (2015).

[5] R. N. Bose, L. Maurmann, R. J. Mishur, L. Yasui, S. Gupta, W. S. Grayburn, H. Hofstetter, and T. Salley, *Non-dna-binding platinum anticancer agents: Cytotoxic activities of platinum–phosphato complexes towards human ovarian cancer cells,* Proceedings of the National Academy of Sciences **105**, 18314 (2008).

[6] K. Suntharalingam, O. Mendoza, A. A. Duarte, D. J. Mann, and R. Vilar, *A platinum complex that binds non-covalently to dna and induces cell death via a different mechanism than cisplatin,* Metallomics **5**, 514 (2013).

[7] S. Inaga, T. Katsumoto, K. Tanaka, T. Kameie, H. Nakane, and T. Naguro, *Platinum blue as an alternative to uranyl acetate for staining in transmission electron microscopy,* Archives of histology and cytology **70**, 43 (2007).

[8] J. A. Terzakis, *Uranyl acetate, a stain and a fixative.*, Tech. Rep. (Francis Delafield Hospital, New York, 1968).

[9] M. H. Bernstein, *Iron as a stain for nucleic acids in electron microscopy,* The Journal of biophysical and biochemical cytology **2**, 633 (1956).

[10] M. Nakakoshi, H. Nishioka, and E. Katayama, *New versatile staining reagents for biological transmission electron microscopy that substitute for uranyl acetate,* Journal of electron microscopy **60**, 401 (2011).

[11] P. W. Rothemund, *Folding dna to create nanoscale shapes and patterns,* Nature **440**, 297 (2006).

[12] B. Neto and A. Lapis, *Recent developments in the chemistry of deoxyribonucleic acid (dna) intercalators: principles, design, synthesis, applications and trends,* Molecules **14**, 1725 (2009).

[13] J. Brglez, P. Nikolov, A. Angelin, and C. M. Niemeyer, *Designed intercalators for modification of dna origami surface properties,* Chemistry–A European Journal **21**, 9440 (2015).

[14] F. Sabaté, R. Gavara, I. Giannicchi, R. Bosque, A. Dalla Cort, and L. Rodríguez, *Ternary assemblies comprising metal–salophen complexes and 4, 4-bipyridine,* New Journal of Chemistry **40**, 5714 (2016).

[15] S. M. Sondhi, S. Kumar, R. Rani, A. Chakraborty, and P. Roy, *Synthesis of bis-acridine derivatives exhibiting anticancer and anti-inflammatory activity,* Journal of Heterocyclic Chemistry **50**, 252 (2013).

[16] I. Antonini, P. Polucci, A. Magnano, B. Gatto, M. Palumbo, E. Menta, N. Pescalli, and S. Martelli, *Design, synthesis, and biological properties of new bis (acridine-4-carboxamides) as anticancer agents,* Journal of medicinal chemistry **46**, 3109 (2003).

[17] L. Jin, A.-C. Milazzo, S. Kleinfelder, S. Li, P. Leblanc, F. Duttweiler, J. C. Bouwer, S. T. Peltier, M. H. Ellisman, and N.-H. Xuong, *Applications of direct detection device in transmission electron microscopy,* Journal of structural biology **161**, 352 (2008).

[18] E. Stahl, T. G. Martin, F. Praetorius, and H. Dietz, *Facile and scalable preparation of pure and dense dna origami solutions,* Angewandte Chemie International Edition **53**, 12735 (2014).

[19] K. Nagayama and R. Danev, *Phase contrast electron microscopy: development of thin-film phase plates and biological applications,* Philosophical Transactions of the Royal Society B: Biological Sciences **363**, 2153 (2008).

[20] R. Erni, *Aberration-corrected imaging in transmission electron microscopy: an introduction* (World Scientific Publishing Company, 2010).

[21] G. Bahr, *Osmium tetroxide and ruthenium tetroxide and their reactions with biologically important substances: electron stains iii,* Experimental cell research **7**, 457 (1954).

[22] B. Lippert, *From cisplatin to artificial nucleases—the role of metal ion-nucleic acid interactions in biology,* Biometals **5**, 195 (1992).

[23] G. B. Onoa, G. Cervantes, V. Moreno, and M. J. Prieto, *Study of the interaction of dna with cisplatin and other pd (ii) and pt (ii) complexes by atomic force microscopy,* Nucleic acids research **26**, 1473 (1998).

[24] R. Krautbauer, H. Clausen-Schaumann, and H. E. Gaub, *Cisplatin changes the mechanics of single dna molecules,* Angewandte Chemie International Edition **39**, 3912 (2000).

[25] H. P. Spielmann, D. E. Wemmer, and J. P. Jacobsen, *Solution structure of a dna complex with the fluorescent bis-intercalator toto determined by nmr spectroscopy,* Biochemistry **34**, 8542 (1995).

[26] K. Jennette, S. Lippard, G. Vassiliades, and W. Bauer, *Metallointercalation reagents. 2-hydroxyethanethiolato (2, 2, 2 -terpyridine)-platinum (ii) monocation binds strongly to dna by intercalation,* Proceedings of the National Academy of Sciences **71**, 3839 (1974).

[27] M. Howe-Grant, K. C. Wu, W. R. Bauer, and S. J. Lippard, *Binding of platinum and palladium metallointercalation reagents and antitumor drugs to closed and open dnas,* Biochemistry **15**, 4339 (1976).

[28] M. Beer and E. N. Moudrianakis, *Determination of base sequence in nucleic acids with the electron microscope: Visibility of a marker,* Proceedings of the National Academy of Sciences of the United States of America **48**, 409 (1962).

[29] D. Ferrer, D. A. Blom, L. F. Allard, S. Mejía, E. Pérez-Tijerina, and M. José-Yacamán, *Atomic structure of three-layer au/pd nanoparticles revealed by aberration-corrected scanning transmission electron microscopy,* Journal of Materials Chemistry **18**, 2442 (2008).

[30] A. Wragg, M. R. Gill, C. J. Hill, X. Su, A. J. Meijer, C. Smythe, and J. A. Thomas, *Dinuclear osmium (ii) probes for high-resolution visualisation of cellular dna structure using electron microscopy,* Chemical Communications **50**, 14494 (2014).

[31] S. R. Adams, M. R. Mackey, R. Ramachandra, S. F. P. Lemieux, P. Steinbach, E. A. Bushong, M. T. Butko, B. N. Giepmans, M. H. Ellisman, and R. Y. Tsien, *Multicolor electron microscopy for simultaneous visualization of multiple molecular species,* Cell chemical biology **23**, 1417 (2016).

[32] P. Nielsen, J. Hansen, T. Thomsen, and O. Buchardt, *Reagents for photoaffinity labeling. i. photobinding efficiency of aryl azido-, diazocyclopentadienyl-and ethyl diazomalonyl-derivatives of 9-aminoacridine,* Experientia **39**, 1063 (1983).

[33] G. W. Watt and J. E. Cuddeback, *The synthesis of mixed ligand complexes of platinum (ii),* Journal of Inorganic and Nuclear Chemistry **33**, 259 (1971).

[34] M. Erkelenz, D. M. Bauer, R. Meyer, C. Gatsogiannis, S. Raunser, B. Saccà, and C. M. Niemeyer, *A facile method for preparation of tailored scaffolds for dna-origami,* Small **10**, 73 (2014).

[35] L. Z. Zhang and G.-Q. Tang, *The binding properties of photosensitizer methylene blue to herring sperm dna: a spectroscopic study,* Journal of Photochemistry and Photobiology B: Biology **74**, 119 (2004).

[36] J. D. McGhee and P. H. von Hippel, *Theoretical aspects of dna-protein interactions: co-operative and non-co-operative binding of large ligands to a one-dimensional homogeneous lattice,* Journal of molecular biology **86**, 469 (1974).

[37] Y. Kabiri, A. N. Ananth, J. van der Torre, A. Katan, J.-Y. Hong, S. Malladi, J. Kong, H. Zandbergen, and C. Dekker, *Distortion of dna origami on graphene imaged with advanced tem techniques,* small **13**, 1700876 (2017).

[38] C. J. Van Staveren, J. Van Eerden, F. C. Van Veggel, S. Harkema, and D. N. Reinhoudt, *Cocomplexation of neutral guests and electrophilic metal cations in synthetic macrocyclic hosts,* Journal of the American Chemical Society **110**, 4994 (1988).

[39] D. M. Rudkevich, Z. Brzozka, M. Palys, H. C. Visser, W. Verboom, and D. N. Reinhoudt, *Ein difunktioneller rezeptor für die simultane komplexierung von anionen und kationen—erkennung von kh2po4,* Angewandte Chemie **106**, 480 (1994).

4

Visualization of unstained DNA nanostructures with advanced in-focus phase contrast TEM techniques

You cannot depend on your eyes when your imagination is out of focus.

Mark Twain

Over the last few years, tremendous progress has been made in visualizing biologically important macromolecules using transmission electron microscopy (TEM) and understanding their structure-function relation. Yet, despite the importance of DNA in all forms of life, TEM visualization of individual DNA molecules in its native unlabeled form has remained extremely challenging. Here, we present high-contrast images of unstained single-layer DNA nanostructures that were obtained using advanced in-focus phase contrast TEM techniques. These include sub-Ångstrom low voltage electron microscopy (SALVE), the use of a volta-potential phase plate (VPP), and dark-field (DF) microscopy. We discuss the advantages and drawbacks of these techniques for broad applications in structural biology and materials science.

This chapter has been published as: Yoones Kabiri, Raimond B. G. Ravelli, Tibor Lehnert, Haoyuan Qi, Allard J. Katan, Natascha Roest, Ute Kaiser, Cees Dekker, Peter J. Peters, and Henny Zandbergen, Visualization of unstained DNA nanostructures with advanced in-focus phase contrast TEM techniques, Scientific Reports, 9, 2019.

4.1. Introduction

Although TEM imaging of DNA, in its native unstained form, is crucial for various applications across life sciences, it has remained extremely difficult to obtain such images. The challenges of DNA imaging with TEM are indeed manifold. Unstained DNA has only been made visible if freely suspended, i.e., without carbon support, and success in these experiments was limited to specific DNA structures such as DNA bundles or fibers [1–6]. When DNA is deposited onto commercial carbon membranes in dry condition, no good contrast can be achieved. Unfortunately, reducing the carbon thickness to increase the DNA contrast is not trivial due to difficulties in manufacturing and handling of delicate carbon membranes, as well as due to non-conductive properties of amorphous carbon below 4 nm thickness [7], which strongly deteriorates the TEM imaging. Although the superior mechanical and electrical properties of graphene was conceived to provide a viable solution, the hydrophobic interaction between DNA and graphene has proven to be a major obstacle for imaging [8].

In this work, we aim to image unstained DNA nanostructures via modifications in the electron optics instead of addressing the sample preparation technicalities. We therefore choose the easiest route of sample preparation, which is support on commercially-available carbon membranes (i.e., not on delicate thin carbon supports) under dry conditions (i.e., not cryo-frozen [9]). This sample preparation route is thus very reproducible as well as accessible for every TEM lab. For convenient and reliable evaluation of double stranded (ds) DNA contrast, we utilize a single-layer DNA origami nanostructure (Figure 4.1). The use of a two-dimensional DNA origami is an innovative and very useful approach because the specific shape of the origami structure allows reliable and convenient evaluation of dsDNA contrast. In addition, it enables the application of single particle analysis (SPA) to a purely nucleic acid structure, instead of, for example, using DNA-bound protein structures. Imaging multi-layered three-dimensional DNA origami structures is not pursued in this report since we aim for visualization of DNA at the single-helix thickness.

Electron optics in TEM have seen multiple improvements in recent years. While the conventional TEM (CTEM) is an ideal tool for imaging materials science samples with atomic resolution, it performs poorly for visualization of radiation-sensitive biological molecules such as DNA. Therefore, in order to increase the contrast, electron microscopists have tried to develop phase contrast techniques under low-dose conditions with the help of phase plates or low-voltage TEM. However, various technological issues have impeded this goal. For example, a commercial phase plate has only been available since 2015, namely the VPP [10]. Previous generations of phase plates including the well-known Zernike-type were difficult to fabricate, align, and integrate into a SPA workflow. In the case of low voltage microscopy, the significant deterioration of resolution caused by the chromatic aberration (Cc) was the major limiting factor.

Here, we present high contrast TEM images of unstained DNA nanostructures onto commercial carbon membranes using advanced “in-focus” TEM techniques through manipulation of electron optics shown in Figure 4.2. Whereas CTEM renders poor contrast, we find that a chromatic and spherical aberration corrected (Cc+Cs) SALVE (sub-Ångstrom low voltage electron) microscopy, or the cosine-type phase shift induced by the VPP technology, resulted in an overall visibility of the DNA nanostructures, without

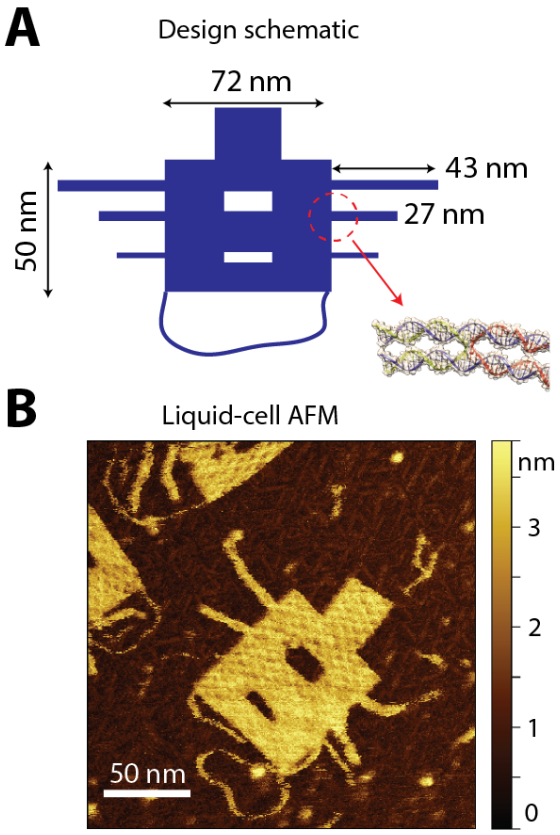

Figure 4.1: Single-layer DNA origami nanoplates as an innovative microscopy sample for single particle analysis. (A) Schematic of the 2D DNA origami design. The origami nanostructure contains various DNA features with different lengths and widths including symmetric side arms, cavities inside the main rectangle, and a floppy dsDNA loop at the bottom. The bottom-right inset illustrates the DNA helices equivalent. See Methods for the full details of the origami design. (B) Liquid-cell atomic force microscopy (AFM) image of an origami nanoplate on mica. Note that the bottom dsDNA loop as well as the single dsDNA arm (third from the top) depict a large flexibility. The high-resolution liquid-cell AFM image resolves Holliday junctions that are clearly distinguishable within the origami plate.

the need of labelling. This enabled the particle picking and class averaging algorithms in the SPA workflow. The SALVE images of the DNA origami extend its application to life science specimens, which makes the low-kV route an attractive approach for imaging of both materials science and biological specimens. Next to the small or flexible protein structures under cryo condition [11], we have here demonstrated VPP application for imaging the non-water embedded unstained nucleic acids. Furthermore, we show the visibility of DNA origami using the non-linear phase contrast DF technique. Finally, we discuss the prospect of SALVE and VPP techniques in terms of in-focus SPA workflow.

4.2. Results

Visualization of unstained DNA origami is not well possible with defocused CTEM. We were unable to detect sufficient contrast of DNA origami plates supported on commercial carbon membranes using the normal CTEM at 200-300 kV acceleration voltages, even with large defocus values (up to 10 μm) for the objective lens and even when the micrographs were acquired by a direct detector camera. The poor visibility of unstained 2D DNA origami on the commercial carbon membranes can be attributed to, on one hand, the low scattering of single DNA helix compared to relatively thick carbon support, and on the other hand, a large suppression of low-spatial frequencies in CTEM (supporting information (SI), Figure S4.1), that are essential for particle edge detection and the overall visibility of the weak phase objects. Electron optical imperfections such as spherical aberration together with objective lens defocus were historically used as rather constructive ways to convert the low-frequency phase components of the exit wave into intensity modulations, though associated with severe damping of the higher resolution fringes (SI, Figure S4.1). Nevertheless, this defocused CTEM approach could not render sufficient contrast to the origami plates supported on thick carbon membranes. Furthermore, acquisition of a good dataset in cryo-EM was not possible (exchanging the amorphous carbon substrate with amorphous ice). This could be attributed to the intrinsic floppy nature of the 2D DNA origami designs or the interfacial effects (air/water interface) during plunge-freezing step of cryo-EM sample preparation.

Taken all together, we thus note that the de facto defocused phase contrast method that is widely employed in the cryo-EM structure determination of proteins remains extremely challenging for contrast enhancement in our case study for non-water embedded DNA, which indeed makes the unstained single-layer DNA nanostructures one the most difficult samples to probe.

Low-kV (80 kV) CTEM facilitates the DNA detection but results in blurry images. In order to increase the DNA contrast in CTEM, one remedy is to decrease the acceleration voltage, ideally down to 80 kV, because considerable increase in scattering cross section (both elastic and inelastic) is expected, which consequently facilitates phase contrast imaging. Reducing the high voltage from 300 kV in our Cs-corrected Titan to 80 kV within the non-Cs-corrected Arctica microscope, shifts the contrast transfer function (CTF) peaks towards the low-frequency components in the frequency spectrum (Figure 4.3A). This is also indeed accompanied by a different performance of the detector as well as yielding a different amplitude contrast. Using this approach, we were able to detect a sufficient amount of contrast in single-frame acquisitions (Figure 4.3B) at 80 kV acceleration voltage, which enabled the particle picking and consequently SPA. Figure 4.3D

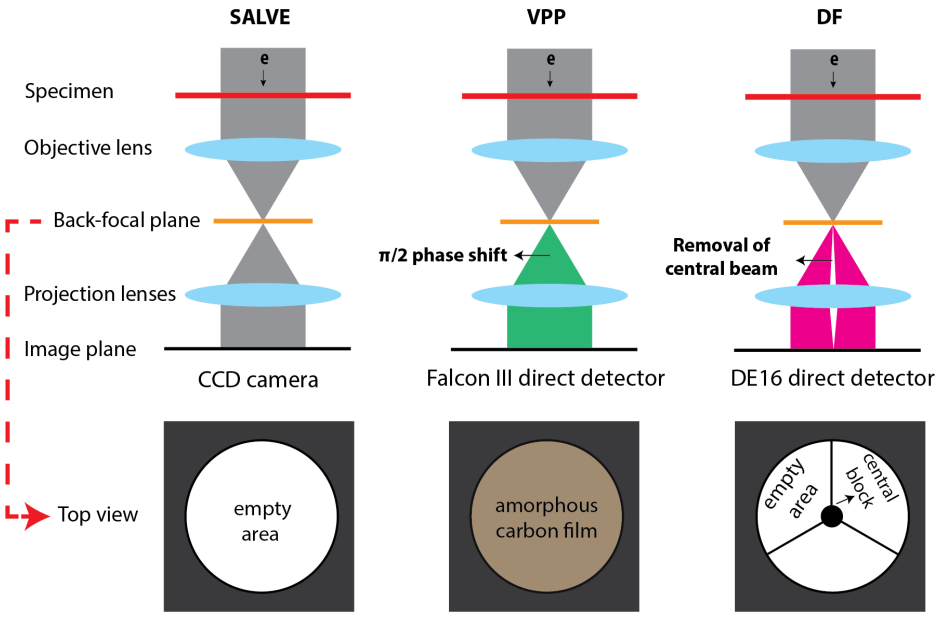

Figure 4.2: Schematics of in-focus phase contrast TEM techniques. The objective aperture design in the back-focal plane of the microscope for each technique is shown enlarged at the bottom row. SALVE technique does not require any special objective aperture design at the back-focal plane, whereas for contrast enhancement of DNA at high kV, $\pi/2$ phase shift or removal of the un-scattered zero beam is needed for VPP and DF, respectively. See the literature for the contrast enhancement mechanisms [10, 12, 13]

shows the 2D class-averaged image after CTF correction. We observe that the side arms of the origami, each having a 4 nm width, as well as the small cavity inside the rectangle (4nm x 19.2nm) are either severely blurry or hidden. This low-resolution reconstruction indicates the importance of Cs-correction in order to obtain high-resolution images. Prior to reconstruction, low-resolution outcome could also be predicted based on the CTF plot in Figure 4.3A, where a considerable decrease in information limit is seen, down to 3.3 Å compared to 2 Å at 200 kV operation voltage of the Arctica microscope (SI, Figure S4.1). In the next section, we proceed to correct for the aberrations.

Cc+Cs correction at low-kV (20 kV, SALVE) strongly improves the contrast and resolution. Low-kV (i.e. 80 kV down to 20 kV) phase contrast electron microscopy was historically abandoned since the chromatic aberration of the objective lens severely deteriorated the resolution [14]. With the elimination of chromatic aberration, the resolution substantially improves at 20 kV (Figure 4.3E, where we see pronounced low-frequency transfer as well as an improved information limit beyond 2 Angstrom). Recently, atomic resolution at 20 kV was successfully realized within the framework of the SALVE project [13]. This is a remarkable step towards studying sensitive samples below 80 kV prone to knock-on damage like graphene [13]. However, hydrogen-containing specimens are still challenging to image [15]. To probe what is possible, we thus imaged the DNA origami plates with the Cc+Cs corrected SALVE microscope to remove the severe delocalization effects at low-kV and at the same time obtain enough contrast for visualization of unstained DNA.

We find that the DNA origami reconstruction using the low-kV dataset provides excellent contrast (see Figure 4.3H). Strikingly, we observe that the detailed DNA structural features such as the smaller cavity and the single DNA helices become visible using class averaging of a relatively small number of manually acquired frames (~100 micrographs). Increased total scattering cross section at 20 kV, together with enhanced low-frequency information transfer, boosts the phase contrast of the DNA. Specifically, Cc correction has an important role which enables focusing both the elastic and inelastic electrons into the same imaging plane and hence strengthening the contrast. Here, we presented first images of single-helix-thick unstained DNA nanostructures supported on commercial carbon supports at 20 kV obtained with the new Cs+Cs corrected technology. Our results extend SALVE microscope application for biomolecular imaging.

Volta-potential phase plate substantially boosts the DNA contrast at high voltages. Although the SALVE microscope did provide pivotal results, the instrument availability is still very limited. Furthermore, various practical challenges should be overcome in terms of automation in data acquisition, cryo compatibility, and etc. If working at standard high kVs (100-300 kV) is desired (which is the norm in most TEM labs), one should tackle the historical CTF obstacle. One possible route to enhance the contrast of weak phase objects at high kV is to improve the low frequency transfer of the CTF, e.g., by changing the conventional sine-type (zero phase shift) into a cosine-type (i.e., $\pi/2$ phase shift). Then, a pronounced phase contrast at near-focus can become possible. Note, for example, the significant revival of the low-frequency components in the dashed area of Figure 4.3I after inducing a 0.5 π phase shift. To realize this type of CTF performance, we employed a recent VPP technology in CTEM to probe the DNA contrast at 200 kV.

Importantly, we find that VPP micrographs display exceptionally good contrast for

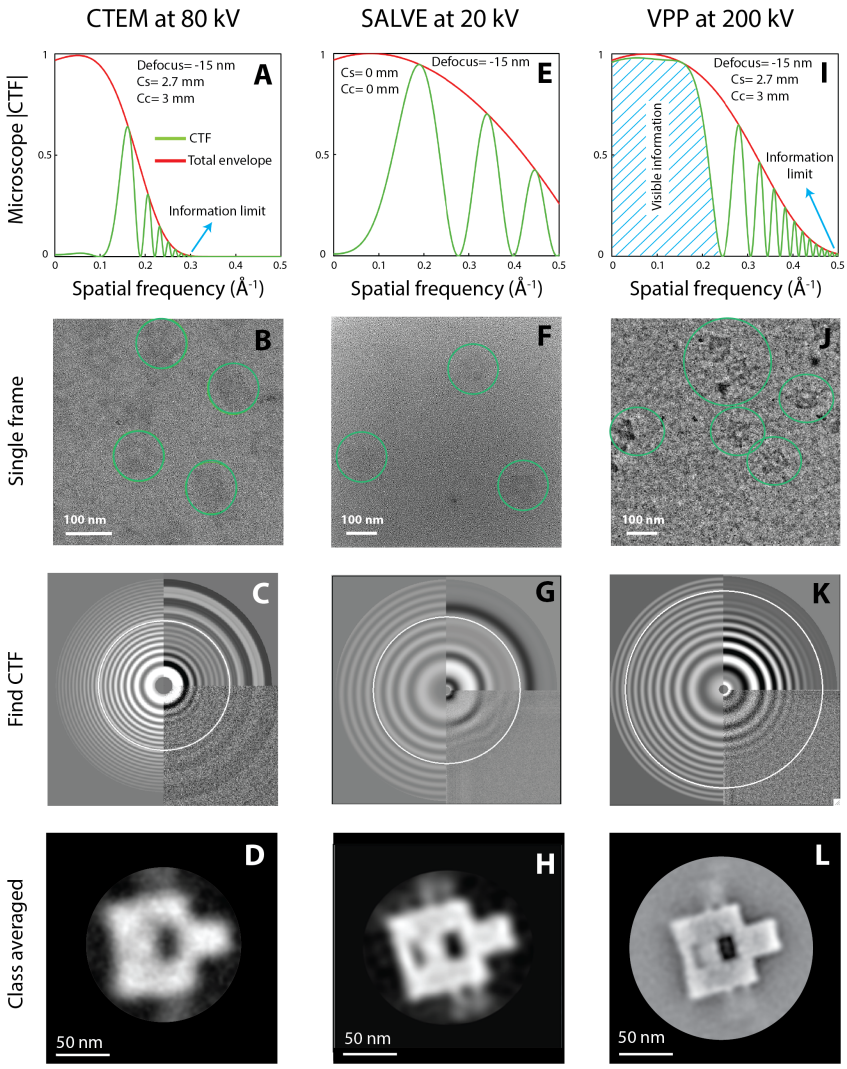

Figure 4.3: SPA results for imaging unstained DNA origami nanoplates supported on commercial carbon films. The figure compares three techniques: Column (A-D) shows results for 80 kV CTEM; column (E-H) for 20 kV SALVE microscope with Cs+Cc correction; and column (I-L) for VPP at 200 kV without Cs and Cc correction. (A, E, I) Theoretical CTF plots at near focus (green curves). The red curves indicate the total envelopes (spatial and temporal). We observe a significant resolution drop at 80 kV for CTEM due to pronounced Cs aberration, but do not observe this in the SALVE microscope. After implementing a VPP in a CTEM microscope, it is evident that the low spatial frequencies are hugely enhanced (the dashed area in panel I). We consider 0.1 amplitude contrast in all the CTF plots. (B, F, J) Single frame acquisitions. Sufficient contrast is achieved in each technique for enabling the particle picking and consequently SPA. Noticeably, the VPP depicts remarkable contrast in single frames. (C, G, K) Processed CTFs of micrographs. (D, H, L) SPA reconstructions. The CTEM reconstruction results in a blurry image due to presence of Cs aberration. Excitingly, the two novel approaches, SALVE and VPP, can alternatively be used to render sufficient contrast as well as good resolution for DNA imaging.

unstained DNA (Figure 4.3J). We observe even the side arms of the DNA origami plates without class-averaging. Such VPP images imply that the low-spatial frequencies play crucial role in the overall visibility of the DNA nanostructures. Owing to the striking DNA contrast in single acquisitions, the class averaging of the origami plates could be achieved with only a handful (~2000) of particles. The reconstructed image (Figure 4.3L) provides a detailed view of all the DNA spatial features that were incorporated in the origami design, e.g., the side arms (2 and 4 nm wide), and the cavities inside the rectangle (4 and 8 nm wide). We thus demonstrated the applicability of VPP at high kV, for imaging unstained single-layer flat nucleic acids on commercial carbon supports, resolving features down to the level of single dsDNA molecules.

Conjugating a VPP with CTEM without Cs correction at 200 kV was sufficient to obtain a good reconstruction of the origami plates. For our case study of nucleic acids, revival of low-frequency components in the frequency spectrum has proven to play a more significant role than the expensive aberrations correction. The versatility brought by VPP to be used in conjugation with a non-Cs-corrected microscope at high kV is indeed a tremendous advantage compared to other phase contrast techniques.

Dark-field microscopy provides necessary contrast for DNA visualization at high voltages but is not suitable for SPA. Alternatively, dark-field microscopy could be another approach for contrast enhancement at high kVs. The conventional DF and scanning TEM (STEM) techniques are the prevailing methods in materials science for studying inorganic samples. Since the diffracted beams in such inorganic samples are stronger (compared to biomolecules), the collection of only a fraction of diffracted beams suffices to form a DF image. However, in the case of single-DNA origami structures, a DF image can only be formed with high contrast after all scattered electrons are gathered in the wide-field TEM mode. For this reason, we fabricated a “Mercedes star” aperture (Figure 4.4A) to remove the unscattered central beam while letting virtually all the scattered beams pass through. The aperture consists of a very delicate ion-milled central disc of 1 μm in diameter, and a cut-off frequency of 1 Angstrom (Figure 4.4B), see the Methods section of the manuscript for details on the aperture fabrication and imaging.

Interestingly, we find that utilization of a DF aperture in conjugation with a direct electron camera leads to DNA visualization at 300 kV (Figure 4.4E). Whereas these DF acquisitions exhibit high contrast, the counterpart images of DNA nanoplates in bright-field TEM mode remain invisible (Figure 4.4C). Note that acquisition and illumination parameters are the same in Figure 4.4C and 4.4E, except that the DF aperture is inserted and aligned in the back-focal plane in Figure 4.4E. We previously imaged the positively stained origami structures with DF using a conventional CCD camera [8]. But, the unstained images (current work) were not optimal until we replaced the CCD with a direct electron device (DE-16 Direct Electron, California). The is related to the lower noise and higher detective quantum efficiency (DQE) of direct electron cameras, which facilitates the contrast in DF.

With the DF technique, we intended to probe for an easier replacement for SALVE and VPP for facile visualization of weak-phase objects at high kVs. The DF technique is indeed easy and helpful for sample screening, especially because the DF aperture can be easily integrated into the objective aperture holder of any TEM machine without high costs. One should note that the size of DF aperture would differ substantially at low kVs

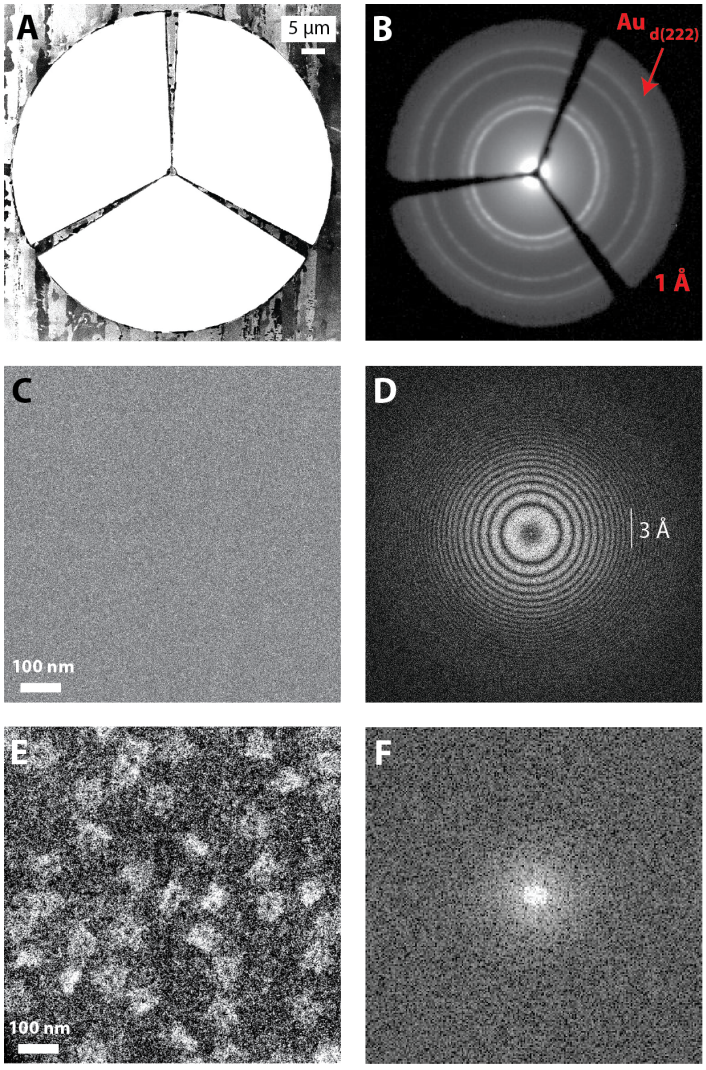

Figure 4.4: Dark-field visualization of unstained DNA nanostructures. (A) Fabrication of the delicate DF aperture by FIB milling on a 5-µm thick platinum foil. (B) Image of the aperture located in the diffraction plane. We see blocking of the zero beam, and a cutoff frequency of about 1 Angstrom (calibrated by a polycrystalline Au sample). (C, E) Bright- and dark-field images of the DNA nanostructures, respectively. We observe that the DNA structures are invisible in bright-field, but they do appear visibly in the dark-field image after insertion of the DF aperture. (D, F) Fourier transform of high-resolution images in panels C and E, respectively. The absence of carbon Thon rings in panel F is attributed to removal of central beam (linear interaction is absent). Thon rings in panel D are seen to extend beyond 3 Angstrom, which indicates a good performance of the DE-16 direct detector camera.

due to expansion of diffraction space. Moreover, the image contrast would be affected by the residual Cs at the low kVs [8]. Therefore, DF imaging below 300 kV was not desired or conducted. Since alignment of the DF aperture should be carried out before every DF acquisition, and due to absence of Thon rings (Figure 4.4F) that are critical for defocus measurement and data acquisition, it is unlikely that DF would become a routine in the SPA workflow [16], until further software and automation obstacles are overcome.

4.3. Discussion

We presented high contrast images of unstained single-layer DNA nanostructures on commercial carbon membranes using advanced in-focus phase contrast TEM techniques. We notice significant contrast enhancement at low acceleration voltages such as 20 kV, which was possible via Cs+Cc aberration correction (in the SALVE approach), or at high acceleration voltages such as 300 kV after inducing $\pi/2$ phase shift (in the VPP approach).

To understand and compare the suitability of SALVE and VPP for SPA in structural biology, one should consider the effect of defocus. Indeed, phase contrast methods that deliver both contrast and resolution at in-focus conditions (< ±100 nm) are highly desired since they provide computational advantages over the prevailing defocused-based CTEM approaches in terms of data processing [17]. SALVE and VPP techniques differ from CTEM since they can be fully exploited at the in-focus conditions. Therefore, we discuss the effect of defocus on the expected resolution for these two techniques. Note that our definition of expected resolution for the in-focus condition differs substantially from the one mostly used in materials science, i.e., that is the information limit (as indicated in Figure 4.3A). We define the resolution based on the 0.5 amplitude threshold in the CTF plot without any zero-crossing at the low-frequency domain of the CTF [17].

Figure 4.5 depicts the effect of defocus on the expected resolution for SALVE and VPP. Let us start to investigate such an effect for the SALVE approach (Figure 4.5A-B). Figure 4.5A shows SALVE CTF plots at three different defocus values. At zero focus (green dotted line), we expect a 2.4 Å resolution based on the |CTF=0.5| criterion. This point is indicated as * in both panel A and B. Over-focusing (defocus>0) shifts this peak to the left-hand side of the frequency spectrum, where its amplitude reaches the |CTF=0.5| threshold without any phase flipping at the low spatial frequencies, resulting in drop of resolution from 2.4 Å at zero focus to about 10 Å at +30 nm defocus. The right curve in Figure 4.5B thus shows the resolution evolution for the defocus>0 illumination. On the contrary, for under-focus values (defocus<0), we observe that a second peak develops in the CTF plot (see the red dashed curve for -3 nm defocus). At -5 nm defocus, it fulfils the |CTF=0.5| criterion at the resolution of 3.1 Å, indicated as in both panel A and B. Greater under-focus values deteriorate the expected resolution from 3.1 Å at -5 nm defocus to 10 Å at -25 nm defocus (left curve in Figure 4.5B depicting the resolution evolution for defocus<0 illumination). The green-highlighted area in Figure 4.5B is restricted according to CTF performance, meaning that obtaining better resolution would not be possible. We note that the allowed defocus range at certain resolution is very narrow in the SALVE technique, which practically affects the SPA data collection.

For the VPP technique, similar analyses are provided in Figure 4.5C-D. The major difference in VPP CTF is the cosine-type CTF. Note that the cut-on frequency is ignored in these plots and we consider complete 0.5 π phase shift performance for the volta-

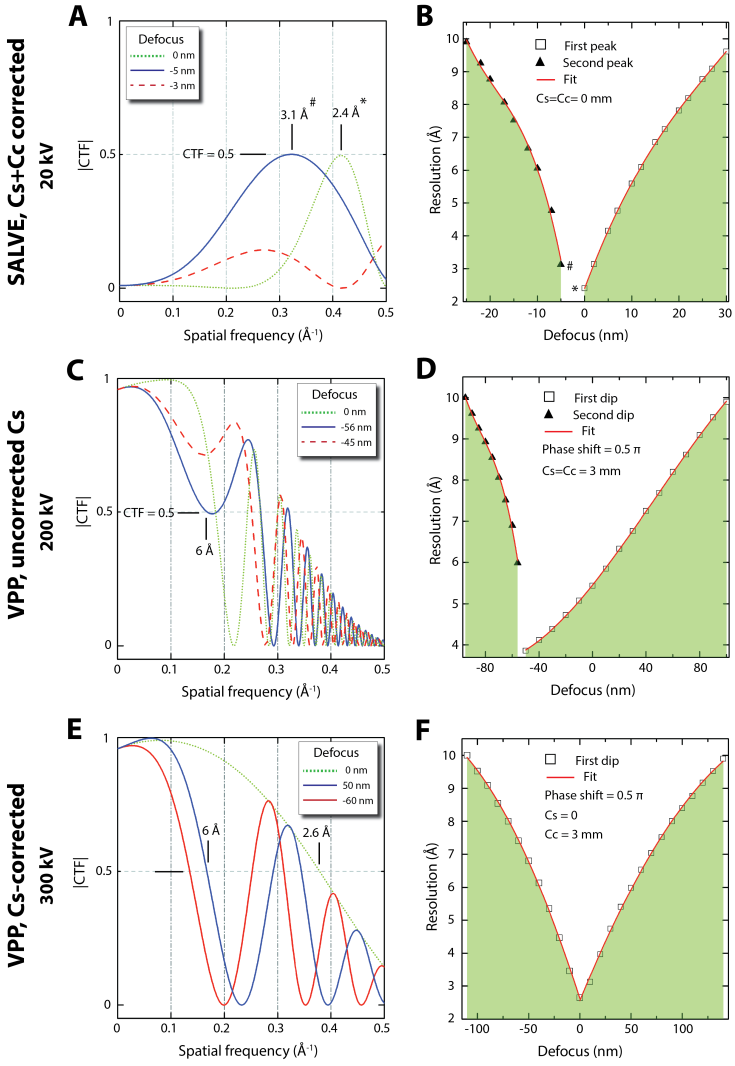

Figure 4.5: Effect of focus on the expected resolution for VPP and SALVE techniques. (A, C, E) Representative CTF plots at different focus values for SALVE, non-corrected VPP and Cs-corrected VPP, respectively. The resolution criterion is 0.5 amplitude threshold in each CTF plot. (B, D, F) Expected resolution vs defocus for each technique mentioned above. The data points are extracted according to CTF plots (see, for example, the * and in panels A and B). The green highlighted areas are prohibited in terms of 0.5 CTF criterion. These analyses indicate that the defocus range for SALVE technique is very narrow, which makes the data acquisition very challenging. On the contrary, VPP depicts a greater defocus tolerance at comparable resolution, hence facilitating the SPA workflow. We also note that removing the Cs could further improve the VPP performance in terms of resolution and permitted defocus range.

potential phase plate. We find that VPP allows for a greater acceptable defocus range, indicating that VPP is a superior technique than SALVE for SPA in terms of in-focus data collection. Figure 4.5E-F shows the effect of Cs correction on VPP. This CTF performance can nowadays be achieved with a commercial Titan Krios instrument equipped with VPP operating at 300 kV. We see that removing Cs in conjugation with a 0.5 π VPP phase plate increases the allowed defocus range at comparable resolution (compare with Figure 4.5D). Moreover, the observed phase-flipping in the CTFs of SALVE and VPP following over- or under-focusing is absent in the Cs-corrected VPP, where we obtain a symmetric defocus-resolution plot in Figure 4.5F.

TEM imaging of unstained nucleic acids opens up ample opportunities in life sciences. Studying label-free DNA-protein interactions, imaging the native chromatin structure, and imaging conjugated DNA nanostructures are just a few examples. More specifically, the 2D DNA origami, with its ample and diverse available sequences at its surface, provides a promising approach for biophysical assays such as probing sequence-specific protein interactions. It has been a long endeavor to develop TEM techniques for such applications. In the current work, we have shown that such images can be obtained using advanced in-focus phase contrast TEM techniques. Although our focus was on imaging nucleic acids, the insights provided by these techniques will be of further interest for broader applications in structural biology and materials science.

4.4. Methods

2D DNA origami design

A 2D DNA origami was designed (Figure 4.1A) in order to have the same scattering yield as in a single dsDNA molecule. The rectangular shape of the origami facilitates its detection on carbon membranes and enables particle picking and consequently SPA. The full details of the origami design and its characterization can be found elsewhere [8]. An additional side arm was incorporated in the design to have single DNA helix (~2 nm as in B-form DNA) extruding from the oligomer sequence within the main rectangle. The liquid-cell AFM data (Figure 4.1B) showed that this arm was very flexible and therefore hard to resolve in the TEM class averaging.

TEM sample preparation

The investigated samples were similar for all of the techniques discussed in this manuscript. They were unstained single-layer DNA origami (Figure 4.1) deposited on commercially available TEM grids (Electron Microscopy Science, USA, 3-4 nm carbon supported on 5-6 nm formvar). 3 µL of purified origami sample with a concentration of 5 nM was drop casted on freshly glow-discharged TEM grids, and left to incubate for 2 minutes. Subsequently, the grids were thoroughly washed with Milli-Q water and gently blown dry with a nitrogen flow. Following this protocol, we achieve a high density and homogenous distribution of the DNA origami plates on TEM grids.

SALVE data acquisition and processing

The Cc+Cs corrected SALVE microscope was operated at 20 kV to image DNA origami. The aberration coefficients Cc and Cs were tuned to -10 µm and -20 µm, respectively.

The microscope is equipped with a Ceta 16M camera (FEI). The exposure time was set to 1s and a dose rate of 61 e $s^{-1}nm^{-2}$ was applied for the manually collected dataset. After initial screening of the dataset, the low-kV collected dataset contained 108 images. The CTFs were fitted on the dose-weighted micrographs with Zhang's Gctf (Kai Zhang, 2015), a GPU-accelerated program for real-time CTF determination and correction. The following parameters were used: spherical aberration -20 µm, voltage 20 kV, amplitude contrast 0.1, minimum resolution 40 Å, maximum resolution 4 Å, minimum defocus 1000 Å, maximum defocus 10000 Å (step size 500 Å). Additionally, the astigmatism was 500 Å, B-Factor of 300 Å and the additional validation option was used. After visual inspection, 92 CTF-corrected images were used for the selection of particles. Particle picking was carried out manually using the GPU-accelerated beta version of Relion 2.1 (Scheres, 2017), with a particle diameter of 1500 Å, pixel size 1.698 Å. Particles were extracted with a box size 1024, based on the particle diameter and pixel size. From the 92 images, 240 particles were extracted and were subjected to 2D-classification using the following parameters: 5 classes, with regularization parameter of 3, 25 iterations and a mask diameter of 1600 Å. After 2D classification, the particles were sorted and selected on a Zmas score of 0.8. These particles were again subjected to 2D classification (3 classes, regularization parameter 3, 25 iterations and a mask diameter of 1600 Å).

VPP data acquisition and processing

The data was collected on an FEI Tecnai Arctica (FEI) cryogenic TEM, operated at 200kV and equipped with a Falcon III detector (FEI). The data was acquired using the following parameters: magnification x53,000, 50 µm C2 aperture, spot size 5, 40.718% C2 lens, 35.129% diffraction lens, pixel size 1.97 Å, dose rate on the detector 47.7 electrons/pixel/s. The data was acquired by the automatically with EPU software (FEI). The phase plate was aligned to provide optimum phase shift performance. Exposure time 5s, with 200 frames and 20 fractions per movie (10 frames/fraction). The periodicity of the phase plate was set to 50 exposures, with an activation time of 10 s. After initial screening of the dataset, the VPP collected dataset contained 1848 images. The movies were aligned using MotionCorr2. Parameters were 5 x 5 patches, dose-weighting 2 electrons/$Å^2$, pixel size 1.97 Å and a b-factor of 100 was applied. The CTFs were fitted on the dose-weighted micrographs with Zhang's Gctf (Kai Zhang, 2015). The following parameters were used: spherical aberration 2.7 mm, voltage 200kV, amplitude contrast 0.1, minimum resolution 30 Å, maximum resolution 4 Å, minimum defocus 1000 Å, maximum defocus 10000 Å (step size 500 Å), minimum phase shift 20 degrees, maximum phase shift 160 degrees with a step size of 10 degrees, the astigmatism was 150 Å and the additional validation option was used. After visual inspection, 1720 CTF-corrected images were used for the selection of particles. Particle picking was carried out manually using the GPU-accelerated beta version of Relion 2.1 (Scheres, 2017), with a particle diameter of 1500 Å, pixel size 1.97 Å. Particles were extracted with a box size 1024, based on the particle diameter and pixel size. From the 1720 images, 2193 particles were extracted and were subjected to 2D-classification using the following parameters: 3 classes, with regularization parameter of 2, 25 iterations and a mask diameter of 1600 Å. After 2D classification, the particles were sorted and selected on a Zmas score of 0.8. These particles were again subjected to 2D classification (3 classes, regularization parameter 3, 25 iterations and a mask diameter of 1600 Å).

Dark-field image acquisition

The DF images were acquired in a post-specimen Cs-corrected Titan microscope. The DF aperture, which is positioned and aligned in the back-focal plane (Figures 4.2 and 4.4), was fabricated by a FEI Helios dual beam machine assisted by an automated CAD software for milling, see full details of our DF aperture fabrication and alignment procedures provided elsewhere [8]. Briefly, the microscope was initially aligned in bright-field mode to remove the Cs and axial aberrations such as astigmatism. The DF aperture was then inserted and aligned in the diffraction space. No change in astigmatism was observed after DF aperture insertion, tested via image sharpness of small (5 nm) Au nanoparticles (since the FFT of DF images lack Thon rings to correct for astigmatism). A direct electron camera (DE-16, Direct Electron, California) was employed to efficiently collect all the scattered electrons (Figure S4.2).

CTEM

The CTEM data were recorded with the same VPP microscope, though the phase plate capability was switched off and the operating voltage was tuned down to 80 kV. This microscope features uncorrected Cs and Cc values of 2.7 mm and 3 mm, respectively.

4.5. Supporting Information

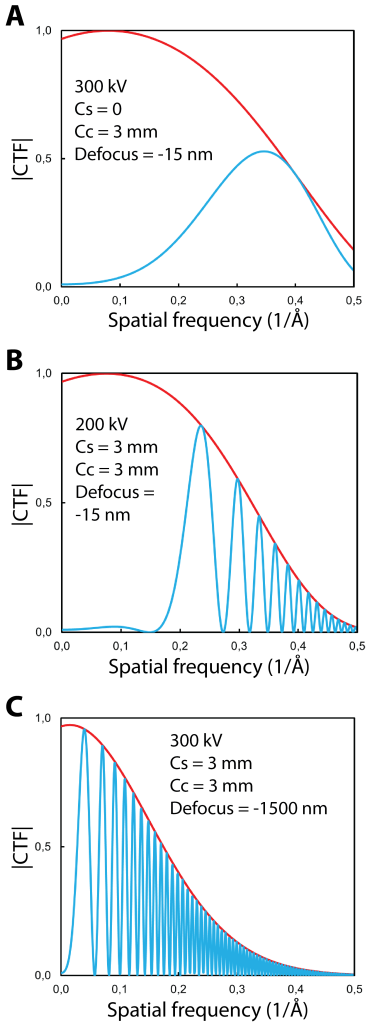

Figure S4.1: CTFs (blue curves) for (A) a Cs corrected Titan microscope operating at 300 kV (B) a non-corrected Arctica microscope operating at 200 kV (C) a non-corrected Titan microscope at 300 kV under strong defocus illumination. The red curves are the total envelope function (temporal and spatial).

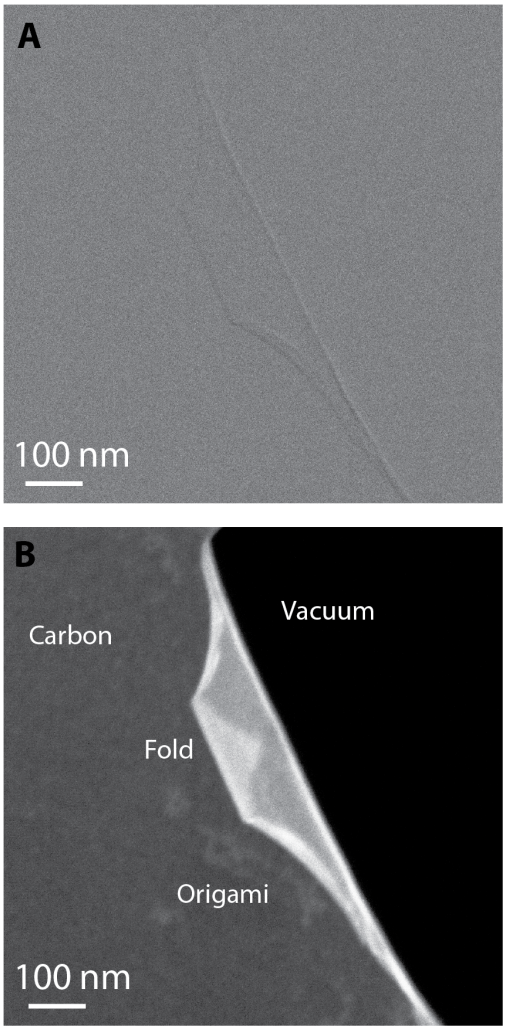

Figure S4.2: DF imaging performance in conjugation with DE-16 camera. (A) Bright-field and (B) DF image of a same area on the sample. Remarkable contrast enhancement is see after inserting DF aperture.

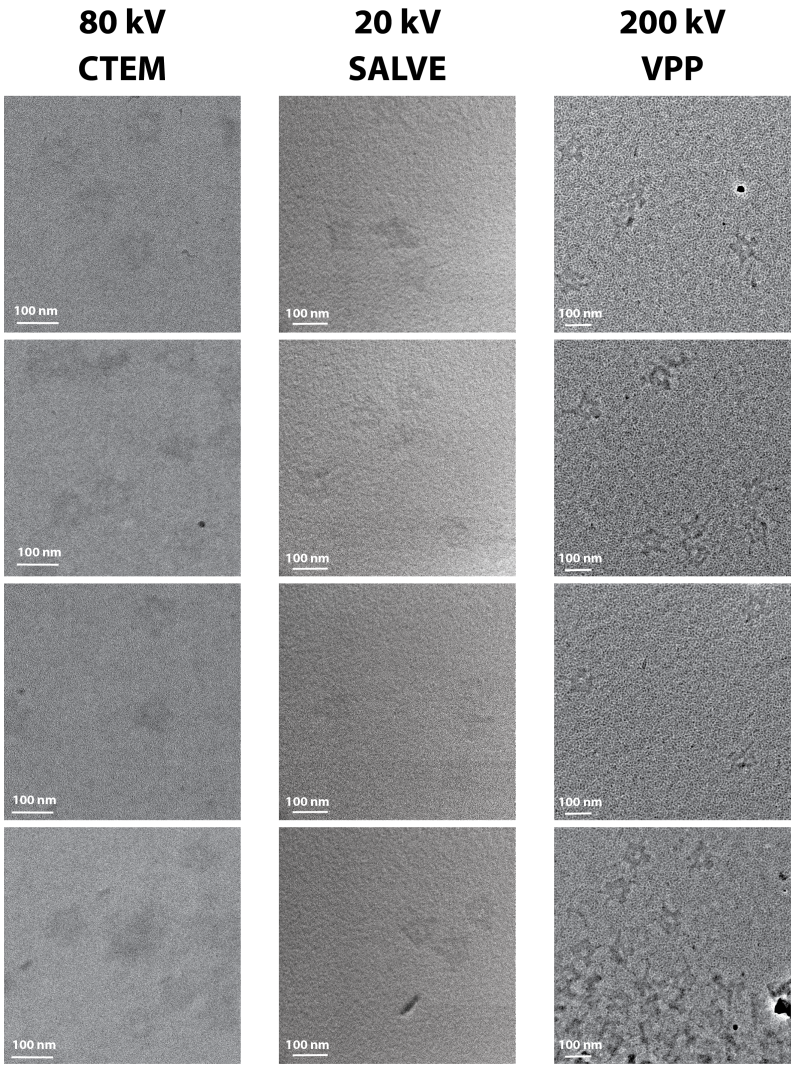

Figure S4.3: Additional exemplary micrographs. More data will be deposited in the Electron Microscopy Public Image Archive (EMPIAR).

We fabricated and tested our own Zernike-type phase plate (Figure S4.4). The Zernike phase plate is known for providing a uniform and complete $\pi/2$ phase shift, and it features a thin suspended carbon membrane in the back focal plane of the objective lens. A hole is drilled in the center of the carbon membrane (Figure S4.4C) to allow the unscattered zero beam passes through while the scattered electrons pass the carbon and hence the inner potential of the carbon atoms induces a phase shift between the scattered and unscattered electrons, the main mechanism for enhancing the contrast of the weak phase biomolecules in TEM. The thicknesses of about 15-30 nm is required for a $\pi/2$ phase shift for a TEM machine operating at 300 kV such as our Titan microscope in Delft [18, 19]. In order to reduce the noise contributed by the inelastic scattered electrons, it is better to keep the carbon thickness below 20 nm. In addition, the carbon membrane should be heated during operation of the Zernike phase plate, otherwise huge contamination is built around the central hole which degrades the performance of the phase plate quickly [20]. However, heating the whole aperture in the back focal plane causes a lot of drift and hence alignment of the central hole (1 µm in diameter) becomes challenging.

Instead of joule heating of the whole objective aperture, alternatively we incorporated a MEMS device based on platinum resistive spiral heaters embedded in a SiN membrane (Figure S4.4B). The nanofabrication process of such MEMS device is discussed elsewhere [21]. The heater design was altered to be able to incorporate a 70 µm aperture inside the platinum spirals, and to fabricate the Zernike phase plate on top of it. Each chip consists of two heater spirals and hence two Zernike phase plates can be constructed on the back focal plane. The final design of the Zernike phase plate should consist of a thin layer of a carbon with a hole in the middle. However, the normal heater chips consist of 20-50 nm SiN on the aperture. Figure S4.4A shows how we remove and replace the SiN with carbon. Carbon (18 nm) was evaporated on the backside and later the SiN was removed on the top side with dry etching process. We used electron energy spectroscopy (EELS) to confirm the removal of the SiN (Figure S4.4B) as well as extensive TEM and SEM imaging to assure the quality of the final suspended carbon on aperture. Finally, we drilled the hole (0,5 and 1 µm) in the middle of the carbon with focused ion beam (Helios, ThermoFisher Scientific).

We tested the phase plate without the heating option of the device. Insertion into the TEM and wire connections (through wire bonding) was a delicate work since the pole piece gap of the objective lens should remain well isolated from the electric circuits on top of the heater chip. Figure S4.5 summarized our imaging results with the Zernike phase plate. We could not obtain a reliable image due to presence of platinum ring around the central hole (Figure S4.5B-C). For future experiments, complete removal of this platinum ring seems necessary since we experienced challenges during the alignment in the back focal plane of the microscope.

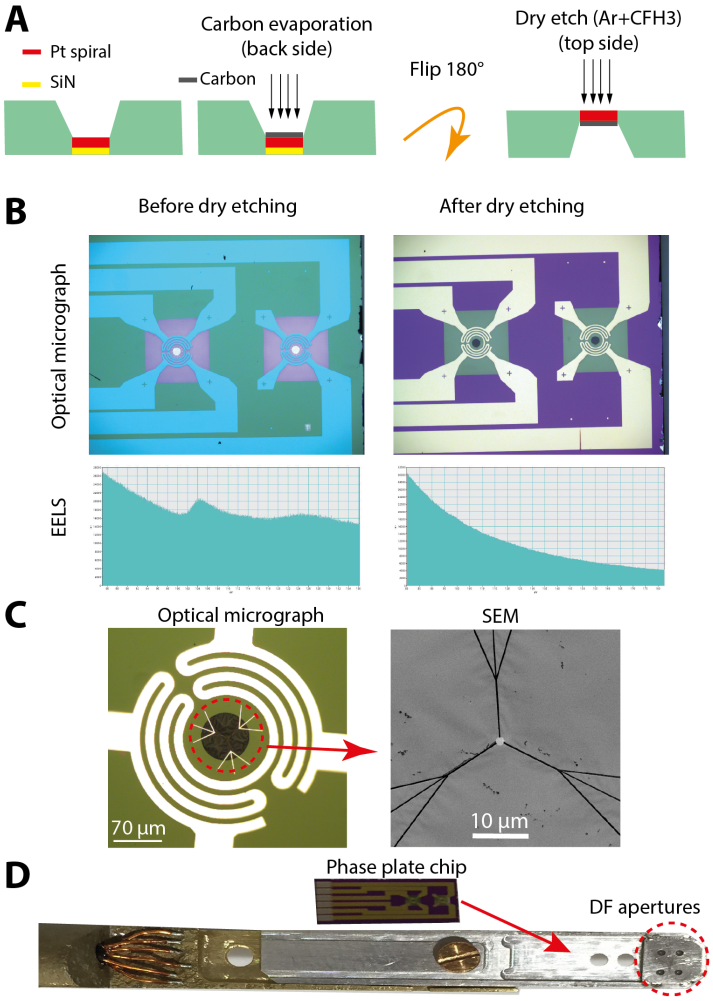

Figure S4.4: Fabrication of a Zernike phase plate based on MEMS heaters. (A) Nanofabrication process. (B) SiN removal check using EELS. Silicon L-edge is absent, indicating complete removal of SiN. (C) Optical micrograph of one Zernike aperture with the close-up SEM image of the central hole. (D) Image of the aperture holder that situates in the back focal plane.

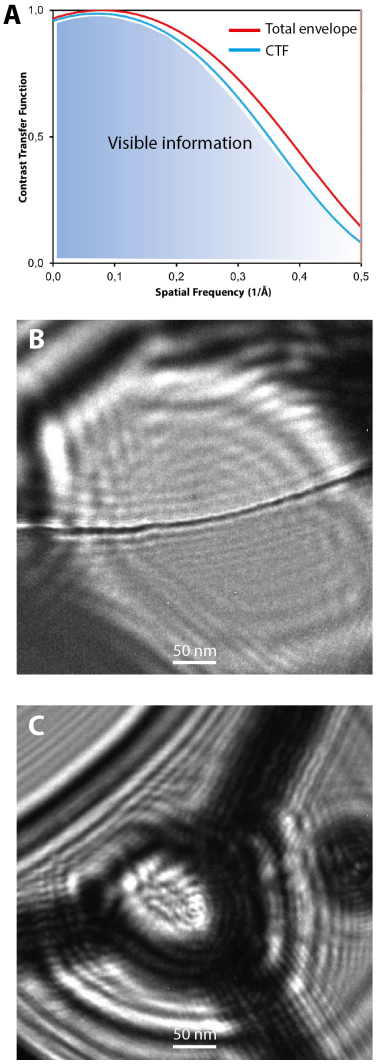

Figure S4.5: Results of Zernike phase plate imaging. (A) CTF of the Titan microscope with full pi/2 phase shift at 300 kV and at near focus. (B,C) TEM images containing the shadow image and fringes of the platinum ring of the phase plate.

References

[1] M. Marini, A. Falqui, M. Moretti, T. Limongi, M. Allione, A. Genovese, S. Lopatin, L. Tirinato, G. Das, B. Torre, *et al.*, *The structure of dna by direct imaging,* Science advances **1**, e1500734 (2015).

[2] F. Gentile, M. Moretti, T. Limongi, A. Falqui, G. Bertoni, A. Scarpellini, S. Santoriello, L. Maragliano, R. Proietti Zaccaria, and E. di Fabrizio, *Direct imaging of dna fibers: the visage of double helix,* Nano Letters **12**, 6453 (2012).

[3] Y. Takai, T. Nomaguchi, S. Matsushita, and Y. Kimura, *Molecular-scale imaging of unstained deoxyribonucleic acid fibers by phase transmission electron microscopy,* Applied physics letters **89**, 133903 (2006).

[4] Y. Fujiyoshi and N. Uyeda, *Direct imaging of a double-strand dna molecule,* Ultramicroscopy **7**, 189 (1981).

[5] M. Marini, T. Limongi, A. Falqui, A. Genovese, M. Allione, M. Moretti, S. Lopatin, L. Tirinato, G. Das, B. Torre, *et al.*, *Imaging and structural studies of dna–protein complexes and membrane ion channels,* Nanoscale **9**, 2768 (2017).

[6] T. G. Martin, T. A. Bharat, A. C. Joerger, X.-c. Bai, F. Praetorius, A. R. Fersht, H. Dietz, and S. H. Scheres, *Design of a molecular support for cryo-em structure determination,* Proceedings of the National Academy of Sciences **113**, E7456 (2016).

[7] D. M. Larson, K. H. Downing, and R. M. Glaeser, *The surface of evaporated carbon films is an insulating, high-bandgap material,* Journal of structural biology **174**, 420 (2011).

[8] Y. Kabiri, A. N. Ananth, J. van der Torre, A. Katan, J.-Y. Hong, S. Malladi, J. Kong, H. Zandbergen, and C. Dekker, *Distortion of dna origami on graphene imaged with advanced tem techniques,* small **13**, 1700876 (2017).

[9] E. Y. Chua, V. K. Vogirala, O. Inian, A. S. Wong, L. Nordenskiöld, J. M. Plitzko, R. Danev, and S. Sandin, *3.9 å structure of the nucleosome core particle determined by phase-plate cryo-em,* Nucleic acids research **44**, 8013 (2016).

[10] R. Danev, B. Buijsse, M. Khoshouei, J. M. Plitzko, and W. Baumeister, *Volta potential phase plate for in-focus phase contrast transmission electron microscopy,* Proceedings of the National Academy of Sciences **111**, 15635 (2014).

[11] M. Khoshouei, M. Radjainia, A. J. Phillips, J. A. Gerrard, A. K. Mitra, J. M. Plitzko, W. Baumeister, and R. Danev, *Volta phase plate cryo-em of the small protein complex prx3,* Nature communications **7**, 10534 (2016).

[12] C. Zhang, Q. Xu, P. J. Peters, and H. Zandbergen, *The use of a central beam stop for contrast enhancement in tem imaging,* Ultramicroscopy **134**, 200 (2013).

[13] M. Linck, P. Hartel, S. Uhlemann, F. Kahl, H. Müller, J. Zach, M. Haider, M. Niestadt, M. Bischoff, J. Biskupek, *et al.*, *Chromatic aberration correction for atomic resolution tem imaging from 20 to 80 kv,* Physical review letters **117**, 076101 (2016).

[14] U. Kaiser, J. Biskupek, J. Meyer, J. Leschner, L. Lechner, H. Rose, M. Stöger-Pollach, A. Khlobystov, P. Hartel, H. Müller, *et al.*, *Transmission electron microscopy at 20 kv for imaging and spectroscopy,* Ultramicroscopy **111**, 1239 (2011).

[15] T. W. Chamberlain, J. Biskupek, S. T. Skowron, P. A. Bayliss, E. Bichoutskaia, U. Kaiser, and A. N. Khlobystov, *Isotope substitution extends the lifetime of organic molecules in transmission electron microscopy,* small **11**, 622 (2015).

[16] R. M. Glaeser, *Invited review article: Methods for imaging weak-phase objects in electron microscopy,* Review of Scientific Instruments **84**, 312 (2013).

[17] R. Danev and W. Baumeister, *Cryo-em single particle analysis with the volta phase plate,* Elife **5**, e13046 (2016).

[18] R. Danev, R. M. Glaeser, and K. Nagayama, *Practical factors affecting the performance of a thin-film phase plate for transmission electron microscopy,* Ultramicroscopy **109**, 312 (2009).

[19] R. Danev and K. Nagayama, *Transmission electron microscopy with zernike phase plate,* Ultramicroscopy **88**, 243 (2001).

[20] K. Nagayama, *Phase contrast enhancement with phase plates in electron microscopy,* Advances in imaging and electron physics **138**, 69 (2005).

[21] M. Neklyudova, A. Erdamar, L. Vicarelli, S. Heerema, T. Rehfeldt, G. Pandraud, Z. Kolahdouz, C. Dekker, and H. Zandbergen, *Through-membrane electron-beam lithography for ultrathin membrane applications,* Applied Physics Letters **111**, 063105 (2017).

5

Probing DNA nanostructures in graphene/SiN nanocapillaries with liquid-phase STEM

Replace judgment with curiosity.

Lynn Nottage

It would be of great interest to image DNA in its natural unlabeled form in liquid with transmission electron microcopy (TEM). Here, we report our attempts to do so using graphene and SiN nanocapillaries and DNA-Au nanoconjugates that serve as a model system for liquid-cell electron microscopy of DNA. Using scanning TEM (STEM), we found that the imaging of nanoconjugates in SiN nanocapillaries resulted in aggregation of the Au markers as a consequence of beam-induce damage to DNA. Coating the SiN membranes with graphene helped significantly to mitigate the beam damage. STEM imaging of DNA-Au dimers was well possible in graphene liquid cells where we could observe the 3D motion of these constructs. Detecting contrast of the unlabeled dsDNA linker remained challenging though. These findings provide a strategy for future investigations of imaging nucleic acid nanostructures using liquid-cell electron microscopy.

This chapter is in preparation for publication as: Yoones Kabiri, Shimroy William, Cas de Mooij, Henny Zandbergen, Cees Dekker. Probing DNA nanostructures in graphene/SiN nanocapillaries with liquid-phase STEM

5.1. Introduction

Understanding how DNA behaves and interacts at the true nanoscale is of obvious great importance for many applications across biology. The ability to image DNA molecules with single-nanometer resolution thus deserves paramount attention. Among the microscopy techniques suitable to study specimens with adequate spatiotemporal resolution inside a bulk environment (i.e., not at a surface such as with scanning probe microscopy techniques), transmission electron microscopy (TEM) stands out as the leading choice. However, TEM is normally carried out on dry or frozen samples in vacuum, while exploiting the capabilities of TEM for imaging DNA in liquid are not trivial. A central challenge is the extreme vacuum environment in the microscope column that causes evaporation of any associated water in the specimen. Thin microfabricated liquid cells with windows based on silicon nitride and graphene have been proposed as they can withstand the high vacuum and at the same time encapsulate submicron thin water layers, thus creating a nanocuvette for examining the sample of interest [1–4].

Pioneering work on DNA imaging with TEM was carried out by Alivisatos et al [5] in graphene liquid cells (GLCs). They used DNA-Au nanoconjugates as a model system where a dimer of Au nanoparticles (NPs) helps localize a DNA molecule that interconnects them. The dynamics of such structures was captured in real time using regular TEM imaging. Interestingly, a counterintuitive and puzzling phenomenon that they observed was the excellent structural stability of the DNA linker under ionizing electron irradiation, which was orders of magnitude higher than commonly observed [6].Such damage mitigation behavior was later related to the catalytic properties of the graphene surface towards radiolysis products [7], and has been also observed for dry samples encapsulated by graphene [8, 9].

Many aspects of TEM imaging of DNA in liquid cells have yet remained unexplored. For example, to date, it is not known whether scanning TEM (STEM) provides advantages as an imaging mode to image unstained dsDNA or study the linker stability of these dimeric structures. It is of interest to study the effect of different nanocapillary confinements (i.e., silicon nitride vs graphene) on the structural stability of nanoconjugates with STEM imaging because TEM and STEM induce different radiation damage effects on the samples [10]. STEM provides several advantages over the normal TEM mode, such as a higher signal-to-noise ratio, a higher resolution for imaging nanoobjects in liquid, and greater choices for spectroscopy with nanometer resolution [1, 11–13]. Here, we explore the imaging of DNA-Au nanoconjugates in graphene and SiN liquid cells via in situ STEM.

We constructed a number of DNA-Au dimers that are suitable to be probed inside liquid EM nanocells. We first imaged these dimers using dry STEM, where the dsDNA linker was rendered visible and reliable statistics could be obtained on the particle distances. Subsequently, we introduced the dimers into three types of nanofluidic architectures: (i) SiN liquid cells, (ii) graphene-coated SiN liquid cells, and (iii) graphene liquid cells (GLCs). In situ STEM imaging on conventional SiN nanocells revealed that the radiation damage was very high, as evident from pronounced nanoparticle (NP) aggregation. In graphene-coated SiN nanocells, we observed some degree of radiation mitigation with a reduced amount of attachment of the dimers to the membrane. Finally, GLCs were found to provide a good platform to image the dimers, and we were able to observe the

dynamic movement of DNA-Au nanoconjugates with STEM imaging, as the dimers were stable under STEM illumination in GLCs. However, even in the GLCs, we were unable to realize good contrast for the unstained dsDNA linker that connects the Au NPs.

5.2. Results and Discussion

Assembly of DNA-Au dimers

We tailored the standard nanoconjugate assembly route [14–16] to optimize for the liquid cell studies, see Figure 5.1A. Method 1 is a prevailing route found in the literature [14–16] that involves functionalization of the Au NPs surface with a mixture of target ssDNA oligomers and other passivation agents such as short poly-T sequences that were added to prevent NP aggregation. Assembly of the dimers then occured by hybridization of target oligomers with complementary ssDNA overhangs on a bridging DNA linker. Alternatively, Au NPs with a single bound oligomer on their surface can be collected via high performance liquid chromatography (HPLC) and mixed to form the dimers [5]. In our work, we tried Method 1 but obtained better results with an alternative Method 2, which does not involve any functionalization of Au surfaces with ssDNA oligos. Here, dsDNA linkers of 42 or 90 base pairs length, either with 10 poly-T ssDNA overhangs or PEG spacer at 5' or 3' ends (see supporting information, SI), are initially hybridized in a separate reaction. Next, these constructs are mixed with Au NPs. In order to attach the DNA linkers to the surface of the NPs, thiol group at the ends of the ssDNA overhangs are activated by addition of TCEP (tris(2-carboxyethyl)phosphine) in the reaction mixture. Finally, monovalent salt (400mM NaCl) is added to overcome the electrostatic repulsion between Au NPs and the DNA linker, which facilitates the formation of the thiol-gold bond. Complete experimental details of the nanoconjugate assembly are provided in the SI.

The most significant difference among these two methods that is relevant for this study is the absence of oligomers on the surface of Au NPs in the final dimer structure in method 2, which prevents unwanted hydrophobic interactions of the ssDNA bases with the surfaces of the graphene and SiN nanocapillaries. In addition, method 2 features an easier and straightforward route for dimer fabrication, since any cumbersome Au functionalization is omitted. For example, Figure 5.1B depicts a typical issue during functionalization of Au NPs with oligos, which is aggregation of Au NPs before attachment of sufficient number of oligonucleotides on their surface. Figure 5.1C depicts another challenge in the sample preparation, when dimers are required to be purified from the unreacted Au NPs. We observed that dimers followed by method 1 form unclear or smeared band in the gel bands, which resulted in a low yield of dimer extraction from the gel. Due to these issues, we obtained quite irreproducible results with Method 1.

Characterization of DNA-Au dimers using STEM on dry samples

Although the main focus of this work is on the liquid-cell studies, we initially imaged the nanoconjugates dried out on a carbon support film to obtain a point of reference for measuring the particle distance in liquid. Previous works relied on TEM micrographs

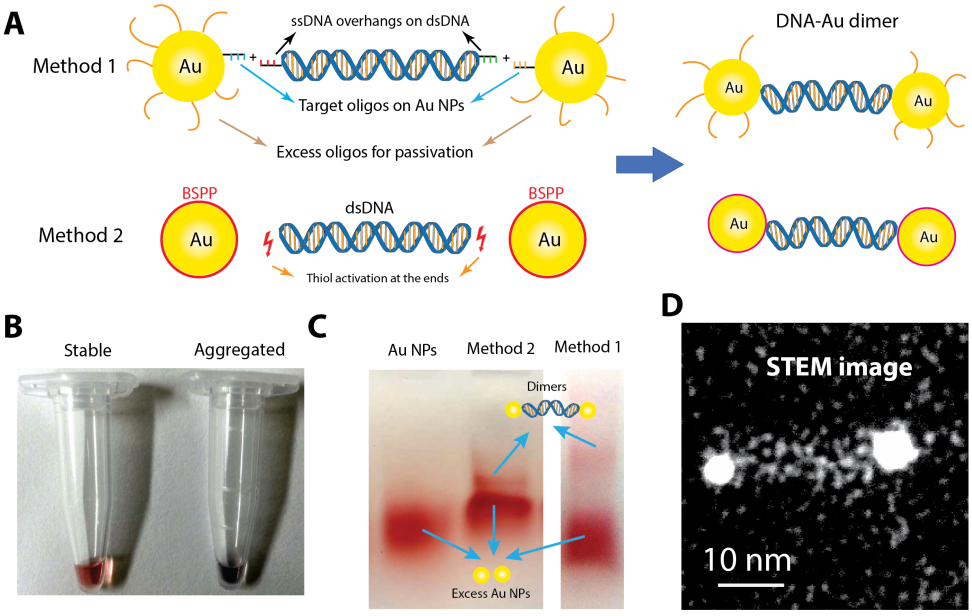

Figure 5.1: DNA-Au nanoconjugate synthesis. (A) Main strategies for assembling the DNA-Au nanoconjugates. Method 1 is the prevailing protocol in the literature, while method 2 is our customized protocol for in situ STEM liquid studies. (B) Image of stable and aggregated NPs/dimers in ambient light. (C) Gel bands of the reaction mixture depicting dimer and excess unreacted Au NPs. (D) Representative STEM image of a dimer NP stained with uranyl acetate.

for obtaining the particle distance without direct observation of the DNA linkers [17–19]. Note that normal TEM can only visualize positive or negative stained DNA nanostructures on carbon supports after class averaging [20, 21]. Here, however, we captured individual conformations of the nanoconjugates using STEM.

We were able to visualize the dsDNA linkers in single STEM acquisitions (Figure 5.2A), and based on that, we performed a statistical analysis of the particle distances in dry state (Figure 5.2B). Following Method 2, we obtained a very good dimer yield of 82% with a low formation of monomers (12%) and multimers (6%). The amount of multimers and aggregates in method 1 was higher, which was another reason why we resorted to the Method 2 assembly protocol. To measure the particle distances, dimer molecules were extracted from the STEM micrographs (N=100 for each construct) and the results are shown in Figure 5.2B. Note that we consider center-to-center measurements of Au NP at the both ends of the dimers as the particle distance throughout this manuscript.

The images in Figure 5.2B depicts noticeable variations of particle distances on carbon membranes in the dry state. Such flexible conformations of dsDNA are remarkable given the fact that these 42-90 bp (corresponding to a 14-30 nm length) are shorter than the 50nm persistence length of DNA. This has been reported before [14] and appears to be inherent to nanoconjugates with regions of ssDNA. It was also suggested before that the significant deviations from the worm-like chain model can be explained by a combination of surface curvature of the Au NPs and excluded volume effects[14]. Furthermore, Zhang et al. presented cryo-EM images of nanoconjugates with visible DNA linkers in an amorphous ice layer, showing a pronounced conformational heterogeneity of the DNA-Au dimer structures and measured particle distances that included abnormally small values, well below the persistence length of the bridging dsDNA [22]. Here, we obtain similar results with STEM imaging of the uranyl-stained dimers supported on carbon substrates. Finally, from comparing the 90 bp DNA linker constructs from Method 1, which are nicked, and from Method 2, which are non-nicked, we note that the presence of nicks in the DNA linker appears to have no major role on the observed end to end length, as both constructs yielded a similar 21 nm length.

STEM imaging of dimers in SiN liquid cells

Investigations of the dimers in the liquid state were carried out using the three types of liquid cell geometries shown in Figure 5.3. We first present our results on the STEM imaging of dimers in the SiN liquid cell nanocapillaries. We used a commercial liquid TEM holder from DENSsolutions (Delft, the Netherlands) with the nanocells that had nominally 50 nm SiN on each side. From our imaging data, we found that probing DNA-Au constructs was not well possible with the SiN liquid cells (Figure 5.4A-D). Initial experiments were done in solutions that contained the monovalent NaCl salts that were added during the assembly step. Here, electron beam-induced salt crystallization on SiN membranes quickly obscured the viewing windows (SI, Figure S5.1). To prevent this, the samples were thoroughly washed several times with TE buffer to remove residual salts, and all other in situ STEM experiments in this paper were done on the de-salted samples in order to avoid such crystallization effect.

Disappointingly, we observed that beam damage to the nanoconjugates was a significant problem (Figure 5.4B-D). Even with the lowest electron dose that was required

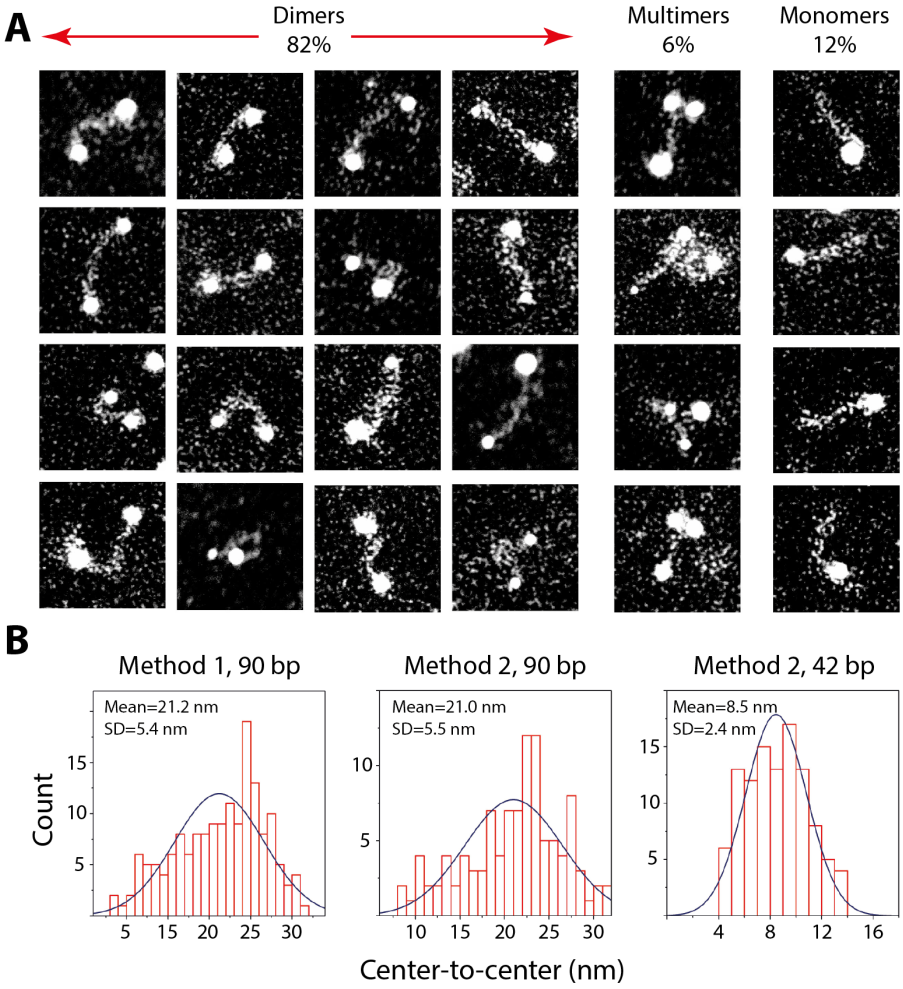

Figure 5.2: Conformations and statistics of dry DNA-Au nanoconjugates. (A) Representative STEM images of the uranyl stained dimers (Method 2, 90 bp) on a carbon support, which depicts a good yield of dimer formation in the population. A pronounced flexibility of the dsDNA linkers is observed. (B) Statistics of the NP center-to-center distances for three dimer constructs.

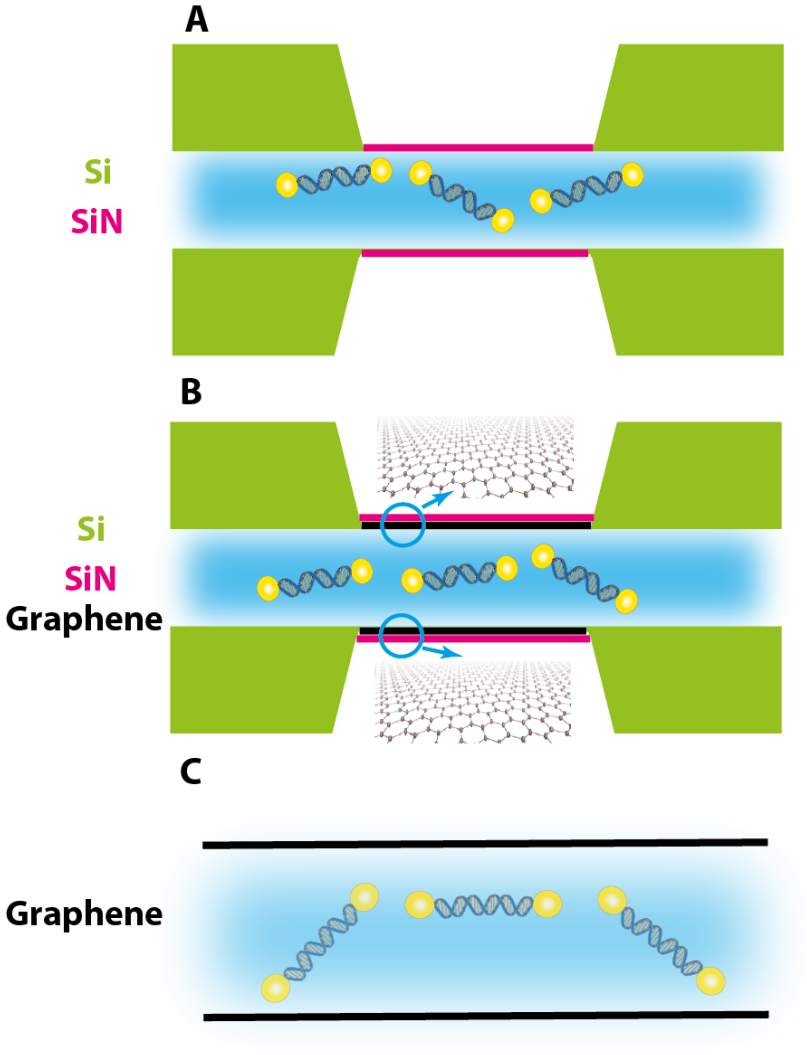

Figure 5.3: Schematics of liquid cell nanocapillaries based on (A) SiN, (B) graphene-coated SiN, and (C) graphene. The images are not drawn to scale.

to visualize the 5 nm Au NPs in the relatively thick SiN liquid cells, the dimers started to aggregate and form irregular clusters. In Figure 5.4B-D (see also SI movie S2), one can resolve individual 5 nm Au NPs (inside the dashed red rectangles), that attach to the clusters one particle at a time. Au duplets were never seen, which indicates that the damage to the dimer structure had already occurred in the bulk of the liquid cell. From a theoretically evaluation of the feasibility of obtaining contrast for 5 nm Au NPs in different liquid cells via Monte Carlo simulations of electron trajectories (SI, Figure S5.2), we deduced that contrast of individual Au NPs in SiN should be well possible for the designed 500 nm height. Indeed, NPs were visualized most clearly if they are close to the top SiN membrane, consistent with our Monte Carlo simulations (SI) and as reported [23, 24]. However, in the experiments, the SiN membranes were found to bulge up to an increased height of several microns after insertion into the microscope which affected the contrast of Au NPs adversely. To sum up, we conclude that SiN nanocapillaries are not suitable for STEM imaging of the hybrid DNA-Au NPs specimens due to pronounced electron beam damage.

To counteract the effect of beam damage, we incorporated graphene into SiN nanocells (Figure 5.4E). A monolayer of graphene was transferred to both top and bottom SiN nanocells using a PMMA transfer protocol [7]. The presence of graphene on SiN was confirmed via electron diffraction at different areas of the chip. An interesting observation in the STEM imaging experiments on these graphene-coated SiN nanocells was that, using similar doses as in Figure 5.4B-D, no NP attachment to the top membrane were seen, in direct contrast to the data for the SiN nanocells. This can be attributed to dissipation of accumulated charge on SiN by graphene, which prevents the well-known phenomenon of NP attachment to SiN membranes and their exceptionally slow movement that is orders of magnitude below what is expected in normal Brownian motion [23]. When, however, high electron doses were employed, we observed that NP clusters started to aggregate and attach to the top membrane (Figure 5.4F-H). The findings suggest that coating graphene on SiN nanocells is not an ideal strategy to capture the dynamics of dimers for EM imaging at high doses.

STEM imaging of dimers in GLCs

We continued our study with STEM imaging of dimers in GLCs that were prepared as in previous reports [5, 25, 26]. Excitingly, we found that GLCs provided a good platform for probing the dynamics of the DNA-Au nanoconjugates using STEM (Figure 5.5). What makes GLCs outstanding compared to (graphene coated) SiN nanocells is the confinement of a very thin layer of liquid between two atomically thin graphene sheets (Figure 5.5A), which enables both high-contrast STEM imaging of dimers as well as utilizing the maximum radiation mitigation due to high ratio of surface area of graphene per unit volume of liquid in the GLCs compared to SiN liquid cells. Figure 5.5B-D are still frames from an in situ STEM movie (SI movie S3) depicting the 3D motion of two 42bp dimer constructs in a GLC. Construct D1 exhibited a full 360-degree rotation in the 4 seconds displayed, while D2 drifted in a direction perpendicular to the viewing plane. The movement dynamics can be characterized as sluggish with convection motion (SI, Figure S5.3). Attachment of the dimers to the graphene was not observed, which indicates that our customized protocol was adequate to avoid unwanted dimer-graphene surface

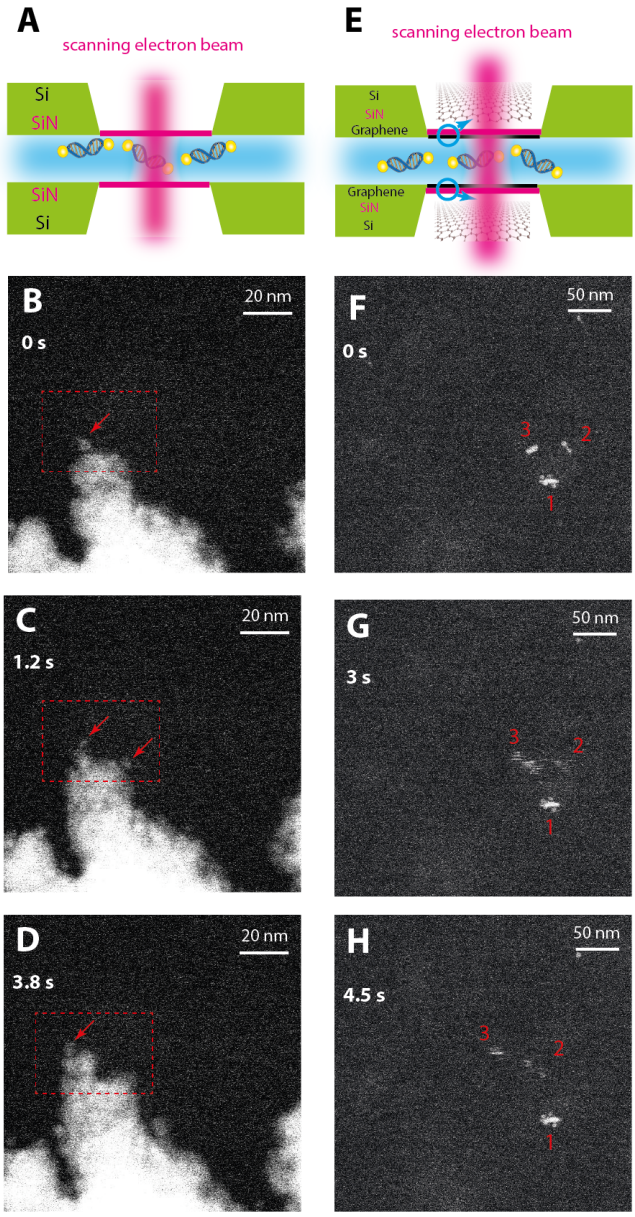

Figure 5.4: (A-D) Liquid-phase STEM imaging of DNA-Au nanoconjugates in SiN nanocells. (B-D) Still frames from an in situ movie (SI Video S1) depicting clustering and aggregation of the dimers due to beam-induce damage. (E-H) same as (A-D) but for dimers in graphene-coated SiN nanocells (SI Video S2). Three NP clusters are identified as 1, 2, and 3. Streaks in clusters 2 and 3 in G and H are due to fast movement beyond the STEM temporal resolution (250 ms in this experiment).

interactions. The high intensity observed in the liquid is likely related to presence of residual salts (SI, Figure S5.4).

An important point to note from these images was the structural stability of the nanoconjugates, as can be monitored from the sustained correlated motion of the Au NPs during continuous STEM imaging. Figure 5.5E shows the apparent particle distance between the two gold beads within each dimer, showing also the maximum observed separations (dashed green lines). Similar analyses for observing the maximum separation was carried out for different dimers (N=35) and the results are plotted in Figure 5.5F. An average NP center-to-center separation distance of 7.9 $\pm 1.3nm$ was observed, which is close to the value in dry state (8.5 $\pm 2.4nm$ in Figure 5.2B). This center-to-center separation value in liquid observed in the STEM micrographs is also in good agreement with measurements reported for the dimers containing the same 42 bp dsDNA bridge using normal TEM [5].

One of the aims of this study was to explore whether unstained DNA could be imaged inside the GLC nanocapillaries using STEM. Hence, we attempted to look for contrast of the bridge that connected the two Au particles. Unfortunately, we found that the DNA between the two gold nanoparticles is invisible, even in the extreme case when the dimers are trapped in the dried-out region of the GLC, i.e., encapsulated between two graphene layers without any water (Figure 5.5G and H). We performed different experiments with varying electron doses, different graphene pockets, and different graphene cleanness, but no good contrast resembling the DNA linker between the two Au NPs could be detected. Based on these STEM results, we thus conclude that the use of electron dyes or tagging the DNA with metallic nanoparticles is necessary to render it visible in GLCs, even when using STEM.

5.3. Conclusion

In this work, we showed single-molecule STEM images of DNA-Au dimers in various liquid-cell architectures and we observed their dynamics and structural stability. The low thickness of the encapsulated liquid layer between graphene membranes allowed visualization and tracking of the dynamics of Au NPs using low-dose STEM imaging, and the damage mitigation properties of graphene surface made it possible to shield the DNA linker against the harsh radiolysis products in the liquid medium. These two aspects provided by GLCs are quintessential for liquid-cell studies on nucleic acids using STEM. On the contrary, SiN nanofluidic cells, that are widely used for probing inorganic samples in materials science, were found to be not suitable to for these DNA-containing specimens as we encountered severe beam damage to the hybrid NPs in these types of nanocapillaries. The findings in this paper provide valuable guidelines for future research on the single-molecule biophysics of DNA using electron microscopy.

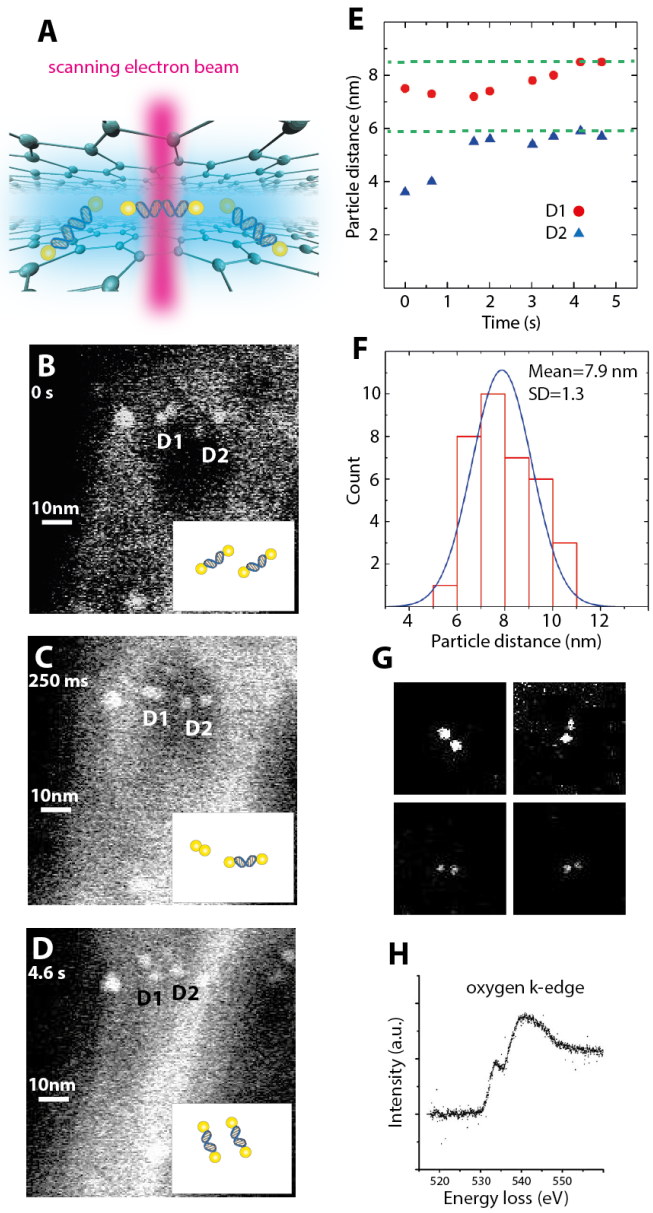

Figure 5.5: DNA-Au nanoconjugates can be probed with STEM in GLC nanocapillaries. (A) Schematics of GLC encapsulating dimers in thin layers of liquid. (B-D) Still frames from a movie (Video S3) depicting the 3D motion and structural stability of DNA-Au constructs in GLCs. Two dimers (named D1 and D2) are tracked with their orientations are sketched in the insets. (E) Particle distance traces for the D1 and D2 dimers in (B-D). The green dashed line shows the maximum measured distance. (F) Statistics of maximum particle distances in GLCs (N=35). (G) STEM images of trapped dimers encapsulated between two layers of graphene without liquid. Frame size is 47x47 nm2. (H) Electron energy loss spectroscopy (EELS) with detectable oxygen k-edge indicating the presence of water in GLCs.

5.4. Supporting Information

5.4.1. Dimer Assembly

Preparation of single-stranded DNA

We obtained ssDNA oligonucleotides from Integrated DNA Technologies Inc. (Coralville, IA). For method 1, the 3'ends of the target oligos are modified with dithiol disulfide linkers. The target 90 bp and 42 bp oligos used for method 2 were modified by dithiol disulfide linkers at the both ends. The ssDNA were resuspended in MilliQ distilled water, with a concentration of 100 µM. The sequences and corresponding information of all strands are listed in Table S5.1.

Gold nanoparticle functionalization with oligos

Two different sets of functionalized gold nanoparticles were made with the target oligos Ol-(N-1) and Ol-(N-2) (Table S5.1). Prior to functionalization, 50 µL of 100 µM dithiol-modified ssDNA strands were activated by addition of 5 µL TCEP (tris(2-carboxyethyl)-phosphine hydrochloride, Sigma-Aldrich, 0.5 M) by incubation for 1 hour. The sample was desalted using a Bio-Rad desalting column. Citrate-stabilized spherical gold nanoparticles were ordered from Nanopartz, Inc. (Loveland, US) with a nominal size of 5 nm and at a 6.6 µM concentration. 15.1 µL of the gold nanoparticle stock solution and 50 Milli-Q distilled water were added until a 1 mL reaction volume was reached. The eppendorf cup containing the sample was placed at a shaker at 800 RPM at 38 °C. Afterwards, the pH value was lowered to 2.5 by addition of a Trisodium-Citrate buffer, causing protonation of the oligo linkers [27]. Salt aging by stepwise addition of 10 µL of 5 M NaCl per minute, was done for 18 times for further enhancing the attachment and reducing the electrostatic repulsion between the AuNPs and the oligos [28]. The final solution contained 33 µL of 1 M NaOH, for neutralizing the pH value. The sample was cooled down to room temperature and washed (1X TE-buffer, 100 mM NaCl) 5 times using 50 kDa centrifugal column filters at 2500 RCF for 15 minutes, in order to remove the excess oligonucleotides and salts. The purified samples were stored at 4 °C.

Gold nanoparticle ligand exchange

For enhancing the stability of the nanoparticles, the weak citrate-capping was replaced by the more stable bis(p-sulfanatophenyl)phenyl-phosphine (BSPP) (Sigma-Aldrich, St. Louis, MO, US) ligand, through excessive addition of the ligand at a ratio of 500:1 between BSPP and the gold nanospheres. Afterwards, the solution was stirred at 600 RPM for approximately 6 hours and covered with aluminum foil. The solution was washed 5 times in 1X TE-buffer (pH 8) by centrifugation at 2500 RCF for 15 minutes (50 kDa filter). We estimated the final concentration of the stock solution from optical absorption spectrum measurements using the molar extinction coefficient (ε_{520} = 1.51x10^7 M^{-1} cm^{-1}), yielding a concentration of 4 µM.

Dimer assembly method 1

The two sets of functionalized gold nanoparticles (described above) were mixed in a 1:1 ratio prior to assembly, where the assembly buffer consisted of a 1X TE-buffer containing 100 mM NaCl. The dimers were formed by addition of athe DNA strand containing overhang parts which are complementary to the oligos attached to the gold. These DNA bridging strands were made by mixing oligo sequences (Ol-(N-3)), (Ol-(N-4)) and adding 50 mM NaCl. Afterwards, temperature annealing was done from 70 °C followed by slow cooling to room temperature at a rate of 1 °C/min. In order to prevent the formation of superstructures, the DNA bridging particles were added in a ratio of 1:5 DNA:Au NP and incubated overnight at room temperature. Purification of the formed nanoconjugate structures was carried out by gel electrophoresis at 7 V/cm with 0.5X TBE-buffer as running buffer. The 1% agarose gel was run for 1 hour until a band was formed. Subsequently, the distinct bands were cut out, followed by the 'freeze and squeeze' protocol for extraction of the conjugates [4]. Finally, the samples were washed in 1X TE-buffer (pH 8) and stored at 4 °C.

Dimer assembly method 2

The complementary ssDNA strands were ordered from Integrated DNA Technologies Inc. (Coralville, IA). The 5'-ends were modified with poly-T spacers (5T) and a disulfide group. To generate the corresponding dsDNA structures, temperature annealing from 50 °C to room temperature was carried out at a slow rate of 1 °C/min. The particles were mixed with the BSPP coated gold nanospheres in a ratio of 1:5. In order to induce dimer formation, TCEP was added to the solution (at a ratio of 500:1 between the TCEP particles and dsDNA structures) as a reducing agent and 400 mM NaCl was added to overcome the electrostatic repulsion between the negatively charged nanospheres and the dsDNA particles. Subsequently, the Eppendorf cup was enveloped with aluminum foil, followed by overnight incubation at room temperature. Purification by gel electrophoresis was carried out using an 3% agarose gel, a 1X TBE-buffer at 10 V/cm for 45 minutes, yielding a clear separation between the bulk nanospheres and the formed DNA-Au nanoconjugate structures. Subsequently, the distinct band was cut out and dimers were extracted by the freeze and squeeze protocol. The samples were washed in 1X TE-buffer (pH 8) and stored at 4 °C.

Name	Number base pairs	Sequence	Spacer
Ol-(N-1)	22	5'-GGTTCTCGGTCGCTTCATACAC-3'–Spacer – Dithiol	PEG
Ol-(N-2)	22	5'-GGGACGGCCAAAAATGCTTTGG-3'–Spacer – Dithiol	PEG
Ol-(N-3)	68	5'-GTGTATGAAGCGACCGAGAAC CTCAGCTGTGAAATTGTTATCCGCT CACAATTCCACACAACATACGA-3'	-
Ol-(N-4)	68	5'-CCAAAGCATTTTTGGCCGTCCC TCGTATGTTGTGTGGAATTGTGAGC GGATAACAATTTCACAGCTGA-3'	-
Ol-(B-1)	90	5'-GTGTATGAAGCGACCGAGAACCTCA GCTGTGAAATTGTTATCCGCTCACAA TTCCACACAACATACGAGGTTCTCGG TCGCTTCATACAC-3'–Spacer–Dithiol	Poly-T (10T)
Ol-(B-2)	90	5'-CCAAAGCATTTTTGGCCGTCCCT CGTATGTTGTGTGGAATTGTGAGCGGA TAACAATTTCACAGCTGAGGGACGGCC AAAAATGCTTTGG-3'–Spacer–Dithiol	Poly-T (10T)
Ol-(B-3)	42	Dithiol–Spacer–5'-GATAACAATCTCACAGCTGAGGC TCTCGGTCGCTTCATACAC-3'	Poly-T (10T)
Ol-(B-4)	42	Dithiol–Spacer–5'-GTGTA TGAAGCGACCGAGAGCCTCAGCT GTGAGATTGTTATC-3'	Poly-T (10T)

Table S5.1: Oligo information for the constructs in the main text

5.4.2. Preparation of SiN and graphene-coated SiN nanocapillaries

A commercial liquid TEM holder from DENSsolutions (Delft, The Netherlands) was used for both the SiN and graphene-coated experiments. The SiN chips used in conjugation with this holder were also commercially available and provided by the same company. The SiN chips were cleaned thoroughly by stepwise immersion in acetone, ethanol, and isopropanol respectively to remove the protective polymer coating. For bare SiN nanocapillary experiments (Figure 5.4A-D), shortly before the nanocell assembly, the chips are treated with oxygen plasma to render them hydrophilic. One chip was placed at the tip of the holder and 1 uLit of the dimer sample was applied on top of the chip, followed by immediate sealing with the second SiN chip on top. The same procedure was used for assembling the graphene-coated (PMMA transfer) SiN nanocapillaries but no oxygen plasma was applied, in order to protect the graphene membrane. While the liquid holder featured a liquid flow capability, we used the sealed option (no flow). It has been shown that flow inside the liquid cell has virtually no impact on the radiolysis since the harsh radicals saturate the medium immediately after the e-beam irradiation due to their fast diffusion coefficient, which cannot be compensated by the negligible flow rate offered by the holder [6].

5.4.3. STEM imaging

A post-specimen aberration-corrected Titan microscope (ThermoFischer Scientific) was used in STEM mode at 300 kV acceleration voltage. Cs was tuned to zero for the lowest delocalization, while chromatic aberration (Cc) was 3 mm. Lower operating voltage below 300 kV was not pursued because it induces higher radiolysis due to increased inelastic cross-section, which is detrimental for liquid cell imaging in terms of damage and bubble formation. Collection of the STEM frames was done via a high-angle annular dark-field (HAADF) detector at camera length of 28.5 cm for dominant mass-thickness Z-contrast imaging. After initial alignment for liquid cell imaging, the focal point was adjusted to the top membrane (for SiN nanocapillaries) for the highest signal to noise ratio (cf. the Monte Carlo simulations). Electron doses were different depending on the experiments. For th SiN liquid cells, our effort was to visualize the 5 nm Au NPs on top membrane with the lowest electron dose possible in order to minimize the radiation damage. Regardless of the doses used, however, what followed was huge NP aggregation in the SiN nanocells, as a direct consequence of structural damage to the DNA linker and NP stabilizing shell. For the GLCs, we tuned the screen current by controlling the spot size. The lowest screen current for that purpose was achieved at spot size 7 with a beam current of 50 pA. Other parameters were 50 um condenser aperture, 10 mrad convergence angle, and a temporal resolution between 60 ms up to 250 ms depending on dynamics of the NPs.

5.4.4. Beam-induced salt crystallization

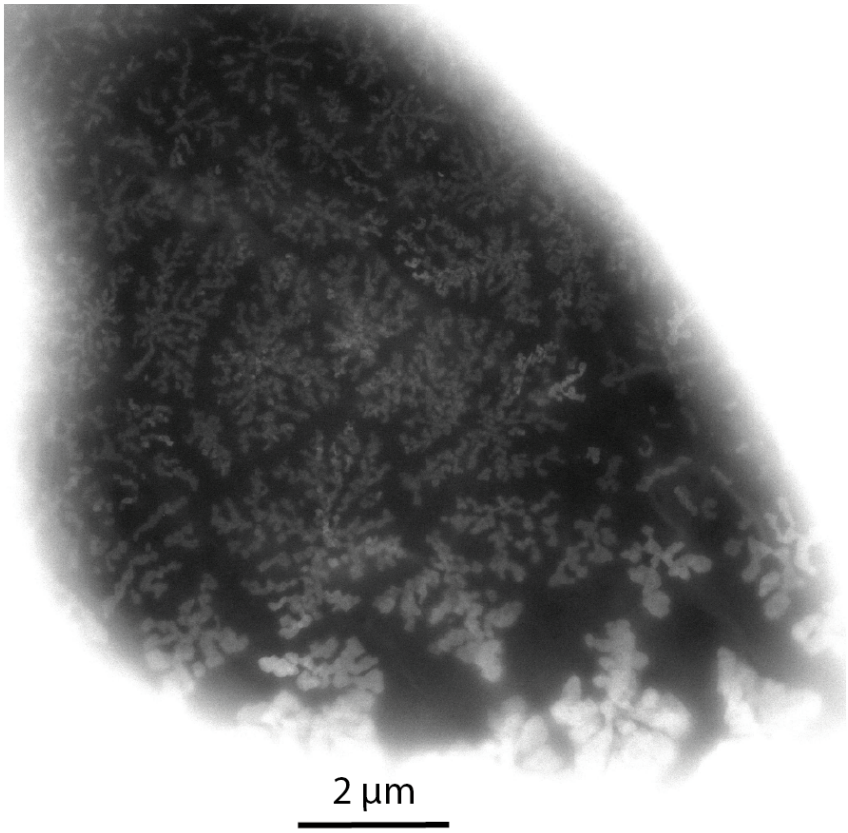

Figure S5.1: Beam-induced salt crystallization in SiN nanocells during STEM imaging. The image shows salt crystal formed from residual salts that were added during the assembly step. All other in situ STEM experiments were done on the desalted samples in order to avoid this crystallization effect.

5.4.5. Monte Carlo simulation of electron trajectories in SiN and graphene liquid cells

We simulated the STEM image contrast of Au NPs in SiN and graphene nanocapillaries via Monte Carlo simulation package Casino V3.3 (Figure S5.2). Liquid cells were created in the 3D geometry editor similar to the insets of Figure S5.2C-D. To simulate the closest condition to our Titan instrument, the following parameters were used. The dwell time was set 320 ns resulting in 12 frames per second. The beam current was set to 500 pA, resulting in 1000 electrons per point. In order to achieve a high lateral resolution, the scan point spacing was set to 0.25 Å. The beam diameter was set to 2.0 Å at the focal plane and was focused with a semi-angle α of 10 mrad, which is the optimum angle for STEM. The simulated detector was a HAADF with the collection semi angles of 94 to 600 mrad. Its quantum efficiency was assumed to be 100%. The option to generate a different number of electrons per scan point, shot noise, was used to create a more realistic image. These parameters ensured low-dose imaging with reasonable temporal and spatial resolution. To validate our results, we simulated other test cases (liquid cells with certain Au NP diameters) as discussed in the literature and we obtained similar results. Simulation results (Figure S5.2C-D) revealed that the highest contrast and resolution was obtained when the nanoparticles are closer to the top membrane in both SiN and GLCs. Moreover, GLCs depicted a higher resolution and contrast due to the atomic thickness of graphene membrane, with a negligible electron scattering strength (leading to reduced background noise). Note that the Monte Carlo simulations depict only scattering events and do not address electron damage effects.

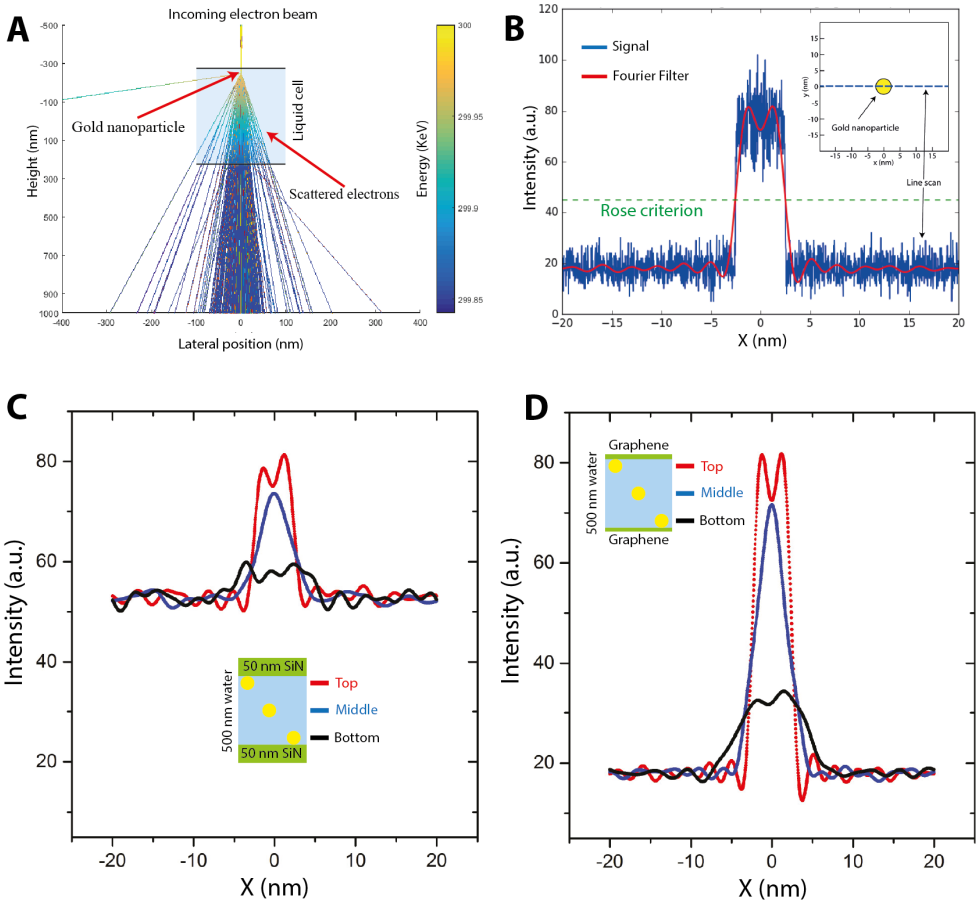

Figure S5.2: (A) Electron scattering trajectories in a liquid cell with a gold nanoparticle situated beneath the top membrane. (B) A representative line-profile intensity of the HAADF detector and its Fourier filter. The Rose criterion is the threshold for the visibility of an object given a background noise. (C) Summary of simulation results for Au nanoparticles inside a SiN liquid cell. The inset shows the positions of the Au NPs in the liquid cell and their corresponding color-coded graphs (D) same as (C) but for a GLC. We observe a higher signal to noise ratio for the GLC and hence a better visibility of the Au NPs.

5.4.6. Movement dynamics of DNA-Au dimers

The diffusional dynamics of the dimers are shown in Figure S5.3. We developed a custom-made Matlab script for particle tracking and statistical analysis of the STEM frames. The left column of Figure S5.3 shows the trajectory of the center-of-mass of the three 42 bp dimers. We observe that the dimers move in a convection type of movement with stagnation when the liquid layer dries at the end of STEM investigations. This drift is most likely due to a leakage in the liquid cell. To correct for it, the drift velocity was estimated by:

$$< \vec{v}_d >= \int_0^T \frac{\vec{r}(t+\delta t) - \vec{r}(t-\delta t)}{2\delta t} dt \tag{5.1}$$

for each trajectory, where $\vec{r}$ is the position vector coordinate and δt=63ms corresponds to the time resolution of the measurements. Subtraction of the drift velocity from the dimer coordinates yielded the trajectories shown in the right column of Figure S5.3. The diffusivity was determined by computing the mean squared displacement (MSD = $< |\vec{r}(t) - \vec{r}(0)|^2 >$) of the ensemble averaged of the corrected trajectories with the corresponding position vector $\vec{r}(t)$. This resulted in a linear relation between the MSD and diffusion time t, which indicates Brownian motion. Abnormal sluggish behavior has been reported by several other groups regarding the slow Brownian motion of dimer structures [5] and nanocrystals [29, 30] due to sample-substrate interaction.

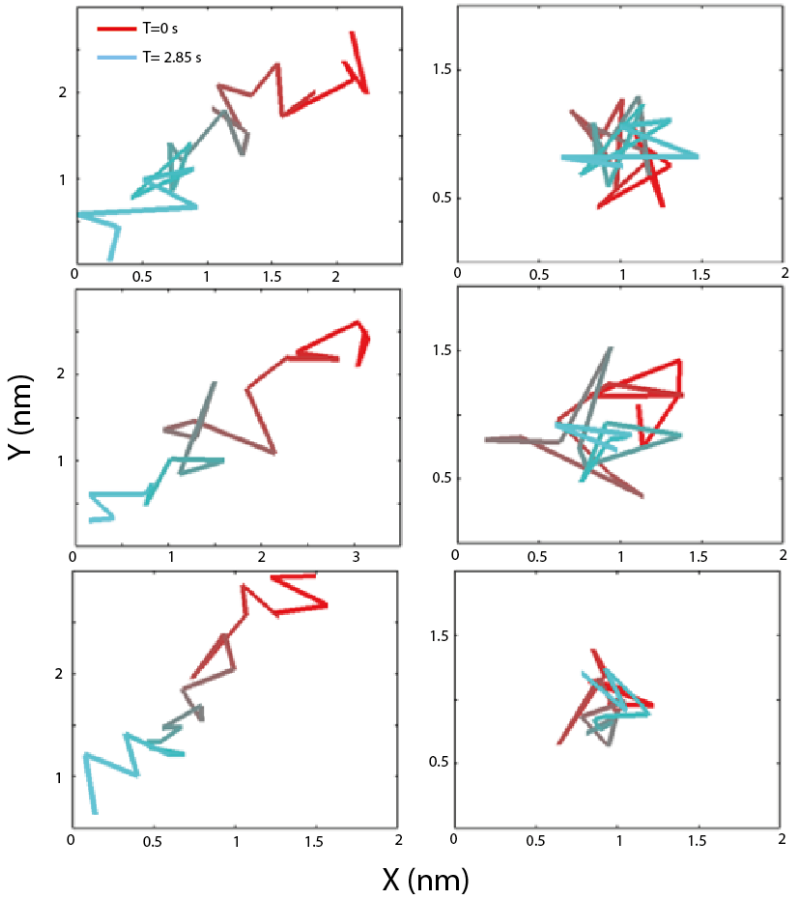

Figure S5.3: Movement dynamics of three dimers (each row) with 42 bp dsDNA in GLCs. The left column shows the trajectory of the center-of-mass, while the right column is the trajectory after drift correction.

5.4.7. Energy-dispersive x-ray spectroscopy (EDS) on GLCs

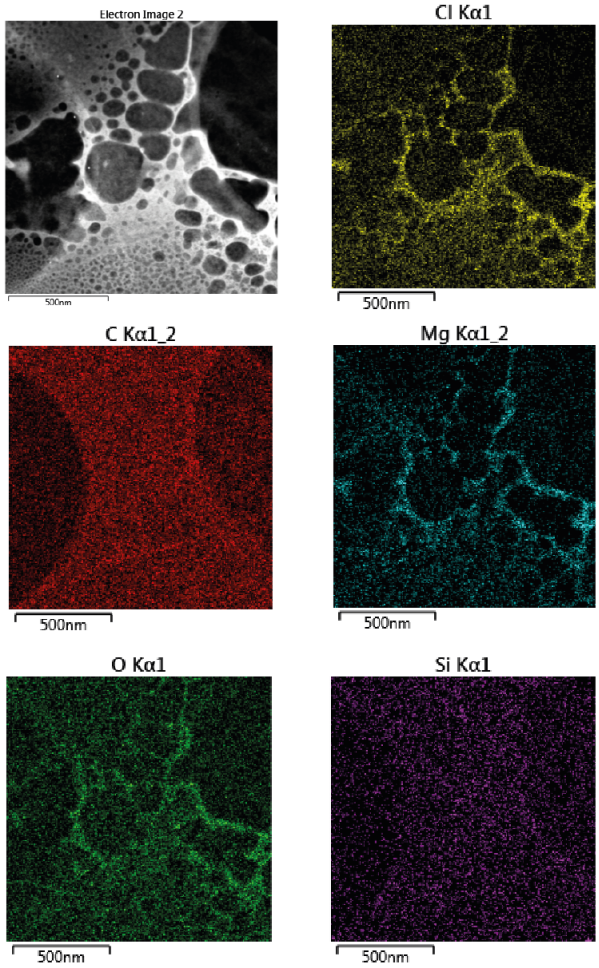

Figure S5.4: STEM EDS map of GLCs. Bubbles are formed during high electron exposure needed for the EDS spectroscopy. The oxygen map confirms the presence of water while mixed with the hygroscopic salts.

References

[1] C. Wang, Q. Qiao, T. Shokuhfar, and R. F. Klie, *High-resolution electron microscopy and spectroscopy of ferritin in biocompatible graphene liquid cells and graphene sandwiches,* Advanced Materials **26**, 3410 (2014).

[2] C. Wadell, S. Inagaki, T. Nakamura, J. Shi, Y. Nakamura, and T. Sannomiya, *Nanocuvette: A functional ultrathin liquid container for transmission electron microscopy,* ACS nano **11**, 1264 (2017).

[3] N. De Jonge and F. M. Ross, *Electron microscopy of specimens in liquid,* Nature nanotechnology **6**, 695 (2011).

[4] F. M. Ross, *Opportunities and challenges in liquid cell electron microscopy,* Science **350**, aaa9886 (2015).

[5] Q. Chen, J. M. Smith, J. Park, K. Kim, D. Ho, H. I. Rasool, A. Zettl, and A. P. Alivisatos, *3d motion of dna-au nanoconjugates in graphene liquid cell electron microscopy,* Nano letters **13**, 4556 (2013).

[6] N. M. Schneider, M. M. Norton, B. J. Mendel, J. M. Grogan, F. M. Ross, and H. H. Bau, *Electron–water interactions and implications for liquid cell electron microscopy,* The Journal of Physical Chemistry C **118**, 22373 (2014).

[7] H. Cho, M. R. Jones, S. C. Nguyen, M. R. Hauwiller, A. Zettl, and A. P. Alivisatos, *The use of graphene and its derivatives for liquid-phase transmission electron microscopy of radiation-sensitive specimens,* Nano letters **17**, 414 (2016).

[8] G. Algara-Siller, S. Kurasch, M. Sedighi, O. Lehtinen, and U. Kaiser, *The pristine atomic structure of mos2 monolayer protected from electron radiation damage by graphene,* Applied Physics Letters **103**, 203107 (2013).

[9] R. Zan, Q. M. Ramasse, R. Jalil, T. Georgiou, U. Bangert, and K. S. Novoselov, *Control of radiation damage in mos2 by graphene encapsulation,* ACS nano **7**, 10167 (2013).

[10] R. Egerton, *Radiation damage to organic and inorganic specimens in the tem,* Micron (2019).

[11] D. J. Kelly, M. Zhou, N. Clark, M. J. Hamer, E. A. Lewis, A. M. Rakowski, S. J. Haigh, and R. V. Gorbachev, *Nanometer resolution elemental mapping in graphene-based tem liquid cells,* Nano letters **18**, 1168 (2018).

[12] J. R. Jokisaari, J. A. Hachtel, X. Hu, A. Mukherjee, C. Wang, A. Konecna, T. C. Lovejoy, N. Dellby, J. Aizpurua, O. L. Krivanek, *et al.*, *Vibrational spectroscopy of water with high spatial resolution,* Advanced Materials **30**, 1802702 (2018).

[13] C. Wang, T. Shokuhfar, and R. F. Klie, *Precise in situ modulation of local liquid chemistry via electron irradiation in nanoreactors based on graphene liquid cells,* Advanced Materials **28**, 7716 (2016).

[14] C. Chi, F. Vargas-Lara, A. V. Tkachenko, F. W. Starr, and O. Gang, *Internal structure of nanoparticle dimers linked by dna,* Acs Nano **6**, 6793 (2012).

[15] S. J. Hurst, A. K. Lytton-Jean, and C. A. Mirkin, *Maximizing dna loading on a range of gold nanoparticle sizes,* Analytical chemistry **78**, 8313 (2006).

[16] F. N. Gür, F. W. Schwarz, J. Ye, S. Diez, and T. L. Schmidt, *Toward self-assembled plasmonic devices: High-yield arrangement of gold nanoparticles on dna origami templates,* ACS nano **10**, 5374 (2016).

[17] A. J. Mastroianni, D. A. Sivak, P. L. Geissler, and A. P. Alivisatos, *Probing the conformational distributions of subpersistence length dna,* Biophysical journal **97**, 1408 (2009).

[18] A. P. Alivisatos, K. P. Johnsson, X. Peng, T. E. Wilson, C. J. Loweth, M. P. Bruchez Jr, and P. G. Schultz, *Organization of 'nanocrystal molecules' using dna,* Nature **382**, 609 (1996).

[19] C. J. Loweth, W. B. Caldwell, X. Peng, A. P. Alivisatos, and P. G. Schultz, *Dna-based assembly of gold nanocrystals,* Angewandte Chemie International Edition **38**, 1808 (1999).

[20] Y. Kabiri, A. N. Ananth, J. van der Torre, A. Katan, J.-Y. Hong, S. Malladi, J. Kong, H. Zandbergen, and C. Dekker, *Distortion of dna origami on graphene imaged with advanced tem techniques,* small **13**, 1700876 (2017).

[21] Y. Kabiri, A. Angelin, I. Ahmed, H. Mutlu, J. Bauer, C. M. Niemeyer, H. Zandbergen, and C. Dekker, *Intercalating electron dyes for tem visualization of dna at the single-molecule level,* ChemBioChem **20**, 822 (2019).

[22] L. Zhang, D. Lei, J. M. Smith, M. Zhang, H. Tong, X. Zhang, Z. Lu, J. Liu, A. P. Alivisatos, and G. Ren, *Three-dimensional structural dynamics and fluctuations of dna-nanogold conjugates by individual-particle electron tomography,* Nature communications **7**, 11083 (2016).

[23] A. Verch, M. Pfaff, and N. de Jonge, *Exceptionally slow movement of gold nanoparticles at a solid/liquid interface investigated by scanning transmission electron microscopy,* Langmuir **31**, 6956 (2015).

[24] N. de Jonge, N. Poirier-Demers, H. Demers, D. B. Peckys, and D. Drouin, *Nanometer-resolution electron microscopy through micrometers-thick water layers,* Ultramicroscopy **110**, 1114 (2010).

[25] G. Algara-Siller, O. Lehtinen, F. Wang, R. Nair, U. Kaiser, H. Wu, A. Geim, and I. Grigorieva, *Square ice in graphene nanocapillaries,* Nature **519**, 443 (2015).

[26] M. Textor and N. de Jonge, *Strategies for preparing graphene liquid cells for transmission electron microscopy,* Nano Letters **18**, 3313 (2018).

[27] X. Zhang, M. R. Servos, and J. Liu, *Instantaneous and quantitative functionalization of gold nanoparticles with thiolated dna using a ph-assisted and surfactant-free route,* Journal of the American Chemical Society **134**, 7266 (2012).

[28] L. M. Demers, C. A. Mirkin, R. C. Mucic, R. A. Reynolds, R. L. Letsinger, R. Elghanian, and G. Viswanadham, *A fluorescence-based method for determining the surface coverage and hybridization efficiency of thiol-capped oligonucleotides bound to gold thin films and nanoparticles,* Analytical chemistry **72**, 5535 (2000).

[29] J. M. Yuk, J. Park, P. Ercius, K. Kim, D. J. Hellebusch, M. F. Crommie, J. Y. Lee, A. Zettl, and A. P. Alivisatos, *High-resolution em of colloidal nanocrystal growth using graphene liquid cells,* Science **336**, 61 (2012).

[30] E. White, M. Mecklenburg, B. Shevitski, S. Singer, and B. Regan, *Charged nanoparticle dynamics in water induced by scanning transmission electron microscopy,* Langmuir **28**, 3695 (2012).

Summary

The low contrast of biomolecules in TEM has been a great obstacle for their structure determination and hence to the understanding of their structure-function relation. Historically, single DNA strands remained one the most difficult classes of biomolecular specimens to image, due to low electron scattering strength of its constituent elements. The common practice was then to image them either when freely suspended (without any support) or shadow image them with negative staining technique. Those remedies are limited in terms of applicability to different DNA nanostructures as well as pose difficulties in sample preparation. For example, making the 2D DNA nanostructures free-standing would not be a viable solution for imaging them. This thesis provides a general study to tackle the challenges in imaging nucleic acids with TEM.

In **chapter 2**, we investigate the suitability of single-layer graphene membranes for improving the imaging of DNA. The prevailing problem in the early days of electron microscopy was the lack of a conductive and thin sample support. The reduced thickness of graphene (3 Angstrom) would reduce the substrate interference and consequently increases the contrast of DNA nanostructures. We probed single-layer DNA origami nanostructures on graphene under different imaging conditions. We observed that the origami plates on graphene can be imaged with scanning TEM and dark-field technique, without a need for labeling, though the origami plates were seen to be severely distorted. Our complementary AFM and TEM analyses showed that the hydrophobic interaction between graphene and DNA plays a crucial role in the observed distortion, and functionalization of graphene with 1-PCA molecules reduced the hydrophobic interaction and hence caused less distortion to the origami nanostructures. Although single sheets of graphene are only about 3-4 Angstrom thick, we could not obtain images of unstained single-DNA helices, even when utilizing the STEM or dark-field mode of the microscope.

We proceeded to make DNA visible using a special intercalating molecule that is introduced in **chapter 3**. One question in biochemistry was whether it would be possible to utilize intercalation binding for single-molecule visualization of DNA with electron microscopy. We designed a new intercalating molecule, i.e., bis-acridine uranyl (BAU), which features two intercalating subunits of acridine that are tethered to a salophen ligand. The salophen ligand contains one atom of heavy uranium element in its structure that acts as an electron scattering agent. We characterized the synthesized BAU compound with various techniques such as NMR, gel electrophoresis, and mass spectroscopy to verify the BAU design as well as its DNA binding properties. The attachment of BAU to DNA through intercalation resulted in accumulation of the heavy uranium element around the DNA and hence led to pronounced electron scattering in TEM (positive staining). We observed that BAU can indeed provide good contrast for DNA in TEM. We could resolve, even at the single-molecule level, DNA strands attached to the 2D DNA origami plates using the STEM technique. The use of STEM in conjugation with DNA origami is a powerful methodology that enables probing other chemicals with a pur-

ported affinity towards DNA, such as OsO4 and Cisplatin. We found that BAU provides a good contrast efficiency, close to that of the prevailing uranyl acetate which is a backbone binder, whereas OsO4 and Cisplatin displayed no discernable contrast.

In **chapter 4**, we address the low contrast of weak phase objects such as DNA nanostructures using modifications in electron optics. For proteins, the common practice in single particle analysis in Cryo-EM is to gather thousands of noisy images (in normal TEM mode) and class average them in order to increase the contrast and consequently determine their structures. However, while this technique is applicable to globular molecules, biomolecules such as 2D DNA nanostructures are invisible in TEM and hence the class averaging does not provide a solution. Not only the low scattering of DNA, but also the theoretical limitations in electron optics results in an overall invisibility of the biomolecules in TEM. To revive the low-frequency part of the frequency spectrum (corresponding to large-scale spatial features in real space) in CTF, we recruited the latest volta-potential phase plate (VPP). VPP induces a $\pi/2$ phase shift and changes the CTF from a since-type to a cosine-type. We find that DNA origami nanoplates can be imaged with good contrast in single frame acquisitions using VPP at high acceleration voltages (200 kV). Instead of using VPP at high kV, we also probed the origami samples at low-voltages (20 kV) using a Cs+Cc corrected microscope (sub-angstrom low voltage electron microscopy or SALVE) and again observed good contrast. These results extend the use of aberration-corrected low-voltage microscopy to structural biology. The in-focus phase contrast methods discussed in this chapter are promising for studying weak phase biomolecules that are not visible through conventional defocus-based TEM.

Understanding the structural stability of DNA in its native aqueous state is the main focus of **chapter 5**. One of the key questions was whether unstained DNA can be imaged inside liquid with electron microscopy, and what would be the effects of the liquid cell architecture (e.g. SiN and graphene liquid cells) and imaging mode (e.g. STEM and TEM) on its structural stability. We utilize a special DNA nanostructure for this purpose, namely DNA-Au nanoconjugates. These nanoconjugates are a class of hybrid materials that constitute two small nanoparticles (each 5 nm in diameter for our case) that are tethered together via a dsDNA molecule. Since the Au particles act as good contrast markers, we could track the nanoconjugates and pinpoint the exact location of DNA in between the particles to see if we can obtain any contrast on the unstained DNA. We found, however, that this is not possible even when using STEM which has higher signal-to-noise than TEM, and even when these nanoconjugates were confined in very thin graphene liquid pockets. Furthermore, SiN liquid cells were found to be not the ideal platform for in situ liquid studies on DNA in terms of resolution and electron beam damage mitigation, whereas graphene liquid cells presented an advantage.

Samenvatting

Het lage contrast dat gegeneerd wordt door biomoleculen in TEM is een groot obstakel voor het in beeld brengen van deze structuren, en daarmee voor het begrijpen van de onderlinge structuur-functie relatie van deze moleculen. Historisch gezien behoren enkelvoudige DNA ketens tot een van de moeilijkst in beeld te brengen biomoleculaire structuren, door hun lage elektronen-verstrooiing, wat wordt veroorzaakt door hun atomaire samenstelling. De beste methode voor het in beeld brengen van deze structuren betrof het vrij vrij ophangen van DNA of het maken van een schaduwafbeelding door een negatieve-markeertechniek. Deze oplossingen zijn erg gelimiteerd in termen van toepasbaarheid voor verschillende DNA nanostructuren waarbij het ook lastig is om de monsters voor te bereiden. Het is bijvoorbeeld zeer lastig om de 2D nanostructuren vrijstaand te maken en daardoor nauwelijks mogelijk om deze structuren in beeld te brengen zonder nadere markering. In dit proefschrift zal een meer algemene studie worden gepresenteerd voor het visualiseren van DNA met TEM.

In **hoofdstuk 2**, wordt de toepasbaarheid van grafeenmembranen voor het in beeld brengen van het DNA onderzocht. Het dominante probleem in het verleden met betrekking tot elektronenmicroscopie was het gebrek aan elektrisch geleidend en voldoende dun materiaal, voor het ondersteunen van het biologische preparaat. Door de interferentie van het fase-contrast tussen de substraathouder) en het monster-afbeelding, zal de gereduceerde dikte van het grafeen (3 Ångström) deze interferentie verminderen en daarmee het contrast van DNA nanostructuren doen toenemen. Wij hebben het afbeelden van enkellaags DNA origami nanostructuren onderzocht met het grafeen onder verschillende omstandigheden. Onze observaties laten zien dat origami platen op grafeen in beeld kunnen worden gebracht met STEM en donkerveldtechnieken, zonder dat het DNA gemarkeerd hoeft te worden, hoewel de origami platen sterk vervormd zijn. Onze complementaire AFM en TEM analyses laten zien dat de hydrofobe interactie tussen grafeen en DNA een belangrijke rol speelt in de vervorming, en het functionaliseren van grafeen met 1-PCA moleculen verzwakt de hydrofobe interactie en vermindert daarbij de vervorming van de origami nanostructuren. Het is het niet gelukt om afbeeldingen te verkrijgen van ongemarkeerde enkele DNA-helixstructuren, verbonden aan de origami platen, zelfs met STEM of de donkere-veldstand van de microscoop.

Ons onderzoek vervolgde met het visualiseren van DNA door gebruik te maken van een speciaal intercalerend molecuul dat wordt geïntroduceerd in **hoofdstuk 3**. Een vraag binnen de biochemie is of het mogelijk is om gebruik te maken van een intercalerende binding voor enkel-molecuul visualisatie van DNA door middel van elektronenmicroscopie. We hebben een nieuw intercalerend molecuul ontworpen, bis-acredine uranyl (BAU), dat beschikt over twee intercalerende subeenheden van acredine die gebonden zijn aan een salophen-ligand. Het salophen-ligand beschikt onder anderen over een atoom van het zware uranium element, wat goed werkt als middel voor de verstrooiing van elektronen. We karakteriseren de gesynthetiseerde BAU samenstelling met ver-

schillende technieken, zoals NMR, gelelektroforese en massaspectroscopie om zowel het ontwerp van de BAU als de DNA-bindende eigenschappen van deze stof vast te stellen. De binding tussen de BAU met het DNA door intercalatie resulteert in een accumulatie van het zware Uranium element rond het DNA en leidt tot de verstrooiing van elektronen in TEM (positieve markering). We observeren dat BAU voor een goed contrast voor het DNA in de TEM kan zorgen. We waren in staat om zelfs op het niveau van een enkel molecuul de DNA strengen, verbonden aan de 2D DNA origami platen, te onderscheiden met behulp van de STEM techniek. Het gebruik van STEM in samenwerking met DNA origami is een krachtige methodologie die het mogelijk maakt om ook andere chemicaliën te onderzoeken met een affiniteit voor DNA, zoals OsO4 en Cisplatin. We vonden dat de BAU de beste efficiëntie biedt, vergelijkbaar met de gangbare Uranylacetaat binder voor de fosfaatruggengraat, terwijl OsO4 en Cisplatin geen waarneembaar contrast lieten zien.

In **hoofdstuk 4** bespreken we het probleem betreffende het lage contrast van zwakke fase structuren (zoals DNA nanostructuren) waarbij we gebruik maken van modificaties in de elektronenoptica, Voor eiwitten is de gangbare methode voor enkele-deeltjes analyse in Cryo-EM het vergaren van duizenden afbeeldingen die veelal ruis bevatten, en deze in verschillende klassen in te delen om daar het gemiddelde van te verkrijgen. Dit gebeurt om het contrast te verhogen en daarmee de structuren duidelijk vast te stellen. De techniek is voornamelijk toepaspaar op veel moleculen, maar sommige biomoleculen, zoals 2D DNA nanostructuren, zijn volledig onzichtbaar in TEM waardoor een klassegemiddelde bepalen onmogelijk is. Niet alleen het lage verstrooiingsgehalte van DNA, maar ook theoretische limieten in elektronenoptica, verklaard aan de hand van de contrast overdracht functie (CTF), zorgen hiervoor, en verklaren waarom de lage-frequentie componenten van de uitgaande golf vrijwel volledig onderdrukt blijven in het beeldvlak van de microscoop. Dit resulteert in een algehele onzichtbaarheid van de biomoleculen in TEM. Om het laag-frequentie gedeelte van het frequentiespectrum (wat overeen komt met grotere spatiele kenmerken in de echte ruimte) te herstellen in CTF, hebben wij de nieuwste volta-potentiaal fase plaat (VPP) aangeschaft. De VPP induceert een $\pi/2$ faseverschuiving en verandert de CTF van een sinus-type naar een cosinus-type. We observeerden dat de DNA origami nanoplaat afgebeeld kan worden met een goed contrast in een enkele frame acquisitie door gebruik te maken van de VPP op een hoge versnel spanning (200 kV). In plaats van het gebruik van de VPP op een hoog kV, hebben we de origami samples ook geanalyseerd bij lage-kV (20 kV) waarden, gebruik makend van Cs+Cc gecorrigeerde microscopen (sub-Ångström lage voltage elektronen microscopie of SALVE) waarbij opnieuw een goed contrast waargenomen werd. De resultaten breiden het gebruik van aberratie-gecorrigeerde lage-voltage microscopie uit in de richting van de structurele biologie. De in-focus fase contrastmethoden besproken in dit hoofdstuk zijn veelbelovend om biomoleculen te bestuderen die niet zichtbaar zijn met conventionele, op defocus-gebaseerde TEM methodieken.

Het hoofddoel van **hoofdstuk 5** is om de structurele stabiliteit van DNA te onderzoeken binnen de natuurlijke vloeistofachtige omgeving. Een van de vragen was of het mogelijk is om een ongemarkeerd DNA molecuul in beeld te kunnen brengen in een vloeistofomgeving met elektronenmicroscopie, en wat de effecten zijn van de vloeistofcel (zoals SiN en grafeen vloeistof cellen). Tevens vragen we ons wat het effect is van

de verschillende beeldtechnieken (zoals STEM en TEM) op de structurele stabiliteit. We gebruiken een speciaal soort DNA nanostructuren voor dit doeleinde, namelijk DNA-Au nanoconjugaties. Deze conjugatiestructuren zijn hybride materialen die bestaan uit twee kleine nanodeeltjes (elk 5 nm in diameter in ons geval), die verbonden zijn via een dsDNA molecuul. Aangezien de Au deeltjes goede contrastmarkeerder zijn, zijn wij in staat gebleken om de geconjugeerde nanostructuren te volgen als functie van de tijd, en om de exacte locatie van het DNA tussen de deeltjes te bepalen om te zien of we een contrast kunnen observeren dat lijkt op het DNA. We vonden echter dat dit laatste niet mogelijk was, zelfs niet als we STEM gebruiken, wat een hogere signaal-ruis verhouding heeft dan TEM. Dit gold zelfs als het monster omsloten was in de erg dunne grafeen vloeistofcel. SiN vloeistofcellen boden niet de ideale condities voor in situ vloeistof studies op DNA in termen van resolutie en verhindering van schade door de elektronenstraal, terwijl de grafeen vloeistof cellen hier wel een voordeel boden.

Acknowledgements

I believe in the end the whole of life becomes an act of letting go.
But what always hurts the most, is not taking a moment to say goodbye.

Life of Pi

I paused for a moment and looked into the mirror before typing this section of my thesis. Five years have passed to take me into this moment; writing my last and certainly the most difficult lines. It has been such a roller coaster period. I have gone through a dramatic personal and professional revolution since I came to Delft from Erlangen, and the lessons learned here are ever-lasting and life-changing. The reflection in the mirror is not altered physically (delighted!) but he is not quite the same character as he used to be. I stepped into the PhD road so dismayed and innocent, and eventually made it to the end. But this journey would have not been possible without the support, care, advice, and company of countless amount of people, a handful of them deserve to be mentioned here.

Above all, my promotors **Cees** and **Henny** who helped me immensely in my professional PhD career. **Cees**, you are filled with curiosity and passion for understanding the physical world. Although it was not long after the start that we realized our scientific approach is totally different, I'm happy that we could get along quite well and realize the project towards the end. You will always have my utter respect and admiration. Hope you will finally convince everyone that science and religion do not contradict each other.

Henny, you have absolutely shattered my view about the mainstream academics. I have never seen a professor so eager to pursue his own research, walking into the lab in order to conduct the experiments, and encouraging students to ask the fundamental "why" question. I will never forget your hands-on trainings on sample preparations and the use of microscopes. On a different note, I enjoyed that you never weighed in on Cees's comments on my manuscripts, which would have otherwise ended up in a bloody tug of war. I wish you can continue developing awesome holders in your own garage until you are 80. Fingers crossed to your dream project of cooling holder with atomic resolution!

My partners in crime, **Sairam** and **Leonardo**. So much joy we had in and outside the lab. Our dirty minds extend well beyond imaginations, ensemble of all the evils in Iran, India, and Italy is just too much for one office. **Prof. Sairam**, I can easily blackmail you, your students are already asking me to reveal dirt on you. I look forward to the day that your son will finally come to me for some revelations. **Leonardo**, you surely realized your dream to cook a pizza at the smallest scale, I know that was your mere motivation to come to Holland and pursue a PhD. This makes you the most renowned Italian nanoscientist in my opinion. I am in big doubt about the exact chemistry of the gases you inserted into the Titan though.

Majid, a ruthless scientist, father, friend, and globe trotter. You do not belong to this broken academic system, change your career I insist. Let me know when you accept the fact that ASML is awesome, far beyond what your prejudice tells you. We make the smoothest man-made surface in the universe, isn't that mind-boggling for you? Let me thank you **Tata** and **Arsha**, to keep this man busy with what actually matters in life and preventing him to ruin his life in the dodgy microscope rooms. Special thank to you **Tata** for tolerating us when we talk about crappy scientific subjects.

I had the pleasure to supervise two extremely talented students during my PhD, **Shimroy** and **Cas**. **Shimmy Shimmy yay**, let me through back to those days in the lab, when you were bewildered how to run a gel, and I told you how to do it, though never done it myself either. You are a good example of tenacious goal-oriented person, who does not fear failures. I was enjoying to see you improving both scientifically and personally, you never seem to surrender. I hope my whip did not hurt your ego. And **Cas**, good job with all those fancy simulations man. Neither you nor me would have thought this BEP project to end up so cool. You remain always "Mooi" in my mind.

To all the great people I met at TU Delft, I appreciate that you were part of either my personal development or fun times. **Afshin** and **Hamid**, for the cheerful swimming and döner times we had together. I wish you all the success in your future career plans. The lab-mates at BN: all **Daniel** is love, I still don't buy your story **Michel** and you know which one I'm referring to, **Laura** you are too protective of your Colombian friends, thanks to **Stephanie**, **Jorine**, **Wayne**, **Daniel-V2 (Xin)**, and **Kuba** for sharing the pains of PhD, **Fabai** don't let the rumours confuse you, I believe you were the smartest PhD of our lab, and **Anthony** you are the most ignorant one, may the spirit of the supreme leader be with you, **Mahipal** you are too direct even for the Dutch, **Adi** don't walk around and shout "Allaho Akbar", that line is exclusively reserved for me to be used at my own discretion, **Jaco** I owe you big times most of my knowledge in molecular biology, very special thanks to you for the mixing and folding all those sneaky origami structures, I particularly enjoyed our open discussions about Dutch society and politics (minder, minder, ...), **Yaron** please don't play with fire and try to be a "normal" person, note that I have recently become very intolerant towards the vegans. I was delighted to share valuable times with other labs and departments at TU Delft: thanks to **Masha**, **Ahmed**, **Jouk**, **Ali**, **Frans**, and **Anil**, for sharing microscopes and cleanroom times. **Tatiana** I'm glad that you introduced me to your Russian friends, **Shiv** the world would have been a better place if everyone was chill like you. I adore my BN-mates, **Aleksandre**, **Eugene**, **Nils**, **Sonja**, **Je-Kyung**, **Jacob**, **Allard**, **Mehran**, **Alessio**, **Anna**, **Hirad**, **Federico**, **Reza**, **Thijs**, **Sam**, **Helena**, **Esengül**, **Sumit**, **Nicole**, **Rebecca**, **Viktorija**, **Benjamin**, **Mike**, **Sebastian**, **Misha**, **Theo**, and **Bojk** for making the BN an energetic department. Oh boy (**Bojk**), my dream is to be able to charm girls just like you.

Since moving to Eindhoven for work, I was surrounded by friendly people in Noord Brabant (I know it's hard for some Dutch people to consent). My dear friends at ASML, **Edgar** man we just forget to do more Squash, even my PhD finished before your Veranda, **Farnoosh** it's rare to have a cool Iranian officemate like you, **Paul** the camper idea was just the best ever, **Bas** tell her we all know why you started here one month after me, **Kees** your sole function is to remind me of my PhD supervisor, **Justyna** Polish lunch will resume in near future, **Maruschka** I envy your new kitchen, **Velislava** thanks for letting

a bunch of tech-talents ruin your house, **Saskia** please adopt dogs too, **Azin**, **Hamed**, **Yasaman**, **Amin**, and **Neda** Persian lunch with you makes me nostalgic, though we eat mostly Dutch food then. My warmest gratitude to my Bright managers, **Marcel**, **Leon**, and **Stijn**. Thanks for running this fabulous society and helping us flourish in high-tech industry.

Everyone agrees that I could not be standing here if it was not due to the divine devotion of my beloved parents. **Maman** and **Baba**, you are a vivid example that angels do walk on earth. Your pure love has filled my heart for eternity. Thanks for asking me what I eat for dinner every time we skype, in order to keep me healthy and agile. My lovely siblings, **Zahra** and **Yoosef**, when was the last time we travelled together? And my dear in-laws, **Mehrnoosh** and **Hamed**, don't listen to the stories you hear about me through my siblings.

Maaike, I don't know how to start and end when it comes to you, my heart would pound and my fingers tremble. Thanks for sowing the seed of love in my soul again, the one that has evolved so much in the past years, taking its toll along the way, but has remained truly genuine. For me, this thesis concludes with your name, but your thoughts will never end here.

Yoones (May 2019)

Curriculum Vitæ

YOONES KABIRI

29-10-1987	Born in Esfahan, Iran.

Education

2002–2006	High school diploma in mathematics and physics National organization for development of exceptional talents Esfahan, Iran
2006–2010	BSc. Materials Science and Engineering (cum laude) Isfahan university of technology, Iran Promotor: Prof. Ahmed Kermanpur
2011–2013	MSc. Advanced Materials and Processes (with distinction) University of Erlangen-Nuremberg, Germany Promotor: Prof. Erdmann Spiecker
2014–2018	PhD. Biophysics Delft university of technology, the Netherlands Promotors: Profs. Cees Dekker and Henny Zandbergen

Work Experience

2010–2011	Design Engineer at MAPNA, Iran
2012–2013	Development Engineer at DFG, Germany
2014–2018	Researcher at Kavli institute, The Netherlands
2018–present	Product performance and integration at ASML, The Netherlands

List of Publications

Related to this thesis:

1- **Yoones Kabiri**, Adithya N. Ananth, Jaco van der Torre, Allard Katan, Jin-Yong Hong, Sairam Malladi, Jing Kong, Henny Zandbergen, and Cees Dekker. Distortion of DNA Origami on Graphene Imaged with Advanced TEM Techniques, Small, 1700876, 2017

2- **Yoones Kabiri**, Alessandro Angelin, Ishtiaq Ahmed, Hatice Mutlu, Jens Bauer, Christof M. Niemeyer, Henny Zandbergen, Cees Dekker. Intercalating electron dyes for TEM visualization of DNA at the single-molecule level, ChemBioChem, 20 (2019)

3- **Yoones Kabiri**, Raimond B. G. Ravelli, Tibor Lehnert, Haoyuan Qi, Allard J. Katan, Natascha Roest, Ute Kaiser, Cees Dekker, Peter J. Peters, and Henny Zandbergen. Visualization of unstained DNA nanostructures with advanced in-focus phase contrast TEM techniques, Scientific Reports, 9 (2019)

4- **Yoones Kabiri**, Shimroy William, Cas de Mooij, Henny Zanbergen, Cees Dekker, Probing DNA nanostructures in graphene/SiN nanocapillaries with liquid-phase STEM, (under preparation)

Other publications:

5- **Yoones Kabiri**, Nadine Schrenker, Julian Müller, Mirza Mačković, Erdmann Spiecker, Direct observation of dislocation formation and plastic anisotropy in Nb2AlC MAX phase using in situ nanomechanics in transmission electron microscopy, Scripta Materialia, 137 (2017)

6- **Yoones Kabiri**, Ahmed Kermanpur, Ahmad Foroozmehr, Comparative study on microstructure and homogeneity of NiTi shape memory alloy produced by copper boat induction melting and conventional vacuum arc melting, Vacuum, 86 (2012)

7- Shibabrata Basak, Jacob Jansen, **Yoones Kabiri**, Henny Zandbergen, Towards optimization of experimental parameters for studying Li-O2 battery discharge products in TEM using in situ EELS, Ultramicroscopy, 188 (2018)

8- Mani Diba, Winston Camargo, Tatiana Zinkevich, Alina Grünewald, Rainer Detsch, **Yoones Kabiri**, Arno PM Kentgens, Aldo R Boccaccini, Jeroen JJP van den Beucken, Sander CG Leeuwenburgh, Hybrid particles derived from alendronate and bioactive glass for treatment of osteoporotic bone defects, Journal of Materials Chemistry B, 7 (2019)

9- Ahmad Foroozmehr, Ahmed Kermanpur, Fakhredin Ashrafizadeh, **Yoones Kabiri**, Investigating microstructural evolution during homogenization of the equiatomic NiTi shape memory alloy produced by vacuum arc remelting, Materials Science and Engineering A, 528 (2011)

10- Ahmad Foroozmehr, Ahmed Kermanpur, Fakhredin Ashrafizadeh, **Yoones Kabiri**, Effects of thermo-mechanical parameters on microstructure and mechanical properties of Ti–50 at.% Ni shape memory alloy produced by VAR method, Materials Science and Engineering A, 535 (2012)

11- Mohsen Mohammadi Zahrani, Mahmood Meratian, **Yoones Kabiri**, Innovative processing of lotus-type porous magnesium through thermal decomposition of wood, Materials Letters, 85 (2012)

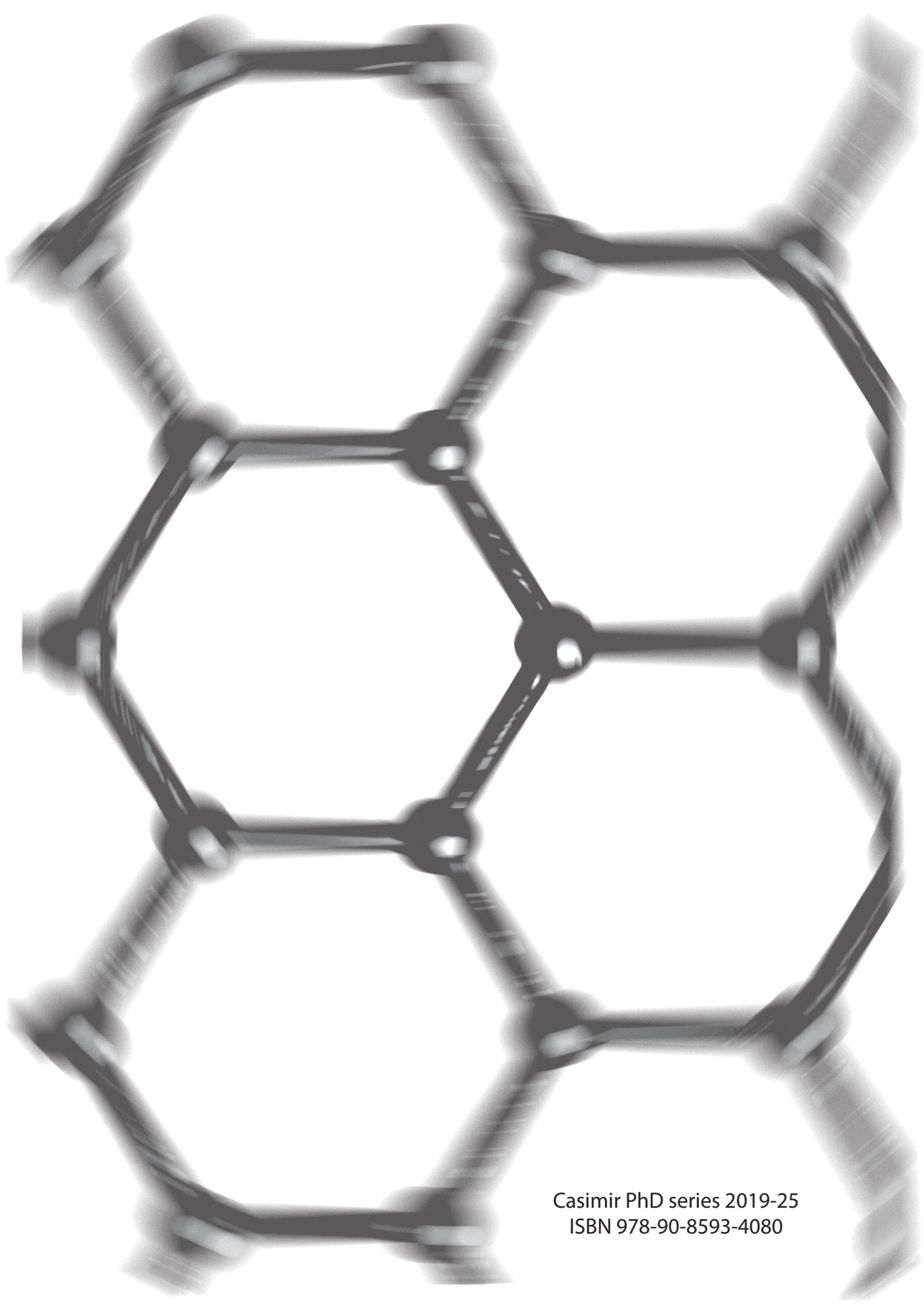

Casimir PhD series 2019-25
ISBN 978-90-8593-4080